

REPORT DOCUMENTATION PAGE

Form Approved
OMB No. 0704-0188

Public reporting burden for this collection of information is estimated to average 1 hour per response, including the time for reviewing instructions, searching existing data sources, gathering and maintaining the data needed, and completing and reviewing the collection of information. Send comments regarding this burden estimate or any other aspect of this collection of information, including suggestions for reducing this burden, to Washington Headquarters Services, Directorate for Information Operations and Reports, 1215 Jefferson Davis Highway, Suite 1204, Arlington, VA 22202-4302, and to the Office of Management and Budget, Paperwork Reduction Project (0704-0188), Washington, DC 20503.

1. AGENCY USE ONLY (Leave blank)

2. REPORT DATE

February 1994

3. REPORT TYPE AND DATES COVERED

4. TITLE AND SUBTITLE

Solution of the Average-Passage Equations for the Incompressible Flow Through Multiple-Blade-Row Turbomachinery

5. FUNDING NUMBERS

N00039-92-C-0100

6. AUTHOR(S)

J. J. Dreyer, W. C. Zierke

7. PERFORMING ORGANIZATION NAME(S) AND ADDRESS(ES)

Applied Research Laboratory
The Pennsylvania State University
P.O. Box 30
State College, PA 16804

8. PERFORMING ORGANIZATION REPORT NUMBER

TR-94-05

9. SPONSORING/MONITORING AGENCY NAME(S) AND ADDRESS(ES)

Advanced Research Projects Agency
3701 N. Fairfax Drive
Arlington, VA 22203-1717

10. SPONSORING/MONITORING AGENCY REPORT NUMBER

11. SUPPLEMENTARY NOTES

12a. DISTRIBUTION/AVAILABILITY STATEMENT

Unlimited

12b. DISTRIBUTION CODE

13. ABSTRACT (Maximum 200 words)

A system of equations governing the incompressible flow through a multiple-blade-row turbomachine is presented. These equations basically form the pseudo-compressible analog to the equations derived by Admaczyk [1984] for compressible, average-passage flow. The methodology behind the derivation is outlined, including a closure model for the time-averaged form of the equations. The equations are then preconditioned to facilitate numerical treatment. An explicit numerical procedure based on Runge-Kutta time stepping for cell-centered, hexahedral finite volumes is outlined for the approximate solution of the governing equations. Convergence acceleration techniques, boundary conditions, and closure issues are also addressed for the numerical scheme. Finally, results are presented for a simulation of the high Reynolds number flow through a two-blade-row, axial-flow pump. These comparisons suggest that the pseudo-compressible average-passage equations can make reasonable predictions of the highly three-dimensional flow within a multiple-blade-row turbomachine operating in an incompressible flow regime. However, especially in wake regions, it is clear that the behavior of the algebraic eddy viscosity model--at least with the present grid--requires improvement for the accurate prediction of the evolution of the downstream velocity field.

14. SUBJECT TERMS

Computational Fluid Dynamics, Turbomachinery, Axial Flow Pump, Incompressible Flow, Average-Passage Equations

15. NUMBER OF PAGES

123

16. PRICE CODE

17. SECURITY CLASSIFICATION OF REPORT

UNCLASSIFIED

18. SECURITY CLASSIFICATION OF THIS PAGE

UNCLASSIFIED

19. SECURITY CLASSIFICATION OF ABSTRACT

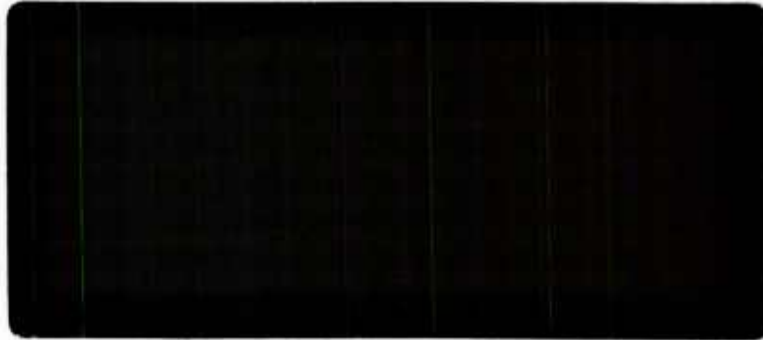
UNCLASSIFIED

20. LIMITATION OF ABSTRACT

UNLIMITED

Applied Research Laboratory

Technical Report



LIBRARY
RESEARCH REPORTS DIVISION
NAVAL POSTGRADUATE SCHOOL
MONTEREY, CA 93943-5002

PENNSTATE



~~The~~ Pennsylvania State University .
APPLIED RESEARCH LABORATORY
P.O. Box 30
State College, PA 16804

SOLUTION OF THE AVERAGE-PASSAGE
EQUATIONS FOR THE INCOMPRESSIBLE FLOW
THROUGH MULTIPLE-BLADE-ROW TURBOMACHINERY

by

J. J. Dreyer
W. C. Zierke

Technical Report No. TR 94-05
February 1994

Supported by:
Advanced Research Projects Agency

L.R. Hettche, Director
Applied Research Laboratory

Approved for public release; distribution unlimited

Abstract

A system of equations governing the incompressible flow through a multiple-blade-row turbomachine is presented. These equations basically form the pseudo-compressible analog to the equations derived by Adamczyk [1984] for compressible, average-passage flow. The methodology behind the derivation is outlined, including a closure model for the time-averaged form of the equations. The equations are then preconditioned to facilitate numerical treatment. An explicit numerical procedure based on Runge-Kutta time stepping for cell-centered, hexahedral finite volumes is outlined for the approximate solution of the governing equations. Convergence acceleration techniques, boundary conditions, and closure issues are also addressed for the numerical scheme. Finally, results are presented for a simulation of the high Reynolds number flow through a two-blade-row, axial-flow pump. These comparisons suggest that the pseudo-compressible average-passage equations can make reasonable predictions of the highly three-dimensional flow within a multiple-blade-row turbomachine operating in an incompressible flow regime. However, especially in wake regions, it is clear that the behavior of the algebraic eddy viscosity model—at least with the present grid—requires improvement for the accurate prediction of the evolution of the downstream velocity field.

Acknowledgements

We would like to extend our appreciation to the Advanced Research Projects Agency (ARPA) and Mr. Gary W. Jones for supporting this research under the Submarine Technology Program. As the head of the Applied Science Division when this program began, Dr. Robert E. Henderson was instrumental in initiating this effort. Also, as head of the Fluid Dynamics Department, Dr. Michael L. Billet gave valuable support throughout the program.

As the developer of the average-passage equations and the original compressible flow code, Dr. John J. Adamczyk at the NASA Lewis Research Center was a principal contributor to the completion of this project. Also, John's team of engineers at Sverdrup Technologies--especially Mr. Tim A. Beach, Mr. Mark L. Celestina, and Dr. Kevin R. Kirtley--gave valuable recommendations throughout the project. Dr. Eli Turkel of Tel-Aviv University provided insight into preconditioning. At ARL Penn State, Dr. Gilbert H. Hoffman provided consultation on grid generation and, later in the project, Dr. Henry McDonald and Dr. Charles J. Knight gave some valuable advise. Finally, Mr. William A. Straka and Mr. P. David Taylor helped to provide many of the figures comparing numerical predictions with experimental data.

Table of Contents

	<u>Page</u>
Abstract	ii
Acknowledgment	iii
List of Figures	v
Nomenclature	ix
1. Introduction	1
2. Governing Equations	2
2.1 Navier-Stokes Equations	4
2.2 Average-Passage Equations	5
2.2.1 Ensemble Averaging	6
2.2.2 Time Averaging	8
2.2.3 Passage-to-Passage Averaging	10
2.2.4 Modifications to the Navier-Stokes Equations	12
2.3 Closure Modelling for the Time-Averaged Equations	14
2.4 Pseudo-Compressibility and Preconditioning	
3. Numerical Discretization	16
3.1 Cell-Centered Finite-Volume Discretization in Space	16
3.2 Artificial Dissipation	17
3.3 Time Integration	21
3.4 Convergence Acceleration	22
3.4.1 Local Time Stepping	23
3.4.2 Implicit Residual Averaging	24
3.4.3 Multigrid	25
3.5 Boundary Conditions	27
3.6 Closure Modelling	28
3.6.1 Reynolds Stress Closure	28
3.6.2 Average-Passage Closure	28
4. Comparison of Numerical and Experiment Results	30
4.1 High Reynolds Number Pump Experiment	30
4.2 Grid Generation	31
4.3 Solution Procedure	32
4.4 Comparisons	32
4.4.1 Inlet Guide Vanes	33
4.4.2 Rotor Blades	35
5. Summary and Conclusions	40
Bibliography	42

List of Figures

<u>Figure</u>	<u>Page</u>
3.1 Generic Flow Domain with the Relevant Coordinate System	44
3.2 Generic Finite-Volume Cell	45
3.3 Directed Areas from a Generic Finite-Volume Cell	46
3.4 Neutral Stability Boundaries	47
3.5 Types and Locations of Boundary Conditions for a Typical Blade Passage	48
4.1 Isometric View of the HIREP Blades with the Cylindrical Coordinate System	49
4.2 Slices of the IGV Three-Dimensional, Computational Grids	50
4.3 Slices of the Rotor Blade Three-Dimensional, Computational Grid . .	51
4.4 Two-Dimensional Computational Grid Defining the Meridional Domain of HIREP	52
4.5 IGV Static-Pressure Distribution	53
4.6 IGV Suction Surface Static-Pressure Contours	54
4.7 IGV Pressure Surface Static-Pressure Contours	55
4.8 Circumferential Variation of Velocity Components 49.7% Chord Axially Downstream of the IGV Trailing Edge--Five-Hole Probe Measurements and ISTAGE Predictions:	
(a) 4.8% Span	56
(b) 9.5% Span	57
(c) 19.0% Span	58
(d) 38.1% Span	59
(e) 52.4% Span	60
(f) 61.9% Span	61
(g) 71.4% Span	62
(h) 76.2% Span	63
(i) 81.0% Span	64
(j) 85.7% Span	65
(k) 90.5% Span	66
(l) 95.2% Span	67

List of Figures (Cont.)

<u>Figure</u>	<u>Page</u>
4.9 Secondary Velocity Vectors 49.7% Chord Axially Downstream of the IGV Trailing Edge:	
(a) ISTAGE Predictions	68
(b) Five-Hole Probe Rake Surveys	69
4.10 Total-Pressure Coefficient Contours 49.7% Chord Axially Downstream of the IGV Trailing Edge:	
(a) ISTAGE Predictions	70
(b) Five-Hole Probe Rake Surveys	71
4.11 Circumferentially-Averaged Pressure Coefficients 49.7% Chord Axially Downstream of the IGV Trailing Edge	72
4.12 Circumferentially-Averaged Velocities 49.7% Chord Axially Downstream of the IGV Trailing Edge	73
4.13 Rotor Blade Static-Pressure Distribution	74
4.14 Rotor Blade Suction Surface Static-Pressure Contours	75
4.15 Rotor Blade Pressure Surface Static-Pressure Contours	76
4.16 Variation of Rotor Shaft Thrust and Torque with Volumetric Flow Coefficient	77
4.17 Predicted Particle Paths, One Grid Point from the Rotor Blade Hub	78
4.18 Schematic of Surface Flow Visualization on the Rotor Blade Hub Surface	79
4.19 Predicted Particle Paths, One Grid Point from the Rotor Blade Suction Surface	80
4.20 Schematic of Surface Flow Visualization on the Rotor Blade Suction Surface	81
4.21 Axial Velocity Contours 32.2% Chord Axially Downstream of the Rotor Tip Trailing Edge:	
(a) ISTAGE Predictions	82
(b) LDV Measurements	83

List of Figures (Cont.)

<u>Figure</u>	<u>Page</u>
4.22 Tangential Velocity Contours 32.2% Chord Axially Downstream of the Rotor Tip Trailing Edge:	
(a) ISTAGE Predictions	84
(b) LDV Measurements	85
4.23 Predicted Secondary Velocity Vectors 32.2% Chord Axially Downstream of the Rotor Tip Trailing Edge	86
4.24 Spanwise Position of the Core of the Rotor Tip Leakage Vortex	87
4.25 Blade-to-Blade Position of the Core of the Rotor Tip Leakage Vortex	88
4.26 Prediction Particle Paths of the Rotor Tip Leakage Vortex and the Trailing Edge Separation Vortex	89
4.27 Photograph of a Cavitating Rotor Tip Leakage Vortex and a Cavitating Trailing Edge Separation Vortex (Farrell [1989])	90
4.28 Circumferential Variation of Velocity Components 32.2% Chord Axially Downstream of the Rotor Tip Trailing Edge--LDV Measurements and ISTAGE Predictions:	
(a) 2.9% Span	91
(b) 8.6% Span	92
(c) 10.5% Span	93
(d) 19.9% Span	94
(e) 29.4% Span	95
(f) 38.8% Span	96
(g) 48.2% Span	97
(h) 57.7% Span	98
(i) 67.1% Span	99
(j) 81.3% Span	100
(k) 86.0% Span	101
(l) 90.7% Span	102
(m) 94.5% Span	103
(n) 98.3% Span	104
(o) 99.2% Span	105

List of Figures (Cont.)

<u>Figure</u>	<u>Page</u>
4.29 Passage-Averaged Rotor Blade Wakes at 76.2% Span: (a) 2.5%, 4.8%, 7.2%, and 11.8% Chord Axially Downstream of the Rotor Blade Trailing Edge	106
(b) 16.5%, 21.1%, and 24.6% Chord Axially Downstream of the Rotor Blade Trailing Edge	107
4.30 Circumferentially-Averaged Velocities 32.2% Chord Axially Downstream of the Rotor Tip Trailing Edge	108
4.31 Circumferentially-Averaged Pressure Coefficients 32.2% Chord Axially Downstream of the Rotor Tip Trailing Edge	109
4.32 Predicted Contours of Total-Pressure Coefficient 32.2% Chord Axially Downstream of the Rotor Tip Trailing Edge	110

Nomenclature

A	outward directed area of a cell face; circumferential averaging operator
C_p	pressure coefficient = $\frac{P - P_{\text{ref}}}{\frac{1}{2}\rho V_{\text{ref}}^2}$
CFL	Courant-Friedrichs-Lewy number (or Courant number)
d	artificial dissipation flux
D	length
D	artificial dissipation operator
E	vector of discrete spatial terms
f	arbitrary function; generic force
F	flux vector in the axial direction
G	gate function for space averaging
G	flux vector in the radial direction
$h, 2h, 4h$	fine, coarsened, and doubly-coarsened grids, respectively
H	gate function for time averaging
H	flux vector in the tangential direction
HIREP	high Reynolds number pump
i, j, k	indices
IGV	inlet guide vane
ISTAGE	computer code developed to solve the incompressible, average-passage equations

Nomenclature (Cont.)

K	source term from cylindrical coordinates
K_p	pressure coefficient = $\frac{p - p_{ref}}{\frac{1}{2}\rho U_{tip}^2}$
L	three-dimensional flux operator
LDV	laser Doppler velocimeter
m	number of blades in the referenced blade row
N	number of ensembles
p	static pressure
P	preconditioning matrix
q	portion of the eigenvalues
Q	vector of dependent variables
r	radial independent variable
R	residual
R^*	implicitly-averaged residual
R_{ij}	stress tensor
RANS	Reynolds-averaged Navier-Stokes
Re	Reynolds number
S	source term from average passage
t	time
t_1	pseudo-time

Nomenclature (Cont.)

u, U	absolute velocity
U_{tip}	rotor blade tip speed
U	vector of dependent variables for pseudo-compressibility
V_{ref}	inlet reference axial velocity
Vol	cell volume
VON	von Neumann number
w	relative velocity
z	axial independent variable
α	preconditioning parameter; Runge-Kutta factor
β	pseudo-compressibility parameter
γ	preconditioning parameter (always -1)
Γ	term in the viscous time step limit
δ	aspect-ratio scale factor for artificial dissipation
Δ	discrete undivided difference operator
ϵ	residual smoothing factor
$\epsilon^{(2)}, \epsilon^{(4)}$	second- and fourth-difference artificial dissipation
ζ	computational coordinate (radial direction)
η	computational coordinate (axial direction)
θ	tangential (or azimuthal) independent variable

Nomenclature (Cont.)

$\kappa^{(2)}, \kappa^{(4)}$	second- and fourth-difference artificial viscosity factor
λ	geometric blockage
ν	kinematic viscosity; pressure gradient switch
ν_e	eddy viscosity
ν_T	total viscosity (kinematic and eddy)
ξ	computational coordinate (tangential or azimuthal direction)
ρ	fluid density (constant)
τ_{ij}	shear stress
ϕ	artificial viscosity blending factor
ψ	wave speed
Ψ	product of the wave speed and the geometric blockage factor
Ω	shaft speed

Subscripts

1,2,3,4	stages of the Runge-Kutta-like scheme
$h, 2h, 4h$	fine, coarsened, and doubly-coarsened grids, respectively
i, j, k	indices
i, I	inviscid
ijk	$(i, j, k)^{th}$ control volume or cell
m	number of blades in the referenced blade row

Nomenclature (Cont.)

r	radial direction
ref	reference quantity
R	rotor blade row
S	stator blade row
v, V	viscous
z	axial direction
ζ	computational radial direction
η	computational axial direction
θ	tangential or azimuthal direction
ξ	computational tangential or azimuthal direction

Superscripts

AX	axisymmetric
(i)	blade row index
$(1), (2)$	blade row number
\sim	dimensional quantity
$-$	ensemble average
$=$	time average
\equiv	passage-to-passage average
\wedge	nondeterministically or randomly unsteady
$\hat{_}$	deterministically unsteady
$/$	unsteady with respect to both blade rows

1. Introduction

In recent years, the design and analysis of turbomachinery has increasingly turned to numerical computations in order to improve estimates of this complex flow field. The improved estimates of this three-dimensional, viscous (turbulent) flow becomes even more important when dealing with turbomachines with a multiple number of blade rows. Most of the recent advances in this area have dealt with compressible flow. This report summarizes work to extend numerical computations of multiple-blade-row turbomachines to incompressible flow.

First, this report outlines the mathematical basis of the average-passage representation of a multiple-blade-row turbomachine. Specifically, starting with the Navier-Stokes equations, Chapter 2 describes the basic methodology that leads to the incompressible average-passage equations. Then, the closure problem associated with this representation is discussed, followed by a description of a closure model appropriate for a single-stage (two-blade-row) turbomachine operating incompressibly. Finally, the governing equations are cast in a preconditioned, pseudo-compressible form that is more appropriate for numerical approximation.

After establishing the mathematical model, we describe the numerical technique used to approximate a steady-state solution to the system of equations presented in Chapter 2. Specifically, Chapter 3 describes the spatial and temporal discretizations of the governing equations, along with the acceleration techniques used to expedite the achievement of a steady-state solution to the discrete equations. Then, we give a brief description of the boundary conditions appropriate for a pseudo-unsteady, average-passage representation of a blade row. Finally, Chapter 3 addresses the numerics of the closure model proposed in Chapter 2 for a single-stage machine.

With the development of a computer code called IStage that numerically solves the average-passage equations for an incompressible flow, we computed an experimentally-measured flow field as a first step towards code validation. Zierke, Straka, and Taylor [1993] acquired measurements in the high Reynolds number pump (HIREP) facility, during an experimental program that was performed in parallel with the numerical program described herein. The numerical computations of this incompressible flow of water through a two-blade-row pump were performed as a prediction, using a uniform inflow rather than the experimentally measured inflow. Chapter 4 shows a large number of comparisons between the numerical predictions and the experimental data, resulting in a good measure of the current status of our numerical model.

2. Governing Equations

In this chapter, the derivation of the average-passage equation system is briefly described. In his original derivation, Adamczyk [1984] outlined a more rigorous treatment for compressible flow. Beginning with the Navier-Stokes equations, we describe the general form of the average-passage equations for incompressible flow, including the averaging operators that are used in their derivation. This is followed by a description of a simple closure model to estimate the resulting body forces and correlation terms. Finally, the equations are cast in a preconditioned pseudo-compressible form better suited for numerical treatment.

2.1 Navier-Stokes Equations

The starting point for the derivation of the average-passage equations is the incompressible Navier-Stokes equations in cylindrical coordinates. They are given as follows:

$$\frac{\partial u_z}{\partial z} + \frac{1}{r} \frac{\partial}{\partial r} (ru_r) + \frac{1}{r} \frac{\partial u_\theta}{\partial \theta} = 0, \quad (2.1)$$

$$\frac{\partial u_z}{\partial t} + \frac{\partial}{\partial z} (u_z^2 + p) + \frac{1}{r} \frac{\partial}{\partial r} (ru_r u_z) + \frac{1}{r} \frac{\partial}{\partial \theta} (u_z u_\theta) =$$

(2.2)

$$\frac{\partial}{\partial z} (\tau_{zz}) + \frac{1}{r} \frac{\partial}{\partial r} (r\tau_{rz}) + \frac{1}{r} \frac{\partial}{\partial \theta} (\tau_{z\theta}),$$

$$\frac{\partial u_r}{\partial t} + \frac{\partial}{\partial z} (u_z u_r) + \frac{1}{r} \frac{\partial}{\partial r} [r(u_r^2 + p)] + \frac{1}{r} \frac{\partial}{\partial \theta} (ru_r u_\theta) =$$

(2.3)

$$\frac{1}{r} (u_\theta^2 + p - \tau_{\theta\theta}) + \frac{\partial}{\partial z} (\tau_{rz}) + \frac{1}{r} \frac{\partial}{\partial r} (r\tau_{rr}) + \frac{1}{r} \frac{\partial}{\partial \theta} (\tau_{r\theta}),$$

and

$$\frac{\partial}{\partial t} (ru_\theta) + \frac{\partial}{\partial z} (ru_z u_\theta) + \frac{1}{r} \frac{\partial}{\partial r} (r^2 u_r u_\theta) + \frac{1}{r} \frac{\partial}{\partial \theta} [r(u_\theta^2 + p)] =$$

(2.4)

$$\frac{\partial}{\partial z} (r\tau_{\theta z}) + \frac{1}{r} \frac{\partial}{\partial r} (r^2 \tau_{\theta r}) + \frac{1}{r} \frac{\partial}{\partial \theta} (r\tau_{\theta\theta}).$$

Respectively, these equations represent the conservation of mass, axial momentum, radial momentum, and angular momentum. The thermal energy equation is not included because it is decoupled from the above equations if the kinematic viscosity is assumed to be constant. Equations 2.1 through 2.4 are written in terms of nondimensionalized dependent and independent

variables as discussed later. The shear stress terms in the Navier-Stokes equations are given by the following:

$$\tau_{zz} = \frac{2}{Re} \frac{\partial u_z}{\partial z} ,$$

$$\tau_{rr} = \frac{2}{Re} \frac{\partial u_r}{\partial r} ,$$

$$\tau_{\theta\theta} = \frac{2}{Re} \left[\frac{1}{r} \frac{\partial u_\theta}{\partial \theta} + \frac{u_r}{r} \right] ,$$

$$\tau_{rz} = \tau_{zr} = \frac{1}{Re} \left[\frac{\partial u_r}{\partial z} + \frac{\partial u_z}{\partial r} \right] ,$$

$$\tau_{r\theta} = \tau_{\theta r} = \frac{1}{Re} \left[\frac{1}{r} \frac{\partial u_z}{\partial \theta} + \frac{\partial u_\theta}{\partial z} \right] ,$$

and

$$\tau_{r\theta} = \tau_{\theta r} = \frac{1}{Re} \left[\frac{1}{r} \frac{\partial u_r}{\partial \theta} + \frac{\partial u_\theta}{\partial r} - \frac{u_\theta}{r} \right] ,$$

where the reference Reynolds number is defined as

$$Re = \frac{U_{ref} D_{ref}}{\nu_{ref}} .$$

For the above equations, the following nondimensionalizations apply:

$$z = \frac{\tilde{z}}{D_{ref}} , \quad r = \frac{\tilde{r}}{D_{ref}} , \quad t = \frac{\tilde{t} U_{ref}}{D_{ref}} ,$$

and

$$u_z = \frac{\tilde{u}_z}{U_{ref}} , \quad u_r = \frac{\tilde{u}_r}{U_{ref}} , \quad u_\theta = \frac{\tilde{u}_\theta}{U_{ref}} , \quad p = \frac{\tilde{p}}{\rho_{ref} U_{ref}^2} ,$$

with the assumption of incompressibility giving

$$\rho = \frac{\tilde{\rho}}{\rho_{ref}} \equiv 1.0$$

and

$$\nu = \frac{\tilde{\nu}}{\nu_{ref}} \equiv 1.0 .$$

For completeness, the shaft rotation rate is nondimensionalized as

$$\Omega = \frac{\tilde{\Omega} D_{ref}}{U_{ref}} .$$

In the above, a tilde (\sim) denotes a dimensional quantity and the subscript "ref" denotes a reference quantity. In this work, the equations are applied to the flow through a turbomachine. The reference length is taken to be the machine diameter and the reference velocity is taken to be the average velocity through the inlet of the machine (that is, the mass flow divided by the inlet area). The reference density and viscosity are taken from the properties of the working fluid.

Equations 2.1 through 2.4 represent the starting point for all of the analysis that follows in the remainder of this report. Note that in their present form, these equations are exact--they are the equations governing the unsteady motion of an incompressible fluid. However, because of the lack of a time derivative in Equation 2.1, the equations cannot be written as a complete system of time evolution equations (unlike the equations governing compressible flow). Ultimately, this difficulty will be rectified by restricting the interest to steady-state solutions, permitting the familiar pseudo-compressibility assumption. However, this is done only after the derivation of the average-passage equations of motion.

2.2 Average-Passage Equations

The average-passage equations govern the "average" flow within a blade passage embedded in a multiple-blade-row turbomachine. Deriving equations that govern an averaged flow field is a familiar exercise. Ensemble (or Reynolds) averaging the Navier-Stokes equations to yield the so-called Reynolds-averaged Navier-Stokes (RANS) equations is a well known procedure used to formulate equations describing turbulent (nondeterministically unsteady) flows in some "average" sense. In that case, the term "average" means steady or, at most, deterministically unsteady. For the average-passage equations, the term "average" is understood to be flow that is steady and spatially periodic over the pitch of the blade row of interest. Clearly, if a turbomachine has M blade rows, there are, in general, M associated average-passage flow fields; that is, each blade row has a representative or average passage.

Adamczyk [1984] developed the average-passage equations by the sequential application of three distinct averaging operators to the Navier-Stokes equations within a multiple-blade-row

environment. The resulting equations thus describe the flow through a referenced blade row embedded in a multiple-blade-row turbomachine in a steady, spatially periodic sense that is unique to the referenced blade row. A difficulty associated with this averaged system of equations, however, is the necessity to provide body forces and temporal and spatial correlations to properly account for the effects of neighboring rotating and stationary blade rows on the referenced blade row. Analogous to Reynolds averaging, the correlations are a direct result of the nonlinear convection terms in the governing equations and must be modelled by additional equations or empirically-based approximations. These operators are briefly described in this section.

2.2.1 Ensemble Averaging

The first operator applied to the governing equations (2.1 through 2.4) is the familiar ensemble (or Reynolds) averaging operator. For an arbitrary function, f , this averaging operation is defined as

$$\bar{f} = \lim_{N \rightarrow \infty} \frac{1}{N} \sum_{i=1}^N f_i \quad (2.5)$$

where f_i is the i^{th} realization of f . The function can then be decomposed into an ensemble-averaged component plus a random component, that is

$$f = \bar{f} + \hat{f} \quad (2.6)$$

where, by construction,

$$\overline{\hat{f}} \equiv 0 .$$

It is important to note that the ensemble averaging operator commutes with both temporal and spatial differentiation.

The procedure for ensemble averaging the governing equations begins with decomposing the velocities and pressure in Equations 2.1 through 2.4 according to Equation 2.6. The equation is then operated on by Equation 2.5, taking advantage of its commutative properties with differentiation. The result is the familiar Reynolds-averaged Navier-Stokes equations. The RANS equations are merely the Navier-Stokes equations with the dependent variables replaced by their ensemble-averaged counterparts and with the inclusion of some additional stress-like terms. These apparent or "Reynolds" stresses are a direct result of the nonlinear convection terms and involve correlations of the randomly fluctuating components of velocity. To solve the RANS equations requires some approximation or modelling of these terms. This is the familiar closure problem of

turbulent flow prediction. There are in existence a myriad of models available for Reynolds stress closure. A fairly standard model is utilized in this work and is described in the next chapter.

In essence, by solving the RANS equations (after providing some appropriate model for the Reynolds stresses), a deterministic flow field is sought with the effects of the random fluctuations in the variables accounted for in some average sense. Conceptually, this is what is intended for two additional averaging operations: time averaging and passage-to-passage averaging.

2.2.2 Time Averaging

The second step in the derivation of the average-passage equations is the application of a time-averaging operator to the ensemble-averaged governing equations. The operator is designed so that it may be applied everywhere in the flow domain including the regions within rotating blade rows. Basically, this operator averages its operand over a period equal to one shaft rotation. The

form of this operator acting on an ensemble-averaged function, \bar{f} , is given by

$$\bar{\bar{f}} = \frac{\Omega}{2\pi} \frac{1}{\lambda_R} \int_{t_1}^{t_1 + 2\pi/\Omega} H(t) \bar{f}(t) dt, \quad (2.7)$$

where

Ω = shaft speed

λ_R = geometric blockage of the neighboring rotating blade row(s)

$H(t)$ = "gate" function.

The purpose of the gate function is to permit the application of the operator everywhere in the flow domain. By definition, H is equal to one everywhere outside of a neighboring rotor blade row; at a point within a neighboring rotor blade row, H is equal to one for all times that the point is immersed in fluid and equal to zero whenever the point lies within a passing blade. The ratio of time for which the gate function equals one to the time for which it equals zero is a measure of the geometric blockage, λ_R , of the neighboring rotor blade row.

The ensemble-averaged function, \bar{f} , can now be decomposed into two components such that

$$\bar{f} = \bar{\bar{f}} + \hat{\bar{f}}. \quad (2.8)$$

where

\bar{f} = time-averaged component,

\hat{f} = deterministic unsteady component,

and, by construction,

$$\overline{\hat{f}} \equiv 0 .$$

Unlike the ensemble averaging operator, time averaging does not, in general, commute with differentiation. Due to the presence of the gate function, there arise additional terms in the interchange of averaging and differentiation. The consequences of this are discussed subsequently.

Time averaging the ensemble-averaged Navier-Stokes equation proceeds by decomposing the dependent variable in the RANS equations according to Equation 2.8 and operating on the resulting equations using Equation 2.7. In a manner completely analogous to ensemble averaging, the time averaging procedure gives rise to terms akin to Reynolds stresses. These apparent or "mixing" stresses are a direct result of the deterministic unsteadiness (that is, unsteadiness that correlates with shaft speed) within the flow field due to the presence of both rotating and stationary blade rows. Additionally, however, the interchange of time averaging and differentiation gives rise to forcing terms proportional to the average pressure loading and shear stress on the surfaces of the rotating blades. Time averaging thus gives rise to a set of body forces as well as an additional set of mixing stresses (or temporal correlations) that must be modelled along with the Reynolds stresses.

It is important to recall the working definition of the average-passage flow field for a given blade row embedded in a multiple-blade-row environment. The average-passage flow field for a given blade row is constructed to be steady and spatially periodic over the pitch of the blade row. For a single-stage machine (or a multi-stage machine whose respective stator and rotor blade rows all have integral-multiple blade counts), subject to an axisymmetric inflow and outflow, the time-averaged flow field is the average-passage flow field. That is, ensemble and time averaging are sufficient to render the flow field steady and spatially periodic over the pitch of each of the blade rows. Thus, to calculate the average-passage flow for a case such as this requires only the modelling of the time-averaged Reynolds stresses (from ensemble averaging) and body forces and temporal correlations (from time averaging).

2.2.3 Passage-to-Passage Averaging

In more general multiple-blade-row configurations, the number of blades in a given blade row is typically chosen such that it is not an integral multiple of the number of blades in any other blade row. As such, in general, the time-average flow relative to some blade row will not be spatially periodic over the pitch of that blade row. To force this spatially aperiodic flow field to be periodic requires the application of a third averaging operator. This is the so-called passage-to-passage averaging operator. Using the methods of Fourier analysis, this operator averages out the passage-to-passage variations of the time-averaged flow field for a given blade row while accounting for the global effect of these variations through an additional set of body forces and momentum mixing correlations. The form of this operator acting on the time-averaged variable,

\bar{f} , is given by

$$\bar{\bar{f}} = \frac{1}{\lambda_s} \sum_{k=-\infty}^{\infty} \int_0^{2\pi} A_{km} e^{ikm\theta} d\theta, \quad (2.9)$$

where

$$A_{km} = \frac{1}{2\pi} \int_0^{2\pi} G(\theta) \bar{f}(\theta) e^{ikm\theta} d\theta$$

and

m = number of blades in the referenced blade row

λ_s = geometric blockage of the neighboring stationary blade row

$G(\theta)$ = "gate" function.

Once again, the purpose of the gate function is to permit the application of the operator everywhere in the flow field. Analogous to the definition of the gate function, H , for the time averaging operator, G is equal to one everywhere outside of neighboring stator blade rows; within neighboring stator blade rows, G is equal to one outside of the blades and equal to zero within the blades. The ratio of the angular position for which this gate function equals one to the angular position for which it equals zero is a measure of the geometric blockage, λ_s , of the neighboring

stator blade row. The time-averaged function, \bar{f} , can now be decomposed into two components

such that

$$\overline{f} = \overline{\overline{f}} + \overline{\hat{f}}, \quad (2.10)$$

where

$\overline{\overline{f}}$ = passage-to-passage-averaged component

$\overline{\hat{f}}$ = spatially aperiodic component.

By construction, the passage-to-passage-averaged component, $\overline{\overline{f}}$, is spatially periodic over

the pitch of the referenced blade row. Once again, unlike the ensemble averaging operator, the passage-to-passage averaging operator does not, in general, commute with differentiation. As with the time averaging operator, the presence of the gate function, G , in the passage-to-passage operator gives rise to additional terms from the interchange of averaging and differentiation. Note also that because the passage-to-passage averaging operator is constructed with its periodicity equal to that of a referenced blade row, there will be a unique average-passage flow field for each blade row in a multiple-blade-row turbomachine.

Finally, to reduce the average-passage equations from the time-averaged equations of motion requires the application of the decomposition, Equation 2.10, and the passage-to-passage averaging operator, Equation 2.9, to the time-averaged equations. As with time averaging, this procedure yields an additional set of Reynolds stress-like terms. These terms represent mixing correlations arising from passage-to-passage flow variations in the time-averaged flow field. Additionally, the interchange of passage-to-passage averaging and differentiation gives rise to additional forcing terms related to the time-averaged pressure and shear stress loadings on the blade surfaces of neighboring stator blade rows. In short, passage-to-passage averaging yields yet another set of body forces and mixing stresses (spatial correlations) to be modelled in addition to those resulting from ensemble and time averaging.

2.2.4 Modifications to the Navier-Stokes Equations

The average-passage equations are essentially the Navier-Stokes equations with some additional terms and with the dependent variables understood to be ensemble, time, and passage-to-passage averaged. There are additional mixing stress terms that are due to nonlinear interactions of turbulent fluctuations, deterministic time-dependent fluctuations, and fluctuations due to spatial aperiodicities. In essence, the shear stress terms in Equations 2.2 through 2.4 can be thought of as being augmented in the following way:

$$\tau_{ij} \Rightarrow \tau_{ij} - R_{ij} ,$$

where i and j take on all combinations of z , r , and θ , and

$$R_{ij} = \overline{\hat{u}_i \hat{u}_j} + \overline{\hat{u}_i} \overline{\hat{u}_j} + \overline{\hat{u}_i} \overline{\hat{u}_j} \quad (2.11)$$

The first term in Equation 2.11 represents the passage-to-passage, time-averaged Reynolds stress; the second term represents the passage-to-passage-averaged mixing stress due to deterministic unsteadiness; and the last term represents a mixing stress due to the steady aperiodic velocity field. There are also forcing functions that account for the average effects of pressure and shear stress loadings from neighboring rotating and stationary blade rows. For the sake of brevity, the full equations are not listed here (see Adamczyk [1984]). The modelling of the tensor (2.11) as well as the body force terms from time and passage-to-passage averaging constitutes the closure problem for the average-passage system of equations.

In this work, only the closure problem associated with the ensemble and time averaging is addressed. As such, it is more convenient to handle only the Reynolds stresses as additional, apparent stresses and to "lump" together all of the mixing stresses and body forces from time averaging into a single source term. A model for computing this source is presented in Section 2.3. With this in mind, the vector form of the average-passage equations for a given blade row rotating at a shaft speed, Ω , can be written as

$$\frac{\partial}{\partial t_1}(\lambda Q) + \frac{\partial}{\partial z}(\lambda F) + \frac{1}{r} \frac{\partial}{\partial r}(\lambda r G) + \frac{1}{r} \frac{\partial}{\partial \theta}(\lambda H) = \lambda K - \lambda S , \quad (2.12)$$

where

$$F = F_i - F_v , \quad G = G_i - G_v , \quad H = H_i - H_v , \quad K = K_i - K_v ,$$

and the subscripts "i" and "v" denote the inviscid and viscous portions of the flux vectors.

Equation 2.12 includes the following vector definitions:

$$\begin{aligned}
 Q &= \begin{bmatrix} 0 \\ u_z \\ u_r \\ ru_\theta \end{bmatrix}, & F_i &= \begin{bmatrix} u_z \\ u_z^2 + p \\ u_z u_r \\ ru_z u_\theta \end{bmatrix}, & G_i &= \begin{bmatrix} u_r \\ u_r u_z \\ u_r^2 + p \\ ru_r u_\theta \end{bmatrix}, \\
 H_i &= \begin{bmatrix} u_\theta \\ w_\theta u_z \\ w_\theta u_r \\ r(u_\theta w_\theta + p) \end{bmatrix}, & K_i &= \begin{bmatrix} 0 \\ 0 \\ \frac{1}{r}(u_\theta^2 + p) \\ 0 \end{bmatrix}, & F_v &= \begin{bmatrix} 0 \\ \tau_{zz} \\ \tau_{zr} \\ r\tau_{z\theta} \end{bmatrix}, \\
 G_v &= \begin{bmatrix} 0 \\ \tau_{rz} \\ \tau_{rr} \\ r\tau_{r\theta} \end{bmatrix}, & H_v &= \begin{bmatrix} 0 \\ \tau_{\theta z} \\ \tau_{\theta r} \\ r\tau_{\theta\theta} \end{bmatrix}, & K_v &= \begin{bmatrix} 0 \\ 0 \\ \frac{1}{r}\tau_{\theta\theta} \\ 0 \end{bmatrix},
 \end{aligned}$$

where

$$w_\theta = u_\theta - r\Omega$$

λ = geometric blockage of neighboring blade rows

S = source term containing the body forces and correlations unique to the average passage system of equations.

Several things need to be clarified about the above equations. First, note that in each term of Equation 2.12, there appears a scale factor multiplying the dependent variables. This blockage factor is a purely geometrically-derived scalar. Relative to a given blade row, it represents the physical blockage due to the presence of each neighboring blade row that has been, in effect, "smeared" by the application of the averaging operators. It is not an additional dependent variable; it may be calculated *a priori* for each blade row in a multiple-blade-row turbomachine. Additionally, the shear stresses in the above viscous vectors include the additional Reynolds stresses, that is, the first term in Equation 2.11. It is important to note also that in Equation 2.12, all of the dependent variables are interpreted as average-passages variables (that is, the triple overbar notation is assumed); for example,

$$u_z \Rightarrow \overline{\overline{\overline{u_z}}},$$

$$\tau_{r\theta} \Rightarrow \overline{\overline{\overline{\tau_{r\theta}}}}, \text{ et cetera.}$$

In this work, the integral form of Equation 2.12 is taken as the basic system of governing equations for the average-passage flow in a multiple-blade-row environment. That is, Equation 2.12 is integrated over a volume and, following an application of Gauss' theorem, the result is

$$\int \frac{\partial}{\partial r_1} (\lambda Q) dV + \oint [\lambda F dA_z + \lambda G dA_r + \lambda H dA_\theta] = \int \lambda K dV - \int \lambda S dV . \quad (2.13)$$

Equation 2.13 forms the basis for the numerical treatment of the average-passage equations.

In summary, carrying out the averaging procedures described in this chapter on the Navier-Stokes equations relative to a given blade row, has resulted in the following. As a result of ensemble averaging, the random fluctuations of the dependent variables associated with turbulent flow have been replaced with an additional mixing (Reynolds) stress acting throughout the flow domain. As a result of time averaging, any blade rows that are rotating relative to the reference blade row have been, in effect, "smeared"; their presence accounted for through a body force distribution in the region occupied by the rotating blade and a mixing stress due to the deterministic unsteady velocity field of the rotating blade row acting throughout the flow domain. As a result of passage-to-passage averaging, all blade rows that are stationary relative to the reference blade row and that do not have integral-multiple blade counts have also been "smeared"; their presence accounted for by an additional body force distribution and mixing stress due to the spatially aperiodic flow associated with the smeared blade row. The resulting average-passage equations thus consist of the Navier-Stokes operator (acting on the average-passage dependent variables relative to a given blade row) plus a series of body force and mixing stress terms. The problem of how to model the body force and mixing stress terms is the closure problem for the average-passage formulation. A simple closure model developed for inviscid flow through a single-stage machine is briefly described in the following section. Though in significantly less detail, it is taken directly from Adamczyk, Mulac, and Celestina [1986].

2.3 Closure Modelling for the Time-Averaged Equations

The focus of this work is to numerically approximate a steady solution to Equation 2.13 for a single-stage turbomachine. A single-stage machine consists of one stationary and one rotating blade row. As mentioned previously, the time-averaged equations in such a case are steady and spatially periodic and, as such, are the average-passage equations. The closure problem is then to model the Reynolds stresses and the body forces and temporal correlations associated with time-averaging. As such, the mixing stress takes the following form:

$$R_{ij} = \overline{\overline{u_i u_j}} + \overline{\overline{u_i}} \overline{\overline{u_j}} , \quad (2.14)$$

where the first term is the time-averaged Reynolds stress and the second term is the mixing stress due to deterministic unsteadiness.

The Reynolds stresses are grouped with the laminar stresses so that they may be modelled using an effective or "eddy" viscosity construction. In this work, the eddy viscosity model is the familiar algebraic model of Baldwin and Lomax [1978]. It is briefly described in the next chapter.

Recall that in Equation 2.13, all of the average-passagge mixing stresses and body force terms were grouped into the source term, S . Adamczyk, Mulac, and Celestina [1986] devised a method for computing S for an inviscid single-stage machine. The method has the very attractive feature that the source term for, say, blade row 1 can be computed from the average-passagge solution for blade row 2 and *vice versa*.

For the body force calculation, it may easily be shown that if it is assumed that the ensemble- and time-averaged pressure loadings of the blades are approximately equal, then, knowing the time-averaged solution for blade row 1, one can calculate its body force representation in the frame of reference of blade row 2. This type of body force representation is axisymmetric. Obviously, this also applies to the body forces due to blade row 2 acting in the frame of reference of blade row 1.

To model the remaining mixing stress terms (that is, the second term in Equation 2.14) in the frame of reference of blade row 1, for example, the following methodology is used. Decompose the i^{th} velocity component in the frame of reference of blade row 1 into two components (for convenience the overbar-hat notation is understood); that is,

$$u_i = u_i^{(2)} + u_i' ,$$

where

u_i = ensemble-averaged, deterministic unsteady velocity component for blade row 1

$u_i^{(2)}$ = velocity component that is steady with respect to blade row 2

u_i' = velocity component that is unsteady with respect to both blade rows.

The second term in Equation 2.14 then becomes

$$\overline{u_i u_j} = \overline{u_i^{(2)} u_j^{(2)}} + \overline{u_i' u_j^{(2)}} + \overline{u_i^{(2)} u_j'} + \overline{u_i' u_j'} .$$

As argued by Adamczyk, Mulac, and Celestina [1986], the correlations involving u_i' can be expected, in general, to be much smaller than those associated with $u_i^{(2)}$. With this in mind, the last three terms in Equation 2.14 are neglected and the following approximation is made:

$$R_{ij} \approx \overline{u_i^{(2)} u_j^{(2)}} . \quad (2.15)$$

In effect, the above approximation asserts that the dominant unsteady correlation for blade row 1 is that due to the steady hydrodynamic loading of blade row 2 and all correlations associated with the blade row interaction velocity field are assumed to be comparatively small and are neglected.

Along with the assumptions regarding the body force calculation for blade row 1, the temporal correlation, Equation 2.15, can be shown to be axisymmetric and can be evaluated from

the steady average-passage flow field of blade row 2. Applying the same assumptions to the body force and temporal correlations from blade row 1 in the frame of reference of blade row 2 will yield completely analogous results. As a result, a rather simple equation can be derived for the total average-passage source for a single-stage turbomachine. For the i^{th} blade row, it is given by

$$\int S(\mathbf{Q}^{(i)}) A dV = A \left\{ L(\mathbf{Q}^{(i)}) - \int K(\mathbf{Q}^{(i)}) dV \right\} - \left\{ L^{AX}(A\mathbf{Q}^{(i)}) - \int K(A\mathbf{Q}^{(i)}) A dV \right\}, \quad (2.16)$$

where

L = surface integral on the left-hand side of Equation 2.13

A = circumferential averaging operator

L^{AX} = axisymmetric form of L

$\mathbf{Q}^{(i)}$ = vector of average-passage dependent variables for the i^{th} blade row.

In words, the average-passage source term for a given blade row is simply the difference between the circumferential average of the three-dimensional flux operator acting on the three-dimensional flow variables and the axisymmetric flux operator acting on the circumferentially-averaged, three-dimensional flow variables. Thus, the governing equations for blade row 1, for example, will be given by

$$\begin{aligned} \int \frac{\partial}{\partial t_1} (\lambda \mathbf{Q}^{(1)}) dV + \oint [\lambda \mathbf{F}^{(1)} dA_z + \lambda \mathbf{G}^{(1)} dA_r + \lambda \mathbf{H}^{(1)} dA_\theta] \\ = \int \lambda \mathbf{K}^{(1)} dV - \int \lambda \mathbf{S}^{(2)} dV, \end{aligned} \quad (2.17)$$

where the superscript refers to the blade row and the last term on the right hand side is given by Equation 2.16 with $i = 2$ (an analogous equation exists for blade row 2).

Another result of the assumed form of the average-passage source term is the property that, at steady-state, the circumferential average of the three-dimensional, average-passage flow fields for both of the blade rows will be identical. In the numerical solution of the average-passage equations, this property of the governing equations will be useful as a global convergence criterion.

2.4 Pseudo-Compressibility and Preconditioning

The differential form of the governing equations (Equations 2.12) does not represent a complete system of time evolution equations--note the zero element in \mathbf{Q} . Because the interest here is in a steady-state solution to Equation 2.12, we are free to alter the time-dependent portion of the governing equation to hasten the achievement of a steady solution. The basic idea is to cast Equation 2.12 in a slightly modified form such that the mathematical character of the modified equation mimics that of the compressible Euler and Navier-Stokes equations. The modified equations may then be treated numerically using techniques developed for the compressible flow equations of motion. This reformulation is referred to as the "pseudo-compressibility" approach and was originally proposed by Chorin [1967] and expanded upon by Turkel [1986], among others.

The pseudo-compressible form of Equation 2.12 is obtained by simply replacing Q in that equation by U where

$$U \equiv \begin{bmatrix} p \\ u_z \\ u_r \\ ru_\theta \end{bmatrix}.$$

In this work, the time derivative in the governing equations is multiplied by a "preconditioning" matrix, P , where

$$P = \begin{bmatrix} \frac{1}{\beta^2} & 0 & 0 & 0 \\ \frac{(\alpha+1)u_z}{\beta^2} & 1 & 0 & 0 \\ \frac{(\alpha+1)u_r}{\beta^2} & 0 & 1 & 0 \\ \frac{(\alpha+1)ru_\theta + \gamma r^2 \Omega}{\beta^2} & 0 & 0 & 1 \end{bmatrix}$$

and α , β , and γ are constant parameters that are used to "tune" the transient behavior of the system to accelerate convergence to a steady-state solution.

The pseudo-compressible form of Equation 2.12 is thus given by the following:

$$P \frac{\partial}{\partial t_1} (\lambda U) + \frac{\partial}{\partial z} (\lambda F) + \frac{1}{r} \frac{\partial}{\partial r} (\lambda r G) + \frac{1}{r} \frac{\partial}{\partial \theta} (\lambda H) = \lambda K - \lambda S. \quad (2.18)$$

Briefly, some elaboration is needed regarding the choice of the preconditioning parameters. It is apparent that for $\alpha = -1$ and $\gamma = 0$ (or $\Omega = 0$), the matrix P becomes the original "artificial compressibility" preconditioner developed by Chorin [1967], with β acting as a pseudo-acoustic speed. Also, for $\gamma = 0$ (or $\Omega = 0$), P becomes the preconditioning matrix developed by Turkel [1986], with α and β acting as parameters to "tune" the wave speeds of the system to maximize convergence to steady state. Turkel [1986] presented some guidelines for choosing the optimal values of α and β . In his work, Turkel [1986] chose α to be a constant and β to be scaled locally with the velocity magnitude. In this work, we chose both α and β to be constants. Additionally, the inclusion of the γ term in the matrix is intended to render the transient behavior of the system independent of the shaft rotation rate Ω . It turns out that if γ is taken to be equal to -1, the eigenvalues of the inviscid flux Jacobians (that is, the signal propagation speeds of the system) can be shown to be algebraically independent of Ω . Based on results obtained in two dimensions for moving cascades, we decided to "hard wire" this value of γ for all of the three-

dimensional calculations. In the cascade calculations, we found that for a given choice of α and β , the convergence to steady-state could be made for any value of the blade speed if γ was equal to -1. For other choices of γ , α and/or β would sometimes require adjustment to obtain convergence for different blade speeds. In summary, for the numerical simulation presented in Chapter 4, we used the preconditioning parameters of $\alpha = 0.0$, $\beta = 2.5$, and $\gamma = -1.0$.

To yield the equations that are to be solved numerically, Equation 2.18 is integrated over a volume. The result can be written as

$$\int P \frac{\partial}{\partial t_1} (\lambda U) dV + \oint [\lambda F dA_z + \lambda G dA_r + \lambda H dA_\theta] = \int \lambda K dV - \int \lambda S dV. \quad (2.19)$$

It can easily be shown that the introduction of pseudo compressibility (that is, substituting the vector U and the matrix P into the governing system of Equation 2.12) changes the inviscid form of the equations ($Re \rightarrow \infty$) to a system of hyperbolic equations analogous to the equations governing inviscid, compressible flow. This is useful in that it permits the use of the large variety of numerical techniques developed for the steady solution of the compressible equations of motion. Here, an explicit finite-volume technique is utilized for the numerical approximation of the steady-state solution of Equation 2.19. This is discussed in the following chapter.

3. Numerical Discretization

In this chapter, the numerical technique utilized to solve the steady-state average-passage equations for a single-stage turbomachine is outlined. First, the spatial discretization is described. It consists of a finite-volume technique along with a model for an artificial dissipation operator necessary for numerical stability. This is followed with a description of the explicit multistage time integration procedure utilized along with several convergence acceleration techniques--local time stepping, implicit residual averaging, and multigrid. Next, the boundary conditions required by the average-passage simulation are briefly described. This chapter ends with a description of the numerical treatment of the average-passage closure models.

3.1 Cell-Centered Finite-Volume Discretization in Space

A generic flow domain is schematically depicted in Figure 3.1 where the relevant coordinate systems are identified. This domain is discretized into a series of contiguous hexahedral cells. The numerical approximation of the governing system of equations, Equation 2.19, begins with the standard cell-centered finite-volume discretization for hexahedra. That is, for a hexahedral cell, Equation 2.19 is numerically integrated in space to yield

$$\begin{aligned} P_{ijk} \frac{d}{dt_1} (\lambda U)_{ijk} Vol_{ijk} + \sum_{m=1}^6 [(\lambda F A_z)_m + (\lambda G A_r)_m + (\lambda H A_\theta)_m]_{ijk} \\ = (\lambda K)_{ijk} Vol_{ijk} - (\lambda S)_{ijk} Vol_{ijk} , \end{aligned} \quad (3.1)$$

where the subscript "ijk" denotes the $(i,j,k)^{th}$ control volume or cell, m denotes the m^{th} face of the cell, Vol denotes the cell volume, and A_z , A_r , and A_θ are components of the outward directed area of a cell face.

In Equation 3.1, the dependent variables are defined at the center of a control volume and are taken to be an average value for the cell. Figure 3.2 depicts the $(i,j,k)^{th}$ cell with its defining grid points. The cell volume is computed using a tetrahedron decomposition procedure. The directed areas in Equation 3.1 are computed using the cross product of the diagonals of each cell face. Figure 3.3 shows the directed areas of a typical cell.

If all of the spatial terms in Equation 3.1 are collectively denoted by E , then Equation 3.1 may be written more simply as

$$\frac{d}{dt_1} (\lambda U)_{ijk} Vol_{ijk} + P_{ijk}^{-1} E(U)_{ijk} = 0 . \quad (3.2)$$

The portions of E representing facial fluxes are approximated using simple arithmetic averaging of neighboring cell-centered quantities. As such, it may be easily shown that for uniformly spaced grids in cylindrical coordinates, Equation 3.2, in its present form, amounts to a central-difference approximation to Equation 2.18. It is well known that central-difference approximations of the Euler equations or high Reynolds number Navier-Stokes equations requires the addition of some

artificial damping terms for stability. With the inclusion of these terms, Equation 3.2 becomes

$$\frac{d}{dt_1}(\lambda U)_{ijk} Vol_{ijk} + P_{ijk}^{-1} E(U)_{ijk} + D(U)_{ijk} = 0 , \quad (3.3)$$

where D is the artificial dissipation operator.

3.2 Artificial Dissipation

The artificial dissipation operator used in this work is modelled after the operator originally proposed by Jameson, Schmidt, and Turkel [1981] for transonic flow, with modifications for highly-stretched grids suggested by Martinelli [1987]. In the present implementation, the assumption of pseudo-compressibility results in some slight modifications and simplifications.

The purpose of adding artificial dissipation terms is to provide damping of error waves in the solution domain. An effective operator can be constructed by looking at the natural dissipation inherent in upwind differencing. In other words, a form for the dissipation operator can be suggested by determining what form D should take so that when it is combined with the central-differenced, preconditioned convection terms (as in Equation 3.3), the result will approximate an upwind differencing of just the preconditioned convection terms. The actual form of the dissipation will depend on the type of upwind differencing considered; first-order upwinding will result in a Laplacian form for D , while second-order upwinding will yield a D of biharmonic form. In both cases, the proper form for the dissipation will scale with the signal propagation speeds (or wave speeds) of the preconditioned convection terms. The signal propagation speeds are determined by the eigenvalues of the flux Jacobian matrices formed by the inviscid flux vectors F_i , G_i , and H_i .

Jameson, Schmidt, and Turkel [1981] originally devised an artificial dissipation operator that was a combination of second- and fourth-difference operators with the relative amounts of each determined by the flow solution. Additionally, both terms in his operator were scaled by the maximum wave speeds or, more precisely, by the spectral radii of the inviscid flux Jacobians. Although their original implementation was for transonic flow, the same methodology for the construction of the dissipation operator is followed in this work.

In a three-dimensional application (such as in this work), the dissipation operator is constructed separately in each of the coordinate directions using the above methodology. The general form of the operator can thus be written as

$$D(U)_{ijk} = D_\eta(U)_{ijk} + D_\zeta(U)_{ijk} + D_\xi(U)_{ijk} , \quad (3.4)$$

where η , ζ , and ξ denote the i , j , and k computational directions, respectively. Note, in the following, for illustrative purposes, only the η -direction is considered in detail; the other directions follow analogously.

Following the original formulation, a fully conservative dissipation operator is constructed containing both second and fourth differences with, for example,

$$D_\eta(U)_i = -(d_{i+\frac{1}{2}} - d_{i-\frac{1}{2}}) , \quad (3.5a)$$

where

$$d_{i+\frac{1}{2}} = (\epsilon_{i+\frac{1}{2}}^{(2)} \Delta_\eta - \epsilon_{i+\frac{1}{2}}^{(4)} \Delta_{\eta\eta\eta}) U_{i+\frac{1}{2}} \quad (3.5b)$$

and Δ_η and $\Delta_{\eta\eta\eta}$ are undivided first and third difference operators in the η -direction (note that the subscripts j and k are implied in all terms). For the coefficients $\epsilon^{(2)}$ and $\epsilon^{(4)}$, eigenvalue scaling is used. Specifically, these coefficients are defined to be proportional to a blending of the spectral radii of the preconditioned inviscid flux Jacobians in Equation 3.3; the reason for the blending will be described shortly. The second and fourth-difference dissipation scale factors are given by

$$\epsilon_{i+\frac{1}{2}}^{(2)} = \frac{1}{2} \kappa^{(2)} \phi_{\eta, i+\frac{1}{2}} \min(\nu_{i+\frac{1}{2}}, 1.0) \quad (3.6a)$$

and

$$\epsilon_{i+\frac{1}{2}}^{(4)} = \max\left(\frac{1}{4} \kappa^{(4)} \phi_{\eta, i+\frac{1}{2}} - \epsilon_{i+\frac{1}{2}}^{(2)}, 0.0\right) , \quad (3.6b)$$

where

$$\nu_{i+\frac{1}{2}} = \max(\nu_i, \nu_{i+1}) \quad , \quad \nu_i = \left| \frac{p_{i-1} - 2p_i + p_{i+1}}{p_{i-1} + 2p_i + p_{i+1}} \right| , \quad (3.7)$$

$$\phi_\eta = \frac{1}{3} \Psi_\eta \left\{ 1 + \left[\frac{\Psi_\zeta}{\Psi_\eta} \right]^\delta + \left[\frac{\Psi_\xi}{\Psi_\eta} \right]^\delta \right\} , \quad (3.8)$$

and

$$\Psi_\eta = \lambda \psi_\eta , \quad \Psi_\zeta = \lambda \psi_\zeta , \quad \Psi_\xi = \lambda \psi_\xi .$$

In the above, ψ_η , ψ_ζ , and ψ_ξ are the maximum wave speeds in the respective computational coordinate directions and λ is the geometric blockage factor. For example, in the η -direction,

$$\psi_\eta = \frac{1}{2} \left(q_\eta + \sqrt{q_\eta^2 + 4\beta^2 S_\eta} \right), \quad (3.9)$$

where

$$q_\eta = (1 - \alpha)(V \cdot A^\eta),$$

$$S_\eta = A^\eta \cdot A^\eta,$$

$$A^\eta = A_z^\eta e_z + A_r^\eta e_r + A_\theta^\eta e_\theta,$$

and

V = velocity vector

A^η = the directed area of an $\eta = \text{constant}$ cell face

e_z , e_r , and e_θ = unit vectors in the z , r , and θ directions, respectively.

Also in the above, ϕ_η is the blending function for the eigenvalue scaling in each of the coordinate directions. This blending has been found to be useful for flow solutions using highly-stretched computational grids by Martinelli [1987]. The purpose of this function is to combine the artificial dissipation scale factors (that is, the spectral radii of the inviscid flux Jacobians) in each of the coordinate directions so that no one coordinate direction is artificially damped significantly more than any other. Note that the exponent δ in the definition of the blending function determines the level of blending; for example,

$\delta = 0$ scales the dissipation independently in each direction (anisotropically)

and

$\delta = 1$ scales the dissipation identically in each direction (isotropically).

For typical high Reynolds number grids, $\delta \approx 0.50$ has been found to be adequate.

There are two other constants that have to be set by the user in Equation 3.5b; these are $\kappa^{(2)}$ and $\kappa^{(4)}$. The factors of 1/2 and 1/4 in Equations 3.6a and 3.6b are included so as to confine the typical values of $\kappa^{(2)}$ and $\kappa^{(4)}$ to the range of 0.0 to 1.0.

In Equation (3.6a), v can be interpreted as a pressure gradient "switch" that locally alters the artificial dissipation depending on the gradients present in the flow field. This function essentially measures the rate of change of the pressure gradient in a particular coordinate direction. The way in which this function is incorporated in the definitions of the artificial dissipation scale

factors results in $\epsilon^{(4)}$ tending to zero in regions of rapid change in pressure gradient; while in the same regions, $\epsilon^{(2)}$ approaches its maximum value. Conversely, in regions where the pressure gradient is only slowly varying, the second-difference artificial dissipation will approach zero and there will remain only a background level of fourth-difference artificial dissipation. In the original (compressible flow) implementation of this type of blended artificial dissipation, the intention was the sharp capture of shock waves. Near shock waves it was found that the fourth-difference artificial dissipation would cause overshoots that could negatively effect convergence. If, however, the fourth-difference portion of the operator was turned off in the vicinity of a shock and the second-difference portion increased, shocks could be captured without overshoots. Of course, this rendered the solution only first-order accurate near shocks, but it would remain second-order accurate in smooth regions of the flow field. Although this work deals exclusively with incompressible, shock-free flow, this type of formulation is preserved for handling the possibility of nearly discontinuous, shock-like structures that may appear during the transient. In most situations, however, this blended dissipation is not necessary for convergence. For this reason, the following special cases are included in the formulation:

If $\kappa^{(4)} = 0$, then

$$\epsilon_{i+\frac{1}{2}}^{(2)} = \frac{1}{2} \kappa^{(2)} \phi_{\eta, i+\frac{1}{2}}$$

and

$$\epsilon_{i+\frac{1}{2}}^{(4)} = 0.0 ;$$

while if $\kappa^{(2)} = 0$, then

$$\epsilon_{i+\frac{1}{2}}^{(2)} = 0.0$$

and

$$\epsilon_{i+\frac{1}{2}}^{(4)} = \frac{1}{4} \kappa^{(4)} \phi_{\eta, i+\frac{1}{2}} .$$

In other words, by choosing either of the constants to be zero, the dissipation operator can be made independent of the switching function and, as such, represent a pure second-difference or a pure fourth-difference dissipation. Therefore, in these special cases, the coefficients $\kappa^{(2)}$ and $\kappa^{(4)}$ approximately represent the fraction of the equivalent dissipation that would be present from first-order or second-order upwind discretizations of the inviscid convection terms in the governing equations. For example, choosing $\kappa^{(2)} = 0.10$ and $\kappa^{(4)} = 0.0$ implies a level of numerical dissipation of approximately ten percent of the level that would be present if first-order upwinding were used for the convection terms.

The boundary treatment for the artificial dissipation follows that of Rizzi and Eriksson [1985]. Basically, the boundary and near-boundary cells are handled in a way that

ensures that both the second- and fourth-difference operators remain dissipative at the extremes of the domain.

3.3 Time Integration

To facilitate the description of the time stepping methodology, the residual is defined as

$$R(U)_{ijk} \equiv P_{ijk}^{-1} E(U)_{ijk} + D(U)_{ijk} . \quad (3.10)$$

It is important to note that this residual is composed of a number of distinct elements--recall that the vector E contains all of the discretized, physical spatial terms (that is, inviscid and viscous fluxes, as well as the radial momentum and average-passage source terms) and the vector D is the artificial dissipation operator described in Section 3.2. This has important consequences in the implementation of the time stepping scheme. Using the residual definition, Equation 3.10, the discrete governing equations may be written as

$$\frac{d}{dt_1} (\lambda U)_{ijk} Vol_{ijk} + R(U)_{ijk} = 0 . \quad (3.11)$$

Equation 3.11 is then integrated in time to a steady-state solution using the explicit "hybrid multistage" scheme of Jameson, Schmidt, and Turkel [1981]. In its simplest manifestation, this four-stage Runge-Kutta-like scheme takes on the following form for the $(i,j,k)^{th}$ cell at the n^{th} time step:

$$\begin{aligned} U^{(1)} &= U^n - \alpha_1 \frac{\Delta t}{\lambda Vol} R(U^n) \\ U^{(2)} &= U^n - \alpha_2 \frac{\Delta t}{\lambda Vol} R(U^{(1)}) , \\ U^{(3)} &= U^n - \alpha_3 \frac{\Delta t}{\lambda Vol} R(U^{(2)}) \\ U^{n+1} &= U^n - \alpha_4 \frac{\Delta t}{\lambda Vol} R(U^{(3)}) \end{aligned} \quad (3.12)$$

where

$$\alpha_1 = 0.250, \alpha_2 = 0.333, \alpha_3 = 0.500, \alpha_4 = 1.000 ,$$

and the bracketed numerical superscripts denote provisional values.

It turns out that evaluating the entire residual at each stage in Equation 3.12 can be very expensive (for example, the artificial dissipation operator, D , is roughly twice as expensive to

evaluate as just the inviscid portion of E). In practice, it has been found that it is sufficient to evaluate the physical dissipation and artificial dissipation portions of R at the first stage only and freeze their values through subsequent stages. This technique has only a very small detrimental effect on the size of the permissible time step, while saving significant computational time. This selective evaluation of the different pieces of the residual at each stage is what distinguishes this type of scheme from a true Runge-Kutta scheme.

In this work, a slightly different four-stage scheme is used. The coefficients for the scheme presently used are

$$\alpha_1 = 0.250, \alpha_2 = 0.500, \alpha_3 = 0.550, \alpha_4 = 1.000 .$$

This scheme was chosen because of its more effective high wave number damping characteristics relative to the "standard" scheme. Although the permissible time step for this scheme is slightly less than the standard scheme, its high wave number damping gives it superior multigrid performance and overall faster convergence.

3.4 Convergence Acceleration

Several techniques are utilized to hasten the attainment of a steady-state solution to Equation 3.3. The techniques used are: local time stepping, implicit residual averaging, and multigrid.

3.4.1 Local Time Stepping

Because the time coordinate in the governing equations is purely artificial, the transient behavior of the system may be freely manipulated to accelerate convergence to steady state (the introduction of the preconditioning matrix, P , was the first instance of this sort of manipulation). The rate of convergence is determined by how quickly errors can be removed from the solution domain. There are essentially three mechanisms by which errors can be removed from the domain. They can be damped by numerical (or physical) diffusion; they can be transported with the flow through the outflow boundary; or they can propagate "acoustically" out of the domain in any direction. Excessive numerical damping will have a detrimental effect on the steady-state solution. As such, the amount of artificial dissipation is generally kept as low as possible. The most effective way to increase the convergence rate, therefore, is to maximize the computational rate at which information is propagated throughout the domain, or, in other words, to minimize the number of time steps necessary to propagate a signal over a given distance. This is most easily done by advancing the solution for each cell in the domain through the maximum possible time step for that cell.

To determine the maximum allowable time step, a Fourier analysis is carried out on a linearized form of the governing equations in generalized curvilinear coordinates. The result of this analysis is a time step determined by two conditions imposed by the inviscid and viscous portions of the governing equations. The inviscid limitation on the permissible time step is the

familiar Courant-Friedrichs-Lewy (CFL) condition for the hyperbolic Euler equations. In this case, it is formed directionally in the following way:

$$(\Delta t_I)_{ijk} = CFL \left[\frac{1}{\Delta t_\eta} + \frac{1}{\Delta t_\zeta} + \frac{1}{\Delta t_\xi} \right]_{ijk}^{-1}, \quad (3.13)$$

where the subscript "I" denotes inviscid and CFL is a stable Courant number for the multistage scheme in Equation 3.12. The directional time steps are functions of the maximum wave speeds (flux Jacobian spectral radii) in the respective computational coordinate directions. For example, in the η -direction,

$$(\Delta t_\eta)_{ijk} = \left[\frac{Vol}{\psi_\eta} \right]_{ijk}, \quad (3.14)$$

where ψ_η is as given in Equation 3.9; however, here the average value for a cell is used. The ζ and ξ directions follow analogously.

The viscous limitation on the permissible time step is a result of the parabolic or diffusive portions of the governing equations. As such, it has terms dependent on the physical as well as artificial dissipation operators in Equation 3.3. To derive the viscous stability bound, the methodology described by Kunz and Lakshimarayana [1992] was applied to the preconditioned pseudo-compressible equations of motion. The resulting viscous time step limit can be expressed in the following way if the assumption of grid orthogonality is made:

$$(\Delta t_V)_{ijk} = VON \left[\frac{Vol}{\Gamma_\eta + \Gamma_\zeta + \Gamma_\xi} \right]_{ijk}, \quad (3.15)$$

where the subscript "V" denotes viscous and VON is a stable von Neumann number for the multistage scheme. The directional factors in the denominator have the following form:

$$(\Gamma_\eta)_{ijk} = \left[\frac{4\nu_T S_\eta}{Vol} + 4\epsilon_\eta^{(2)} + 16\epsilon_\eta^{(4)} \right]_{ijk},$$

where

$$\nu_T = \frac{1 + \nu_e}{Re}$$

and ν_e is the eddy viscosity. The values of $\epsilon_\eta^{(2)}$ and $\epsilon_\eta^{(4)}$ for a cell are computed using the average values of Equations 3.6a and 3.6b in the η -direction for that cell. The ζ and ξ directions follow analogously.

The value of the allowable time step for a particular cell is then determined by simply taking the more restrictive of the two limits (Equations 3.13 and 3.15)--that is,

$$\Delta t_{ijk} = \min(\Delta t_I, \Delta t_V)_{ijk} . \quad (3.16)$$

Stable values for CFL and VON can be determined from an examination of the amplification factor of the multistage scheme (Equation 3.12). Figure 3.4 shows contours of the amplification factor for the scheme used in this work. The outer boundary of this region is the unit amplification contour--that is, neutral stability. The maximum allowable Courant number is equal to the intercept of the unit contour with the imaginary axis, while the maximum allowable von Neumann number is given by the unit contour's intersection with the negative real axis. A safe way to choose CFL and VON is to choose them such that the rectangle that they define lies completely within the stability region. For the multistage scheme used in this work, a good choice is

$$CFL = 2.0 , \quad VON = 1.0 ,$$

with the corresponding rectangle shown in Figure 3.4.

3.4.2 Implicit Residual Averaging

Another widely used technique for accelerating the convergence of Runge-Kutta-type schemes is residual averaging (or smoothing). The basic idea is to increase the allowable Courant and von Neumann numbers (and, hence, the size of the local time step) by increasing the spatial support of the discrete approximation. One way to do this is to increase the number of stages in the multistage scheme. Unfortunately, this is rather expensive computationally. Another way to increase spatial support is to spatially average the residuals in some way. That is, replace the residual, R , for a given cell with a new residual computed using residual information from neighboring cells. Jameson [1983] found it most effective to carry out this averaging implicitly. It turns out that increasing the time step a given amount in this manner is cheaper computationally than adding more stages to the time integration. Also, implicit residual averaging has no imposed upper bound on the size of the increase in time step, as does the inclusion of additional stages (there are practical limits, however).

Basically, residual averaging consists of the replacement of the residual, R , for a cell, defined by Equation 3.10, with an implicitly-averaged residual, R^* , where R^* is the solution to the following:

$$(1 - \epsilon_\eta \Delta_{\eta\eta})(1 - \epsilon_\zeta \Delta_{\zeta\zeta})(1 - \epsilon_\xi \Delta_{\xi\xi})R^* = R . \quad (3.17)$$

In Equation 3.17, $\Delta_{\eta\eta}$, $\Delta_{\zeta\zeta}$, and $\Delta_{\xi\xi}$ are undivided second-difference operators and ϵ_η , ϵ_ζ , ϵ_ξ are smoothing factors in the respective computational coordinate directions. In this work, the smoothing factors are taken to be constants typically in the range of 0.0 to 1.0 (For the results shown in Chapter 4 they were each equal to 1.0.). Equation 3.17 is solved by three successive block tridiagonal sweeps through the domain. In practice, it is sufficient to replace the residuals in Equation 3.12 at the second and last stages only. This is sufficient to approximately double the allowable time step.

3.4.3 Multigrid

A multigrid strategy based on the technique outlined by Jameson and Baker [1984] is also implemented as a convergence acceleration technique. Its implementation in a compressible average-passage formulation is outlined by Kirtley, Beach, and Adamczyk [1990]. Here, its application to the preconditioned, pseudo-compressible, average-passage equations is briefly described.

The primary advantage of using a multigrid technique for the steady-state solution of the Euler or Navier-Stokes equations is the effectiveness of the multigrid procedure in eliminating low wave number errors from the solution domain. This is especially attractive in the current application to turbomachine simulation for the following reason: The boundary conditions used in this work require that the exit hub static pressure be periodically adjusted (or throttled) to draw the correct mass flow through the machine. In the case of rotors, it is essential that the correct (or design) mass flow be simulated, as otherwise, the flow incidence angles and, hence, pressure loading of the rotor blades will be incorrect. Each time the back pressure is adjusted, a pressure wave is sent upstream to readjust the flow accordingly. These pressure waves are of very long wavelength and, as such, are slow to be removed by the multistage algorithm. The multigrid procedure is a means by which long wavelength errors like these can be quickly removed by performing intermediate iterations on coarsened grids where the waves appear with higher wave numbers.

In this work, a standard "V-cycle" multigrid algorithm is utilized. The cycle consists of a series of multistage iterations on progressively coarser grids. Each coarse grid iteration includes a forcing function derived from information obtained from finer grid solutions. Once the coarsest grid in the sequence is reached and the corrections to the flow variables on this grid are computed by advancing the solution through a multistage iteration (or time step), a series of interpolation steps follow where corrections on each coarsened grid are interpolated to progressively finer grids. Ultimately, the flow variables on the finest grid are corrected and the cycle can begin again.

Although the multigrid algorithm can theoretically be carried out over as many grid coarsenings as the finest grid can be evenly divided into, the current implementation of the scheme is limited to two grid coarsenings—that is, a three-level, V-cycle multigrid.

Specifically, upon completion of a fine-grid iteration (or time step), the flow variables on the fine (h) grid are restricted to a coarsened ($2h$) grid by the following volume-weighted average:

$$U_{2h} = \frac{\sum_8 \lambda_h U_h Vol_h}{\sum_8 \lambda_h Vol_h} , \quad (3.18)$$

where the summation is over the eight fine-grid cells that make up one coarse-grid cell. A forcing function is computed so that fine-grid accuracy is maintained for an iteration on the coarsened grid.

For the $2h$ grid, it is given as

$$f_{2h} = R(U)_{2h} - \sum_8 R(U)_h, \quad (3.19)$$

where $R(U)_{2h}$ is the residual computed on the coarse grid using the restricted variables from the fine grid. With the above definitions, the m^{th} stage of the multistage scheme on the $2h$ grid will look like

$$U_{2h}^{(m)} = U_{2h}^n - \alpha_m \left[\frac{\Delta t}{Vol} \right]_{2h} \left\{ R(U)_{2h}^{(m-1)} - f_{2h} \right\}. \quad (3.20)$$

One further coarsening is carried out to a $4h$ or doubly-coarsened grid, with U_{4h} defined analogously to Equation 3.18. The forcing function on this grid is given as

$$f_{4h} = R(U)_{4h} - \sum_8 \left\{ R(U)_{2h} - f_{2h} \right\}. \quad (3.21)$$

The m^{th} stage of the multistage scheme for the $4h$ grid is then simply given by Equation 3.20 with the $2h$ subscripts everywhere replaced by $4h$. Upon completion of a time step on the $4h$ grid, the corrections to the $4h$ flow variables are then prolonged (interpolated) to the $2h$ grid using simple tri-linear interpolation. The modified $2h$ flow variables are then used to calculate corrections to the flow variables on the $2h$ grid. These corrections are then prolonged to the fine grid. The corrected variables on the fine grid are then used to initiate the next fine-grid iteration and a three-level multigrid cycle is complete.

It is important to note that on both of the coarsened grids ($2h$ and $4h$), only the inviscid portions of the residuals are computed. That is, $R(U)_{2h}$ and $R(U)_{4h}$ are essentially Euler operators and, as such, no-flux solid surface velocity boundary conditions are applied on these grids regardless of whether the fine-grid flow is viscous or inviscid. All other boundary conditions on the coarsened grids are the same as those used on the fine grid. Also, just as in the case of a single-grid calculation, the coarsened-grid residual operators include an artificial dissipation operator. Unlike the fine-grid calculation, however, the operator on $2h$ and $4h$ grids is a pure second-difference operator. This is done to ensure effective high wave number damping on the coarsened grids. Finally, all of the viscous effects and multiple-blade-row effects (average-passage source) are "felt" on the coarsened grids through the presence of the fine-grid residual in the definitions of the forcing functions, f_{2h} and f_{4h} .

3.5 Boundary Conditions

In a blade passage, there are four distinct types of boundaries: inflow, outflow, solid surface, and periodic. Figure 3.5 depicts schematically the boundary condition types and locations for a typical blade passage. As this is a cell-centered finite-volume discretization, all boundary conditions are satisfied with the use of "phantom" cells located outside of the physical domain. The boundary conditions utilized for solid surfaces differ depending on whether the flow is viscous

or inviscid. For all other types of boundaries, the boundary conditions are the same for either type of flow.

Consistent with the hyperbolic character of the inviscid preconditioned pseudo-compressible equations of motion, at an inflow boundary, three conditions must be specified and a fourth extrapolated from inside the flow domain. In this work, for both inviscid as well as viscous flow, the total pressure and two absolute flow angles are specified at the inflow plane; the static pressure is extrapolated from the interior.

At an outflow boundary, the character of the governing equations dictates that one condition be specified and three other conditions extrapolated from the interior. Here, the static pressure along the hub at the outflow plane is specified and integrated outward using simplified radial equilibrium--that is,

$$\frac{\partial p}{\partial r} = \frac{u_\theta^2}{r} . \quad (3.22)$$

Also at this boundary, all three velocity components are extrapolated from the interior solution.

Recall that the governing preconditioned pseudo-compressible average-passage equations are, by definition, periodic over the pitch of a blade passage. As such, all flow variables are taken to be periodic upstream and downstream of the blade surfaces and in any hub or tip gap regions above or below the blades.

On the blade, hub, and shroud (casing) surfaces, different boundary conditions are employed depending on whether the flow is inviscid or viscous. For inviscid flow, the solid surface boundary condition for velocity is the familiar no-flux condition, while the pressure is obtained by an application of the normal momentum equation for the surface in question. For viscous flows, where there is adequate grid resolution in the boundary layer, a no-slip condition is satisfied for the velocity components. For higher Reynolds number calculations where grid resolution is a problem, there is also a viscous slip velocity condition, where the slip velocity is determined by a law-of-the-wall-based wall function. For both cases, the wall pressure is determined by assuming a zero normal pressure gradient at the wall. Also, as mentioned by Kirtley, Beach, and Adamczyk [1990], some minor additional terms are included in the hub and shroud boundary conditions to ensure that a common axisymmetric solution is converged upon by all blade rows.

3.6 Closure Modelling

This work deals with the calculation of the average-passage flow fields associated with a single stage turbomachine--that is, two blade rows. As such, the closure issues are concerned with only the ensemble averaging and the time averaging. Specifically, these are the first two terms in the mixing stress relation of Equation 2.11, in addition to the blade force terms resulting from the time averaging of the momentum equations.

3.6.1 Reynolds Stress Closure

The time-averaged Reynolds stress (the first term in Equation 2.11) is modelled using a familiar eddy viscosity construction. Specifically, the algebraic eddy viscosity model of Baldwin and Lomax [1978] is used. This model is a two-layer mixing-length-type model where the relevant length scale is based on the distance to the nearest wall. In the current application, no special corner treatment is utilized. In the wakes, a simple extrapolation procedure is used based on the eddy viscosity distribution at the trailing edge. This extrapolation procedure assumes that the axial grid lines approximately follow the downstream trajectory of the wake. The eddy viscosity distribution at the trailing edge is then exponentially decayed along these grid lines, as suggested by Adamczyk [1992]. To ensure that a common circumferentially-averaged flow field is obtained for all blade rows in a multiple-blade-row environment, the computed eddy viscosity for a blade passage is modified as described by Kirtley, Beach, and Adamczyk [1990].

3.6.2 Average-Passage Closure

The temporal correlations (mixing stresses) and body forces resulting from the application of the time-averaging operator to the Reynolds-averaged Navier-Stokes equations are computed using a discretized version of the technique described in Section 2.3. Recall that the methodology in Section 2.3 was formulated to calculate only that portion of the temporal correlation for a given blade row due to the velocity components that are steady with respect to neighboring rotating blade rows. What follows is a brief outline of how, in practice, the average-passage flow fields for a two-blade-row turbomachine are determined. It follows the method described by Adamczyk, Mulac, and Celestina [1986].

The form of the governing average-passage equations suggested by Equation 2.16 implies that the flow fields are to be calculated simultaneously. In practice, however, a two-level iteration procedure is used. In the inner iterations, the flow fields for the individual blade passages are updated using the multistage algorithm with the average-passage source term fixed. In the outer iteration, the average-passage source terms are updated according to the formula from Section 2.3.

For example, at the end of a series of iterations on the three-dimensional flow field through, say, blade row 1, the average-passage source term is calculated using a discrete version of Equation 2.15 with $i=1$. Next, a series of iterations is calculated for the three-dimensional flow through blade row 2 utilizing the average-passage source term just calculated from the result for blade row 1. Upon completion of these iterations, the average-passage source term for blade row 2 is computed using the discretized Equation 2.15 with $i=2$. Blade row 1 is then restarted with this updated source term and the cycle repeats. This periodic "flipping" between blade rows using updated average-passage source terms is what is referred to as the outer iterations. In effect, at the

4. Comparison of Numerical and Experimental Results

The previous chapters have described the average-passage equations for a multiple-blade-row turbomachine and the numerical technique used to solve these equations. This description includes a method to model the closure problem associated with a two-blade-row machine. In this chapter, we use the resulting computer code (ISTAGE) to predict the flow through a two-blade-row pump. As a first step towards code validation, this chapter presents comparisons between these numerical predictions and experimentally measured data.

4.1 High Reynolds Number Pump Experiment

Zierke, Straka, and Taylor [1993] acquired a large quantity of data within their high Reynolds number pump (HIREP) facility. Figure 4.1 shows a computer-generated graphical image of the HIREP blades and the cylindrical coordinate system used for analyzing the experimental data. This isometric view shows that HIREP contains 13 inlet guide vanes and 7 rotor blades with a significant circumferential blade lean or skew. The hub has a constant diameter of 21 inches, while a tunnel liner creates a casing endwall with a constant diameter of 42 inches. Using this nominal blade diameter, Zierke, Straka, and Taylor [1993] found a rotor blade tip speed of $U_{tip} = 47.6$ ft/sec while operating at the design point with 260 rpm. Most of the data were acquired at this design point. The experimental measurement techniques included rotor shaft torque and thrust cells, blade static-pressure taps, oil-paint surface flow visualization, cavitation visualization, laser light sheet visualization, slow- and fast-response pressure probes, and a two-component, laser Doppler velocimeter (LDV). Five-hole pressure probe measurements of the inflow, 37% chord axially upstream of the inlet guide vanes, showed a nearly uniform, axial flow with a nominal reference velocity of 35 ft/sec. However, the measurements indicated that the casing endwall boundary layer was fully turbulent with a boundary layer thickness of 0.71 inches. The turbulent boundary layer on the hub was slightly less than 0.3 inches.

Since this experiment involved the incompressible flow of water through a two-blade-row machine, the resulting database yields an excellent test case for this particular code. In addition, with chord Reynolds numbers as high as 5,500,000, the database also gives a very challenging test case.

4.2 Grid Generation

Using the algebraic grid generation code of Beach [1990] and Beach and Hoffman [1992], we generated a computational grid for the single-stage HIREP geometry. This grid generator was written specifically for the compressible average-passage formulation. Basically, this interactive grid generator creates stacked, body-conforming, H-type grids for multiple-blade-row turbomachines.

A two-blade-row average-passage calculation (like HIREP) requires a total of three grids. There are two three-dimensional grids: one for an inlet guide vane (IGV) passage and one for a rotor blade passage. Each of these grids extends from an inlet plane upstream of the inlet guide vanes to an exit plane downstream of the rotor blades. Figures 4.2 and 4.3 shows slices of these

grids. The three-dimensional grids used in this work contain 141 axial grid points and 45 points in both the radial and tangential directions. Additionally, a common two-dimensional grid exists that defines the meridional domain (that is, the extent in the r,z -plane) of the turbomachine. It also contains 141 axial and 45 radial grid points. Figure 4.4 shows this two-dimensional grid for the HIREP geometry. It is through this plane that the two three-dimensional solutions "communicate." Body forces and correlations computed from the three-dimensional solution for one blade row are computed on this plane and are subsequently introduced into the three-dimensional domain of the other blade row. Kirtley, Beach, and Adamczyk [1990] describe the interpolation procedure necessary to accomplish this interaction.

In this application, we generated the three-dimensional grid for the rotor as if the blade physically extended from the hub all the way to the casing with no tip clearance. In reality, the HIREP rotor included a nominal tip clearance of approximately 0.13 inches. To model the clearance flow, therefore, we chose a grid index that most closely approximated the location of the physical blade tip. A periodic boundary condition was then used for all eight cells between the tip index and the casing. In other words, above the rotor blade tip, a periodic condition was imposed across the thickness of the blade tip section. Note that we chose the tip grid index to correspond to the physical blade tip and did not include a discharge coefficient to model the *vena contracta* that occurs when the tip clearance flow separates. The HIREP rotor blades had a rounded pressure side corner at the blade tip to prevent this separation and, thus, improve gap cavitation performance.

In reality, both the inlet guide vanes and the rotor blades have fillets at their junctures with the hub and casing. Each inlet guide vane, therefore, includes a fillet at its root and tip, while each rotor blade includes a fillet at the root only (while the tip includes the rounded pressure side corner). These fillets, however, are absent from the computational grid. Neither gridding the true blade tip nor gridding fillets is technically beyond the capabilities of the grid generation code; however, making the simplifications just described does greatly simplify the grid generation process. Moreover, neither geometric simplification should introduce undue error into the computational results.

4.3 Solution Procedure

The major assumption in the simulation of HIREP was the state of the incoming flow. Without prior knowledge of this inflow, we used the design inflow (from a streamline curvature simulation). The design inflow was simply uniform axial flow. Zierke, Straka, and Taylor [1993] subsequently found from measurements of the actual flow field that a relatively thick boundary layer existed on the casing endwall upstream of the inlet guide vanes. It is believed that the absence of this boundary layer in the simulation may be quite important to some of the results—an effect that we will later address.

Actually obtaining the average-passage solution for the HIREP geometry involved running the computer code until a steady-state solution was reasonably approximated. Running the code involved a series of "flips" between the two blade rows. Each "flip" for a given blade row consisted of the calculation of a number of time steps (perhaps several hundred) on the three-dimensional grid for that blade row using the (axisymmetric) average-passage body forces and correlations from the other blade row from the previous "flip." During the "flipping" of the

solutions, we monitored the mass flow. If the mass flow through HIREP was too high or too low, we adjusted the exit hub static pressure (back pressure) accordingly. This "throttling" of the simulation was a direct result of the total pressure/absolute flow angle inflow boundary condition discussed in the previous chapter. The simulation was considered converged when the calculated mass flow equaled the design mass flow and both blade rows had converged to the same circumferentially-averaged flow field (recall that this was a necessary convergence criterion for the average-passage equations). For the HIREP simulation, the calculated mass flow was about 1% lower than the design mass flow.

4.4 Comparisons

Using the computational grid generated for the HIREP geometry and the solution procedure just described, we obtained a converged solution for the HIREP flow field. First, we shall discuss the simulation of the IGV flow field—including comparisons with the experimental database. Then, we shall examine the flow field in the vicinity of the downstream rotor blades.

4.4.1 Inlet Guide Vanes

The first step in understanding the basic characteristics of a turbomachine flow field normally involves observation of the blade static-pressure distribution. For the IGV static pressures, Figure 4.5 shows a comparison between numerical and experimental results at five spanwise locations. Note that, in this figure, the pressure coefficient, K_p , is normalized by a dynamic pressure based on the blade tip speed—as defined by Zierke, Straka, and Taylor [1993]. Overall, the integrated blade loading agrees reasonably well at all five locations. As each section is examined individually, we observe some differences in the predicted and measured distributions of pressure.

At 10% span, a discrepancy exists between the prediction and experiment in the distribution of pressure near the leading edge. At this location, lower pressures were measured than were predicted on both the suction and pressure surfaces. Note that a similar discrepancy at this spanwise location was observed when Zierke, Straka, and Taylor [1993] compared the measurements to a lifting surface theory calculation of the flow field. In the midspan regions (from 30% to 70% span), the suction surface pressures compare quite well with the measurements. However, at these same locations, on the pressure surface, the predictions show a distinct favorable pressure gradient near the trailing edge that is not present in the measurements. This phenomenon reverses itself at the 90% span location, where a favorable pressure gradient was measured and an adverse pressure gradient was predicted.

The contour plots of Figures 4.6 and 4.7 reinforce these previous observations. Notice that the contours of measured static pressures are not extrapolated beyond the locations of the pressure taps. Figure 4.6 shows good qualitative agreement over the entire suction surface. For the pressure surface, on the other hand, Figure 4.7 shows good agreement to about 75% or 80% chord; beyond that location, the discrepancies mentioned previously are clearly evident. The disagreement near the trailing edge on the pressure surface is most likely due to some unsteadiness in the flow solution there. The trailing edge geometry of the inlet guide vane is essentially an

asymmetric chisel, with the bevel of the chisel lying on the suction side of the blade and the point of the chisel being somewhat rounded off. As such, a small separation region exists in the bevel for the entire span of the blade. Depending on the behavior of the wall function and turbulence model in this region, the predictions may quite possibly give an improperly located rear stagnation point. The lack of a sharp trailing edge exacerbates this potential problem.

In the IGV wake region, Figure 4.8 shows the velocity distributions at twelve spanwise locations located 49.7% chord axially downstream of the IGV trailing edge. The figure compares the axial, radial, and tangential velocity components from the prediction with those measured using a rake of five-hole probes. In order to make this comparison, we needed to perform a three-dimensional interpolation of the numerical results, since the grid lines did not lie in axial planes. At 4.8% span and, to a lesser extent, at 9.5% span, the axial velocity comparison shows that the predicted wake depth and width are smaller than the measurements. Examination of the predicted flow field showed the corner separation on the suction surface to be smaller than the separation that was measured. In the predicted flow field, this difference manifested itself downstream as a shallower, narrower wake. Also, to conserve mass, the peak in the predicted axial velocity on the pressure side of the wake is greater than the measured peak.

At larger spanwise locations, Figure 4.8 shows that the numerical predictions of axial velocity give deeper wakes than the five-hole probe measurements. This result is surprising since the grid points at this axial location were more sparse than near the blade itself—which should yield larger numerical dissipation and a faster decay of the viscous wakes. From 19.0% span to 76.2% span, the axial velocity comparisons show another surprise: A peak in the predicted axial velocity occurs on the suction side of the wake—a peak that does not occur in the measurements. This peak appears outside of the viscous wake; and yet, this flow field location is too far downstream of these lightly-loaded inlet guide vanes to feel any potential flow effects. The deeper, predicted wakes continue until the 95.2% span location, where the contamination of the measured wakes from vortices emanating from axially-running seams between tunnel liner sections made comparisons difficult.

The circumferential variation of radial velocity in Figure 4.8 occurs because the spanwise variation in circulation on the inlet guide vanes gives rise to a trailing vortex sheet. Avoiding the comparisons at 4.8%, 90.5%, and 95.2% span where calibration problems produced offsets in the radial velocity measurements, we see that the numerical predictions compare very well with the five-hole probe measurements of the radial velocity variations. Since the trailing vortex sheet is radially skewed, the sheet also leads to a circumferential variation in tangential velocity. The swirl produced by the inlet guide vanes also means that a small portion of the viscous wake profile will have a component of tangential velocity. Figure 4.8 shows the resulting variation in tangential velocity. Despite the measured blade-to-blade differences, Figure 4.8 shows good comparisons between predicted and measured tangential velocities. Near the hub, the level of tangential velocity shows that the predictions give a little more swirl than what was measured.

The circumferential variations of radial and tangential velocity can also be shown as secondary velocity vectors. Figure 4.9 presents the flow within a plane normal to the axial direction with the local circumferential-mean velocity (found from area averaging) subtracted from both the predicted and measured velocities. The resulting secondary velocity vectors follow closely to those defined by Smith [1955]. Both the predictions and measurements show that the trailing vortex sheet has deformed and rolled-up into two concentrated vortex structures rotating in opposite

directions. The predicted locations of these two structures lies very close to the measured locations, although the measured vectors appear to be somewhat larger. These two vortex structures induce a swirling motion in the potential portion of the passage flow. Near the hub, the predicted location of this clockwise (looking upstream) motion matches the measured location; but near the casing, the predicted location of the counter-clockwise motion appears closer to the pressure side of the wake than the measured location.

At this same axial location within HIREP, Figure 4.10 presents predicted and measured contours of total-pressure coefficient. As with the secondary velocity vector plots, the predicted total-pressure contours are smoother than the measured plots since the numerical simulation contained more grid points than the experiment contained five-hole probe locations. Both the predictions and measurements showed a slightly radially-skewed wake with similar levels of total-pressure coefficient. Without the casing boundary layer used in the simulation inflow, the predictions do not show the correct total-pressure loss near the casing endwall. This effect is even more evident after performing a circumferential average, as shown in Figure 4.11. This figure shows higher levels of predicted total-pressure coefficient near the casing endwall, but lower predicted levels elsewhere. The loss in total-pressure coefficient through most of the span (from an inlet value of unity) should be minimal through these lightly-loaded vanes. Note that the measurements using the rake of five-hole probes shows that the values of total-pressure coefficient remain close to unity, while the measurements using the five-hole probe radial surveys actually show values greater than unity. Zierke, Straka, and Taylor [1993] explain that the experimental uncertainty is much greater for the radial surveys than for the rake surveys. Figure 4.11 also shows a larger predicted gradient in the static-pressure profile than shown in the measurements of static pressure—a quantity difficult to measure away from solid surfaces.

Finally, Figure 4.12 shows comparisons of predicted and measured values of the circumferentially-averaged velocity components. Overall, these comparisons are quite good. However, Figure 4.12 clearly shows the absence of the correct inflow boundary layer on the casing endwall during the numerical simulation. Consequently, in order to preserve the same mass flow, the numerical simulation results in smaller values of circumferentially-averaged axial velocities away from the endwalls.

4.4.2 Rotor Blades

Recall that the solution procedure used in the numerical simulation of HIREP consisted of a series of "flips" through which the three-dimensional solution of the IGV passage "communicated" with the three-dimensional solution of the rotor blade passage. This "communication" occurred on a two-dimensional grid that contained updated axisymmetric body forces and correlations from the latest "flip" from one blade row solution to the other. Through this procedure, the momentum and vorticity field from the IGV flow field solution described in the previous section is correctly transferred to the rotor blade flow field solution. And even though the momentum and vorticity field from the IGV flow field appears "smeared" to the rotor blades, the transfer of momentum and vorticity that does take place should adequately model the effect of the inlet guide vanes on the time-average flow through the rotor blades. The procedure also adequately models the potential flow effect of the rotor blades on the time-average flow through the inlet guide vanes.

Similar to our comparisons for the IGV flow field, we will initially compare the predicted and measured rotor blade static-pressure distributions. Figure 4.13 shows that these comparisons for the rotor blades are even better than the comparisons for the inlet guide vanes in Figure 4.5--the rotor blade flow field showed less unsteadiness in the predictions near the trailing edge than did the IGV flow field. Again using the pressure coefficient, K_p , Figure 4.13 shows that both the blade loading and the local streamwise pressure gradients are well predicted at all spanwise locations. The contour plots of Figures 4.14 and 4.15 also show very good agreement, especially when only comparing the predicted static-pressure contours within the regions where the measured contours are bounded by the locations of the pressure taps. The suction surface static pressures of Figure 4.14 show an adverse pressure gradient over the last half of the blade, with the predictions showing some three-dimensional effects in the corner region where the trailing edge meets the hub endwall--a region where no pressure taps existed. Figure 4.15 shows that the predictions also give some three-dimensional effects where the pressure surface trailing edge meets the hub endwall.

Numerically integrating the predicted three-dimensional static-pressure distribution allows us to calculate net thrust and torque coefficients. Figure 4.16 shows these calculations compared to the measured and design values. At the design volumetric flow coefficient, the predicted torque coefficient matches both the measured and design values very well, with the predicted value being about 0.7% higher than the design value. (The measured torque coefficient was 2% lower than the design value.) Comparisons of the thrust coefficient show that the predicted value is 8.5% higher than the design value. While the actual thrust coefficient is probably higher than the design value, the actual coefficient is most likely less than the measured value (which was 16% higher than the design value). Zierke, Straka, and Taylor [1993] describe the difficulties that they had in performing this measurement--difficulties that led to greater measurement uncertainties. Therefore, the simulation appears to give very reasonable predictions of rotor thrust since the predicted value in Figure 4.16 lies between the measured and design values.

The significance of these types of numerical simulations lies in the ability to give three-dimensional, viscous flow information to the designer. One very prominent characteristic of this flow field prediction is the existence and location of regions of boundary layer separation. The next series of figures shows how well this numerical simulation predicts two types of three-dimensional separation.

First, Figure 4.17 presents the predicted particle paths near the rotor hub endwall. Restricted to one grid point away from the hub, these particle paths follow the relative flow through the rotor blade passage and can be used to simulate limiting streamlines. These limiting streamlines can be compared to the skin-friction lines found experimentally using an oil-paint technique and shown schematically in Figure 4.18. Recall that limiting streamlines and skin-friction lines are indistinguishable, except for some differences that occur in the vicinity of lines of separation. Both Figure 4.17 and Figure 4.18 show one type of three-dimensional separation. Just upstream of the rotor blade leading edge, the hub endwall boundary layer separates at a saddle point, with a separation line passing through the saddle point and forming a C-pattern around the blade. Although it is difficult to identify the exact location of the predicted saddle point from Figure 4.17, it appears that the predicted saddle point is a little closer to the leading edge than the measured saddle point in Figure 4.18. The presence of the fillet (and possibly a thicker boundary layer) in the actual flow field will cause the saddle point to lie further upstream of the predicted location. Nevertheless, the numerical simulation does show the existence of the saddle point, as well as the measured movement of the pressure side leg of the separation line into the midpassage

region and the measured movement of the suction side leg of the separation line up onto the suction surface as a result of some local flow overturning. The prediction of this type of three-dimensional separation is important since it corresponds to the development of horseshoe vortices.

The measurements of Figure 4.18 also shows the existence of a saddle point near the suction surface trailing edge, as well as a corresponding line of secondary separation. Clearly, the predicted particle paths in Figure 4.17 also show this secondary separation line and the probable existence of the saddle point. As described by Zierke, Straka, and Taylor [1993], this secondary separation is related to the three-dimensional corner separation that occurs where the suction surface trailing edge meets the hub endwall. Figure 4.19 shows the predicted particle paths of this corner separation on the suction surface, while Figure 4.20 shows a schematic of the skin-friction lines found from the oil-paint technique. The predicted and measured patterns associated with this corner separation look remarkably similar, although the predictions do not show the existence of the spiral node as clearly as the measurements. Both the predictions and the measurements also show a large amount of outward radial migration of the flow. However, the measurements do show that the separation line that extends out to the blade tip lies further upstream of the trailing edge than predicted by the numerical simulation.

Next, we shall compare the predictions with the measurements acquired on an axial plane 32.2% chord axially downstream of the rotor tip trailing edge. As with the flow downstream of the inlet guide vanes, we needed to perform a three-dimensional interpolation of the numerical results, since the grid lines did not lie in axial planes. The predicted and measured axial velocity contours of Figure 4.21 both show the existence of the skewed rotor blade wakes. The contour levels within these wakes are quite similar, with the nonuniform nature of the measured wakes arising from computing contours using LDV data from coarsely-spaced, discrete measurement locations. As a matter of fact, all of the predicted and measured contours compare well in this plane, except for one very important region: the region near the rotor tip leakage vortex. The measured tip leakage vortex appears further from the casing endwall than the predicted vortex, with the potential flow effects from the measured vortex extending much further into the flow field. Comparisons of the predicted and measured tangential velocity contours in Figure 4.22 quantitatively give the same conclusions as the comparisons of the axial velocities.

Similar to the numerical results downstream of the inlet guide vanes, we can plot the velocities downstream of the rotor blades using secondary velocity vectors, with the local circumferential-mean velocity (found from area averaging) subtracted from the predicted velocities. Figure 4.23 presents this vector plot. No comparisons can be made of these predicted vectors with measured vectors since Zierke, Straka, and Taylor [1973] could not measure radial velocities with their two-component LDV system. Similar to the IGV trailing vortex sheet, the rotor blade trailing vortex sheet has deformed and rolled-up into two concentrated vortex structures rotating in opposite directions. While much of the swirling motion between vortex sheets has been induced by the sheets themselves, one can clearly observe the existence of the rotor tip leakage vortex, which again lies very close to the casing endwall.

To more closely examine the position of the tip leakage vortex, we interpolated the numerical results at several axial planes downstream of the rotor tip trailing edge. In order to identify the location of the vortex core, we plotted contours of static pressure on these interpolated planes, with the clearly marked position of the minimum static pressure giving the location of the core. To summarize, Figure 4.24 shows the spanwise location of the vortex core compared to

measured values found from both LDV data and laser light sheet visualization. This figure shows that the predicted core lies 2-3% span closer to the casing endwall, with the radial locations for both the predicted and measured cores changing very little downstream of the trailing edge.

Since the predictions did not include an inlet boundary layer, the numerical simulation computed a smaller casing endwall boundary layer upstream of the rotor blades than shown experimentally (see Figure 4.12). If the numerical simulation had computed a thicker boundary layer, the incidence angle at the rotor blade tip would have been larger and, subsequently, the strength of the rotor tip leakage vortex would increase. Using the image vortex system that Chen, Greitzer, Tan, and Marble [1991] used within a rotor blade passage, a stronger vortex will change the strength of the image vortices. Finally, the stronger image vortices should induce a motion on the tip leakage vortex that would cause the position of the tip leakage vortex to move further away from the casing endwall (and slightly further away from the rotor blade suction surface). Later, we recomputed the HIREP flow field using the measured inflow. Unfortunately, the revised numerical simulation did not predict a significant movement of the tip leakage vortex away from the casing endwall and, thus, the position of the vortex still disagreed with the measured position.

Despite the discrepancies between the spanwise positions of the tip leakage vortex, Figure 4.25 shows that the positions of the predicted and measured vortex core agree very well in the blade-to-blade plane. To better visualize the tip leakage vortex in the numerical simulation, we observed the paths of particles that were released at the edge of the clearance region and rolled-up into a vortex. Observation of the paths of particles released near the trailing-edge tip reveals another interesting phenomenon. These trailing-edge particle paths seem to roll-up into an independent vortex, that rotates with the same sense as the tip leakage vortex, but originates closer to the casing endwall. Zierke, Straka, and Taylor [1993] identified this second vortex as a trailing-edge separation vortex, that originates when the blade boundary layer separates near the trailing edge in the presence of radial outward flow. In a very similar experiment, Farrell [1989] was able to lower his tunnel pressure to a low enough level for cavitation to occur in both vortices. Figure 4.27 shows his photograph of this phenomenon—an observation very similar to the predicted particle paths of Figure 4.26. Further, cavitation visualization performed by Farrell [1989] showed that these two vortices will eventually roll-up into a single vortex as they propagate downstream (as also indicated by the predictions in Figure 4.2b).

For a more detailed comparison between the numerical simulation and the experiment, Figure 4.28 presents 15 spanwise plots of the circumferential variations of axial and tangential velocity at the axial plane 32.2% chord axially downstream of the rotor tip trailing edge. At 2.9% span, the predictions match the LDV data fairly well, although the experiment indicates a flow structure on either side of the wake (possibly the horseshoe vortex) that is not predicted. At larger spanwise locations, through 57.7% span, the predictions agree fairly well with the LDV data, although a few differences are worth noting. At all these spanwise locations, the predicted viscous wakes are deeper than the measured wakes. Also, by observing the centers of the wakes, the predicted wakes appear to be slightly more skewed than the measured wakes. Finally, from 29.4% span to 57.7% span, the overall level of tangential velocity is more negative for the predictions, indicating the numerical simulation allows for more flow turning than the experiment.

Closer to the casing endwall, Figure 4.28 shows poorer agreement between the predictions and the measurements. First, as clearly shown from 81.3% span to 90.7% span, the predicted wakes are shallower than the measured wakes—the opposite trend from what we observed at

smaller spanwise locations. During the HIREP experiment, Zierke, Straka, and Taylor [1993] acquired LDV data at 76.2% span and at several axial locations, in order to investigate wake decay. Figure 4.29 presents comparisons of the predicted wakes with these LDV data. All the measured wakes are narrower than the predicted wakes. However, the measured wakes are deeper at 2.5% chord downstream of the trailing edge and reach a similar depth at 16.5% chord downstream--indicating a faster decay rate for the experimental wakes. Recall that in the numerical simulation, the eddy viscosity downstream of the blades is extrapolated along axial grid lines. If the axial grid lines do not reasonably follow the wake, then the predicted eddy viscosity in the wake will be too small. Therefore, close to the trailing edge, one might expect reasonable agreement. However, as the predicted wake moves downstream and strays from the region where the eddy viscosity exists, one might expect the wake depth to decay more like a laminar wake rather than a turbulent wake.

Outside of the viscous wakes, in an essentially potential flow core, Figure 4.29 shows significant differences between the predictions and the measurements. Figure 4.28 shows these same differences from 67.1% span to 86.0% span, the measured axial velocities show a greater hump, while the measured tangential velocities show a greater trough. These flow structures result from potential flow effects caused by the rotor tip leakage vortex and, since the predicted vortex lies closer to the casing endwall, the potential flow effect from the predicted vortex will not extend as far inboard. From 90.7% span to 99.2% span, the discrepancies in the radial position of the tip leakage vortex core becomes even more apparent.

The incorrect predicted radial position of the tip leakage vortex also impacts the circumferentially-averaged velocity profiles in Figure 4.30. Near the casing endwall, the deficit in axial velocity results more from circumferentially averaging through the axial velocity deficits in the tip leakage vortex than from the endwall boundary layer. With the predicted vortex positioned nearer to the casing endwall, Figure 4.30 shows that the axial velocity deficit lies closer to the casing for the predictions than for the measurements. This predicted deficit displaces less fluid away from the casing endwall and results in a smaller axial velocity through most of the span in order to have the same mass flow. Zierke, Straka, and Taylor [1993] point out that their experimental results do not average through any IGV wakes, and this also increases the circumferentially-averaged measurements relative to the predictions. The tangential velocity profile compares fairly well near the endwalls; but again, the predictions exhibit more negative tangential velocity through most of the span. The inlet guide vanes in HIREP were designed to place positive tangential velocity into the flow and the rotor blades were designed to take all of the swirl out of the flow at the blade tip and leave some negative tangential velocity in the flow at the blade root. Finally, the predictions agree with the HIREP design in that the predicted level of circumferentially-averaged radial velocity is zero for the entire span.

Figure 4.31 shows the circumferentially-averaged predictions of the static- and total-pressure coefficients. The numerical simulation predicts a constant static pressure over the entire span, with the static pressures near the casing endwall predicted to be somewhat smaller than the pressure tap measurements. Figure 4.31 also compares the predicted total pressures with those measured with radial Kiel probe surveys at two circumferential positions of the inlet guide vanes. If these experimental surveys would have been acquired for many IGV positions and then circumferentially averaged, these averaged values of total-pressure coefficient would probably agree quite well with the predicted values. Before we performed the circumferential averaging, the total-pressure coefficients varied as they appear in the contour plot of Figure 4.32. The higher regions

of loss appear as low regions of total pressure in the rotor blade wakes and near the endwalls. Figure 4.32 agrees qualitatively with that data the Zierke, Straka, and Taylor [1993] measured with a fast-response total-pressure probe. However, these measurements could only measure total-pressure variations and also included an IGV wake and, therefore, we could not make a direct comparison with the predictions.

5. Summary and Conclusions

A system of equations is presented governing the average-passage flow through a multiple-blade-row turbomachine operating in the incompressible flow regime. The governing equations result from the sequential application of three averaging operators to the incompressible, Navier-Stokes equations. A procedure for closing this averaged system of equations is also described. To facilitate numerical treatment, the governing equations are cast in a preconditioned, pseudo-unsteady form. It is important that the averaging operators be carried out before casting the equations in the pseudo-unsteady form. The inclusion of the preconditioning matrix allows for better control of the solution transient.

An explicit numerical treatment is outlined to approximate solutions to the governing equations. Basically, this procedure follows the fairly standard four-stage Runge-Kutta time-stepping scheme applied to a cell-centered finite-volume discretization for hexahedral cells. Several convergence acceleration techniques—including local time stepping, implicit residual smoothing, and multigrid—are applied to this scheme in order to improve its efficiency. Also, boundary conditions appropriate for an average-passage simulation are presented. Finally, the practical aspects of numerically closing the discretized governing equations are discussed. Specifically, a two-tier iteration procedure is described, where the inner iterations update the three-dimensional solutions for each blade row and the outer iterations update the average-passage source for each blade row.

An experimental investigation is briefly described involving detailed measurements made of the incompressible flow field in a high Reynolds number pump. This 42-inch diameter pump includes two blade rows that operate within a 48-inch diameter water tunnel. A numerical simulation using the incompressible, average-passage equations was performed in order to compare with these flow field measurements.

Comparisons between the computed and measured static pressures on the inlet guide vanes show reasonable predictions of blade loading. However, some discrepancies occur in the pressure distributions near the trailing edge at midspan. The IGV wake velocity profiles also show reasonable comparisons near the endwalls, with the largest discrepancies (especially in axial velocity) occurring near midspan. Residual unsteadiness in the numerical solutions probably account for the discrepancies in the pressure and velocity flow fields near the IGV trailing edge at midspan. This unsteadiness is most likely due to the combination of the bluntness of the IGV trailing edge and the poor performance of the Baldwin-Lomax eddy viscosity model in the wake regions (at least for this grid). Comparison of the total-pressure contours and the circumferentially-averaged pressures and velocities show good agreement away from the casing endwall, where the calculation lacked the proper inflow boundary layer.

Comparisons of the computed and measured rotor blade static-pressure distribution show excellent agreement at all radial locations. As such, the integrated effect of the computed rotor blade pressures gave good agreement with the measured torque and thrust. Computed particle pathlines on the rotor hub and suction surfaces qualitatively captured the essential separation features showed by the experimental skin-friction lines. Inadequate grid resolution probably led to any discrepancies in these comparisons. Comparisons of the contours of the axial and tangential velocities downstream of the rotor blades show qualitative agreement away from the casing

endwall. Near the casing, the lack of the correct inflow boundary layer had some detrimental effect. However, even this improper inflow boundary condition cannot completely explain why the calculated tip leakage vortex lies closer to the casing than the measured vortex. Despite this discrepancy in the radial location of the tip leakage vortex, the blade-to-blade trajectory appears to agree quite well with the measurements. The computations also appear to capture the essential character of the measured leakage flow; that is, a primary vortex exists, as well as a weaker trailing-edge separation vortex.

Downstream of the rotor blades, comparisons of wake velocity profiles show qualitative agreement away from the endwalls. Very close to the hub, inadequate grid resolution and the subsequent lack of a well-defined horseshoe vortex in the calculation are probably the culprits. Beyond about 70% span, the discrepancy in the radial location of the tip leakage vortex causes differences in the computed and measured velocity profiles. At 76.2% span, the measured wakes decay more rapidly than the predicted wakes. This is most certainly a manifestation of the current implementation of the Baldwin-Lomax model in the wake region. Finally, as with the IGV flow field, comparisons of the total-pressure contours and the circumferentially-averaged pressures and velocities downstream of the rotor blades show good agreement away from the casing endwall, where the calculation lacked the proper inflow boundary layer.

The comparisons in this investigation represent an initial validation case of the numerical algorithm for the simulation of incompressible flow within a multiple-blade-row turbomachine, as outlined previously. For the most part, the comparisons indicate that the model does an adequate job of predicting many of the essential flow features present in a multiple-blade-row environment. For example, blade pressure distributions are predicted quite well—as well as the overall performance, as indicated by circumferentially-averaged quantities and rotor blade torque and thrust. Also, certain highly three-dimensional effects like leakage vortices and corner separations can be qualitatively predicted. On the other hand, it appears as though the behavior of the turbulence model in wake regions consistently causes problems in predicting wake velocity profiles (at least for this grid). Therefore, the most pressing need for the numerical simulation of the incompressible, average-passage flow through a multiple-blade-row turbomachine appears to be a turbulence model that better represents the physics in wake regions.

Bibliography

- Adamczyk, J. J., "A Model Equation for Simulating Flows in Multistage Turbomachinery," ASME Paper 85-GT-226, 1984.
- Adamczyk, J. J., Mulac, R. A., and Celestina, M. L., "A Model for Closing the Inviscid Form of the Average-Passage Equation System," Transactions of the ASME, *Journal of Turbomachinery*, Vol. 108, pp. 180-186, October 1986.
- Adamczyk, J. J., Celestina, M. L., Beach, T. A., and Barnett, M., "Simulation of 3-D Viscous Flow Within a Multi-Stage Turbine," ASME Paper 89-GT-152, 1989.
- Adamczyk, J. J., Extrapolation Procedure for a Eddy Viscosity in a Wake, Private Communication, 1992.
- Baldwin, B. S. and Lomax, H., "Thin Layer Approximation and Algebraic Model for Separated Turbulent Flow," AIAA Paper 78-257, 1978.
- Beach, T. A., "An Interactive Grid Generation Procedure for Axial and Radial Flow Turbomachinery," AIAA Paper 90-0344, 1990.
- Beach, T. A. and Hoffman, G. H., "IGB Grid: User's Manual (A Turbomachinery Grid Generation Code)," NASA CR-189104, 1992.
- Chen, G. T., Greitzer, E. M., Tan, C. S., and Marble, F. E., "Similarity Analysis of Compressor Tip Clearance Flow Structure," Transactions of the ASME, *Journal of Turbomachinery*, Vol. 113, pp. 260-271, April 1991.
- Chorin, A. J., "A Numerical Method for Solving Incompressible Viscous Flow Problems," *Journal of Computational Physics*, Vol. 2, pp. 12-26, 1967.
- Farrell, K. J., "An Investigation of End-Wall Vortex Cavitation in a High Reynolds Number Axial-Flow Pump," M.S. Thesis, Department of Mechanical Engineering, The Pennsylvania State University, May 1989.
- Jameson, A., Schmidt, W., and Turkel, E., "Numerical Solutions of the Euler Equations by Finite Volume Methods Using Runge-Kutta Time-Stepping Schemes," AIAA Paper 81-1259, 1981.
- Jameson, A., "Numerical Solutions of the Euler Equations for Compressible Inviscid Flows," Princeton University, MAE Report 1643, 1983.
- Jameson, A. and Baker, T. J., "Multigrid Solution of the Euler Equations for Aircraft Configurations," AIAA Paper 84-0093, 1984.
- Kirtley, K. R., Beach, T. A., and Adamczyk, J. J., "Numerical Analysis of Secondary Flow in a Two-Stage Turbine," AIAA Paper 90-2356, 1990.

Bibliography (Cont.)

- Kunz, R. F. and Lakshminarayana, B., "Stability of Explicit Navier-Stokes Procedures Using $k-\epsilon$ and $k-\epsilon$ /Algebraic Reynolds Stress Turbulence Models," *Journal of Computational Physics*, Vol. 103, pp. 141-159, 1992.
- Martinelli, L., "Calculations of Viscous Flows with a Multigrid Method," Ph.D. Dissertation, Princeton University, 1987.
- Rizzi, A. and Eriksson, L., "Computation of Inviscid Incompressible Flow with Rotation," *Journal of Fluid Mechanics*, Vol. 153, pp. 275-312, 1985.
- Smith, L. H., Jr., "Secondary Flow in Axial-Flow Turbomachinery," *Transactions of the ASME*, Vol. 77, pp. 1065-1076, October 1955.
- Turkel, E., "Preconditioned Methods for Solving the Incompressible and Low Speed Compressible Equations," ICASE Report 86-14, 1986.
- Zierke, W. C., Straka, W. A., and Taylor, P. D., "The High Reynolds Number Flow Through an Axial-Flow Pump," ARL Penn State Internal Memorandum IM 93-012, Applied Research Laboratory, The Pennsylvania State University, March 1, 1993.

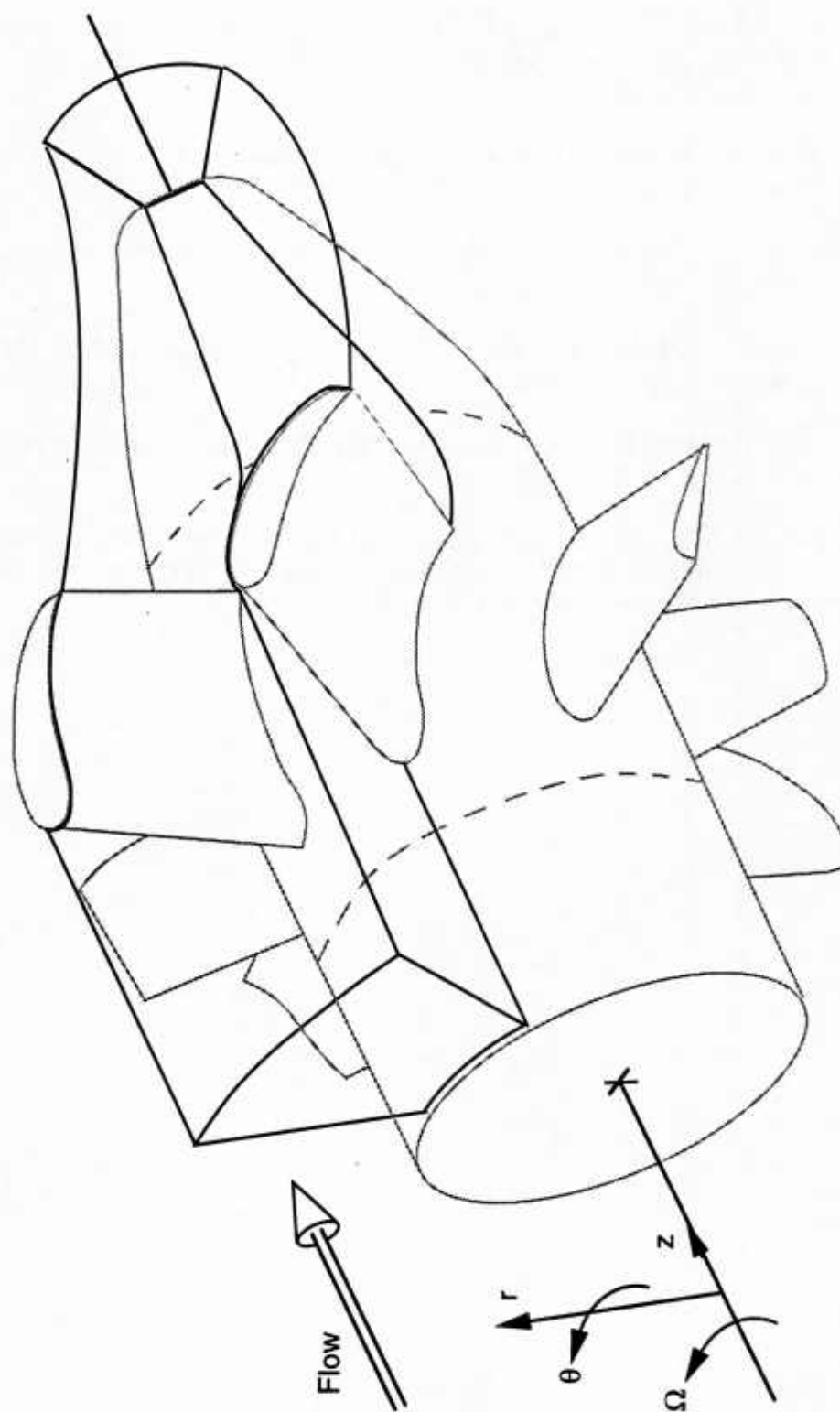


Figure 3.1 Generic Flow Domain with the Relevant Coordinate System

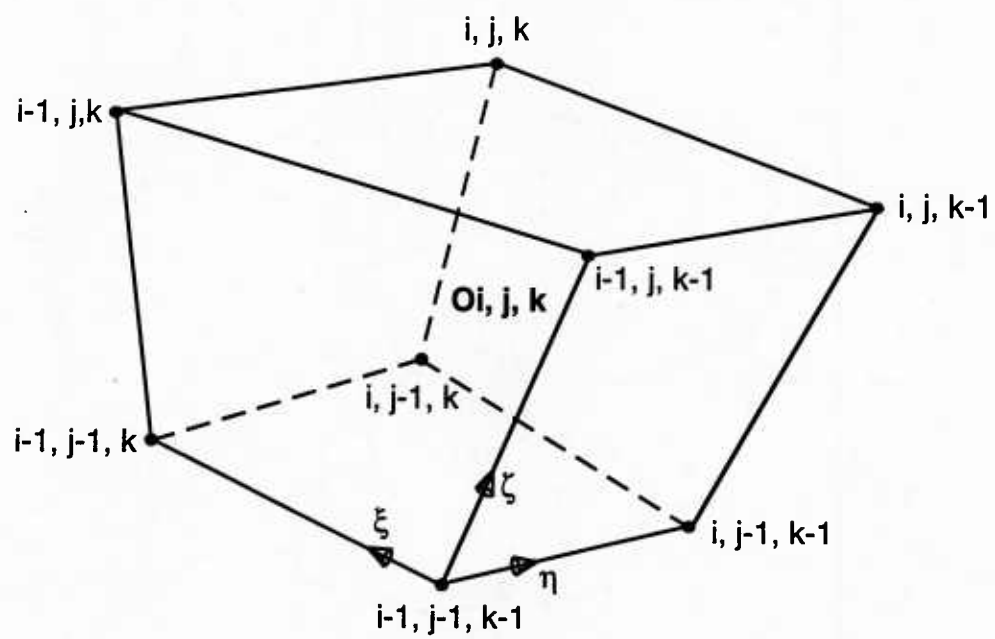


Figure 3.2 Generic Finite-Volume Cell

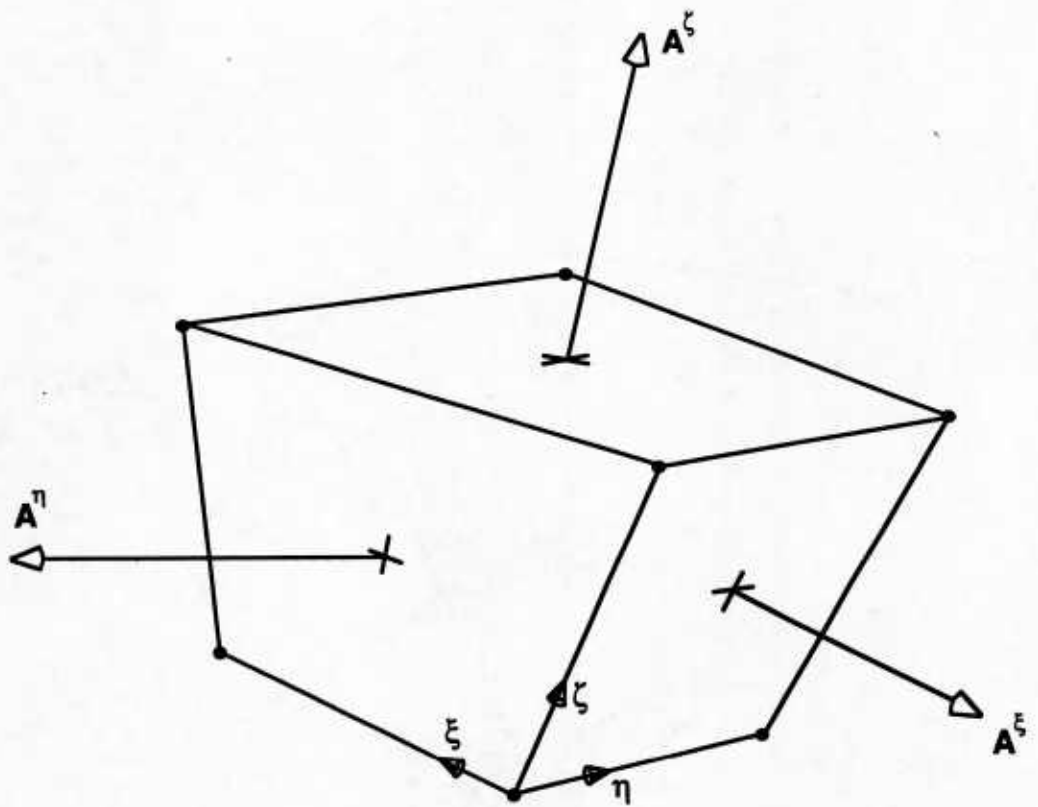


Figure 3.3 **Directed Areas from a Generic Finite-Volume Cell**

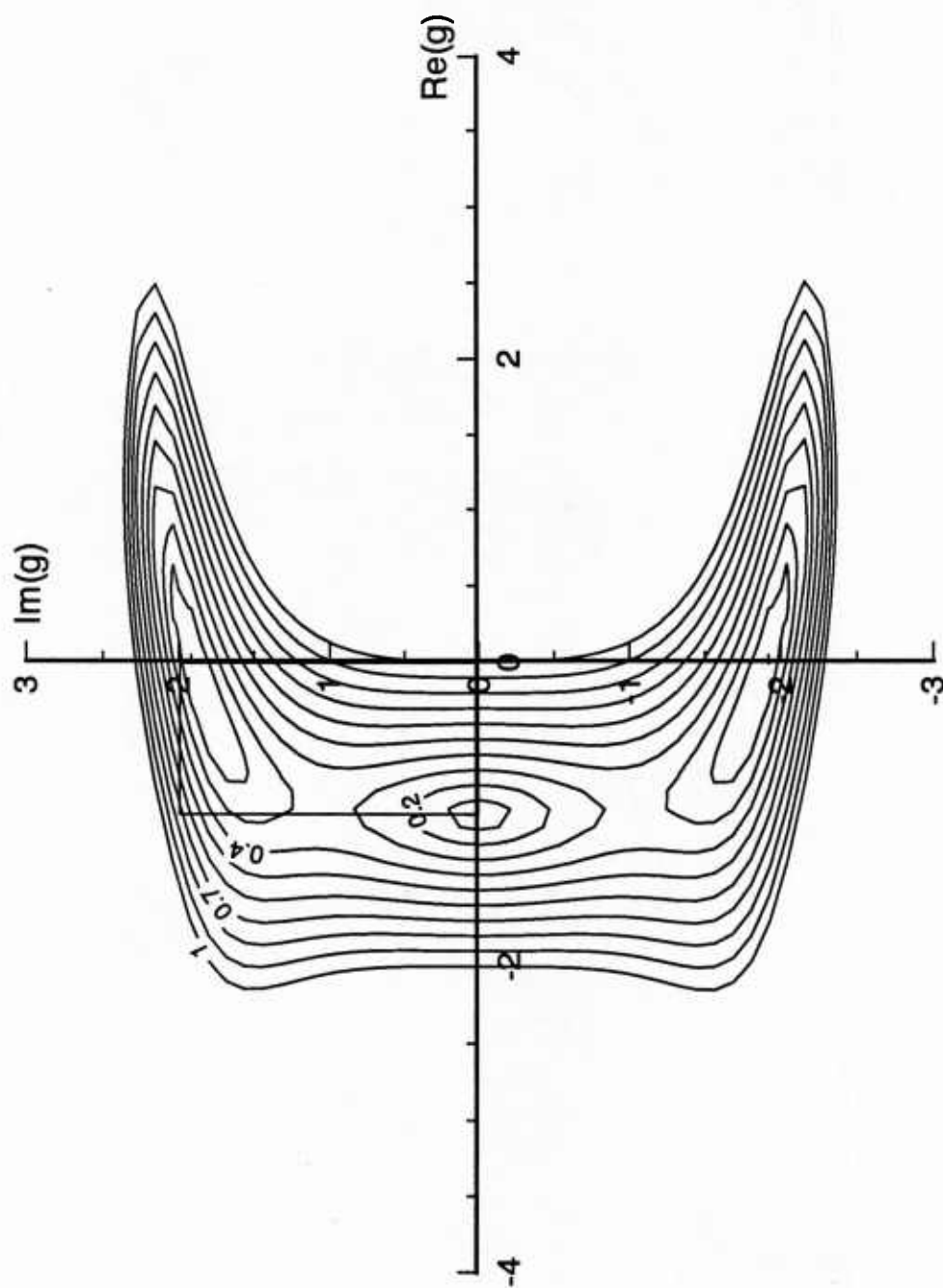


Figure 3.4 Neutral Stability Boundaries

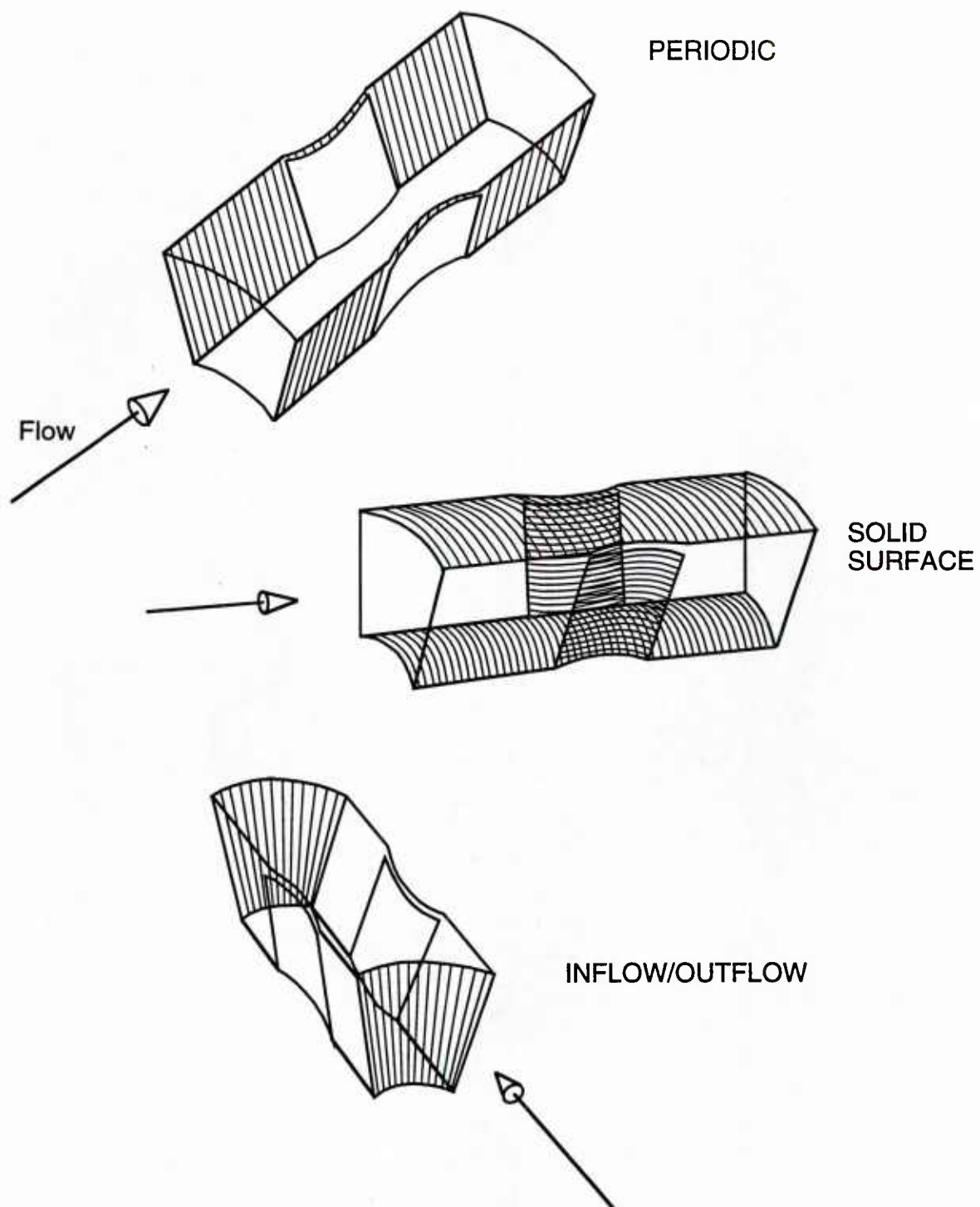
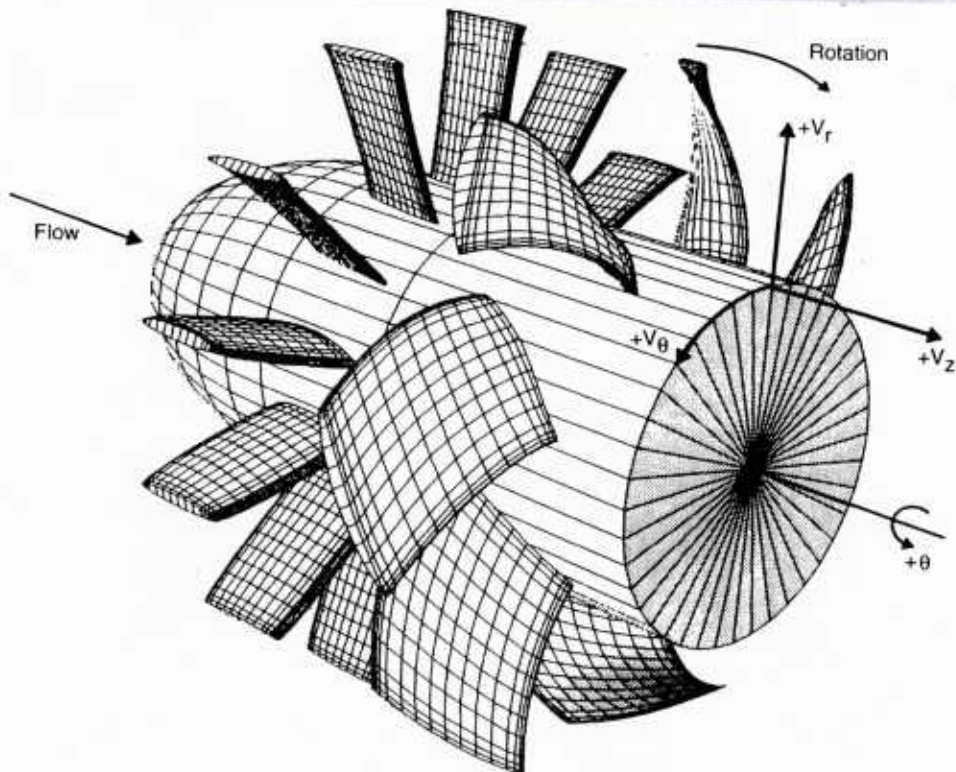
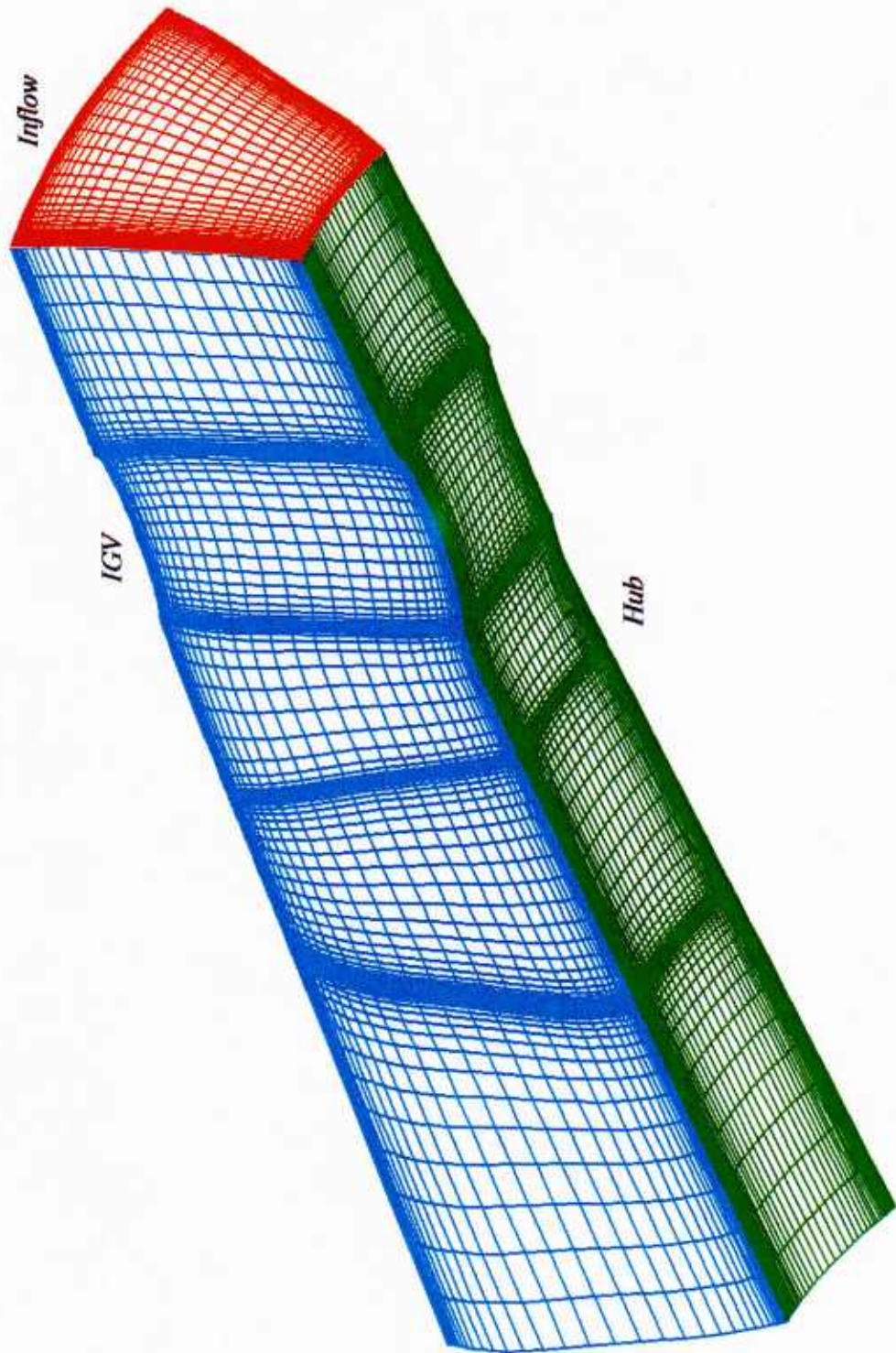


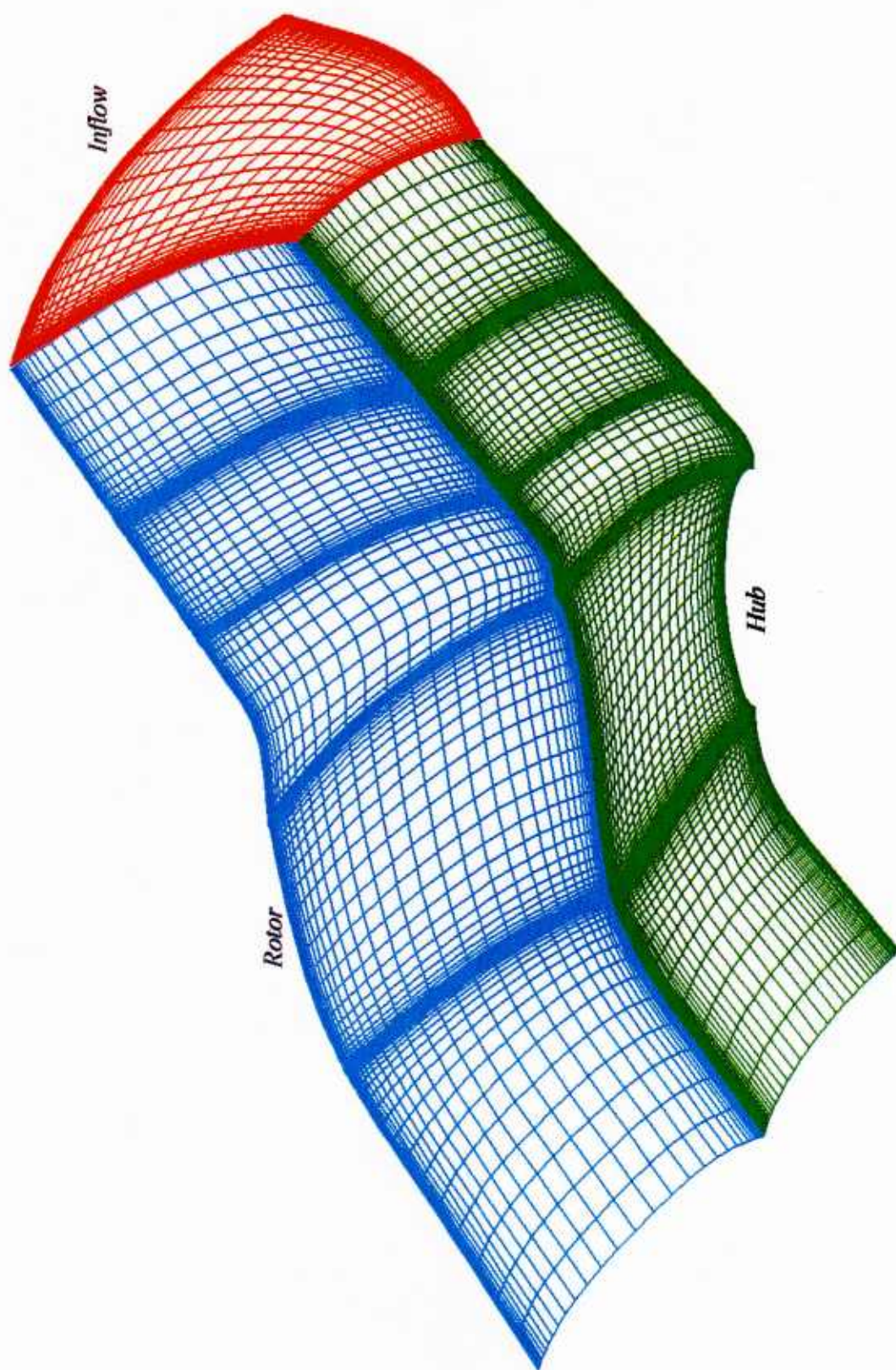
Figure 3.5 Types and Locations of Boundary Conditions for a Typical Blade Passage



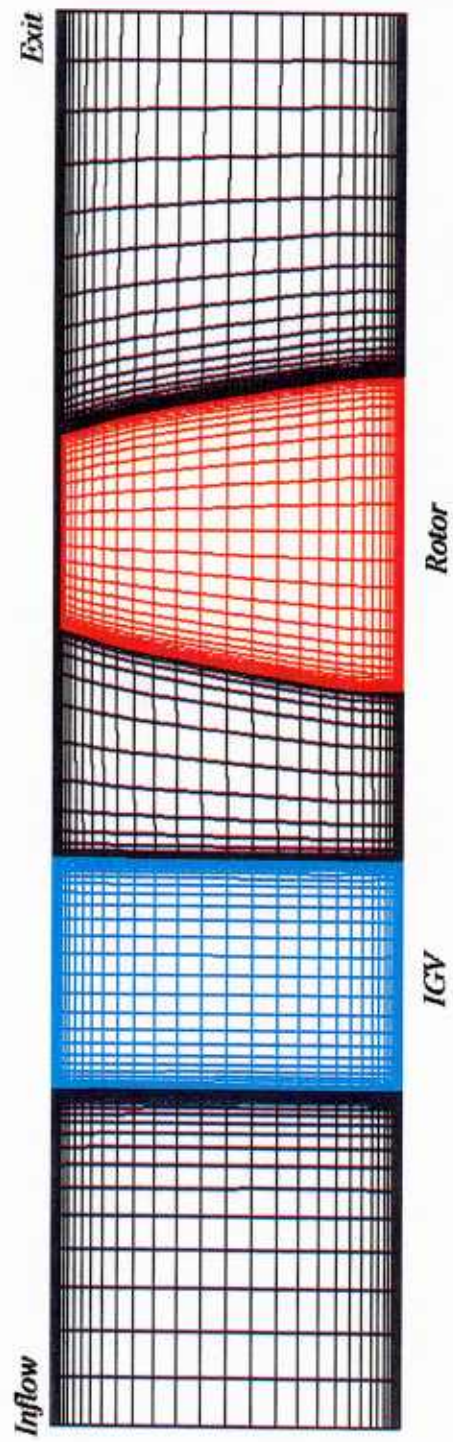
4.1 Isometric View of the HIREP Blades with the Cylindrical Coordinate System



4.2 Slices of the IGV Three-Dimensional, Computational Grid



4.3 Slices of the Rotor Blade Three-Dimensional, Computational Grid



4.4 Two-Dimensional Computational Grid Defining the Meridional Domain of HIREP

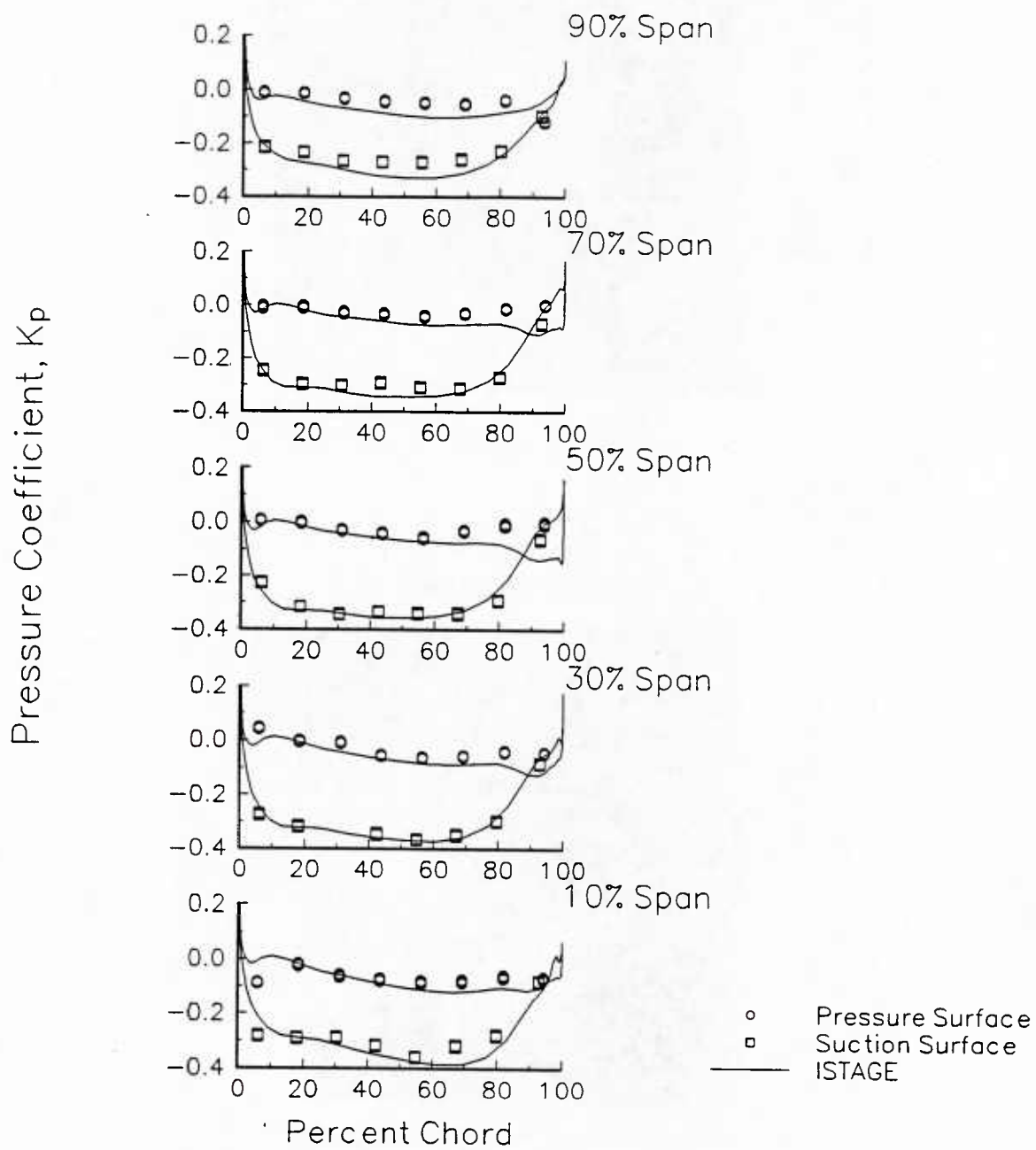


Figure 4.5 IGV Static-Pressure Distribution

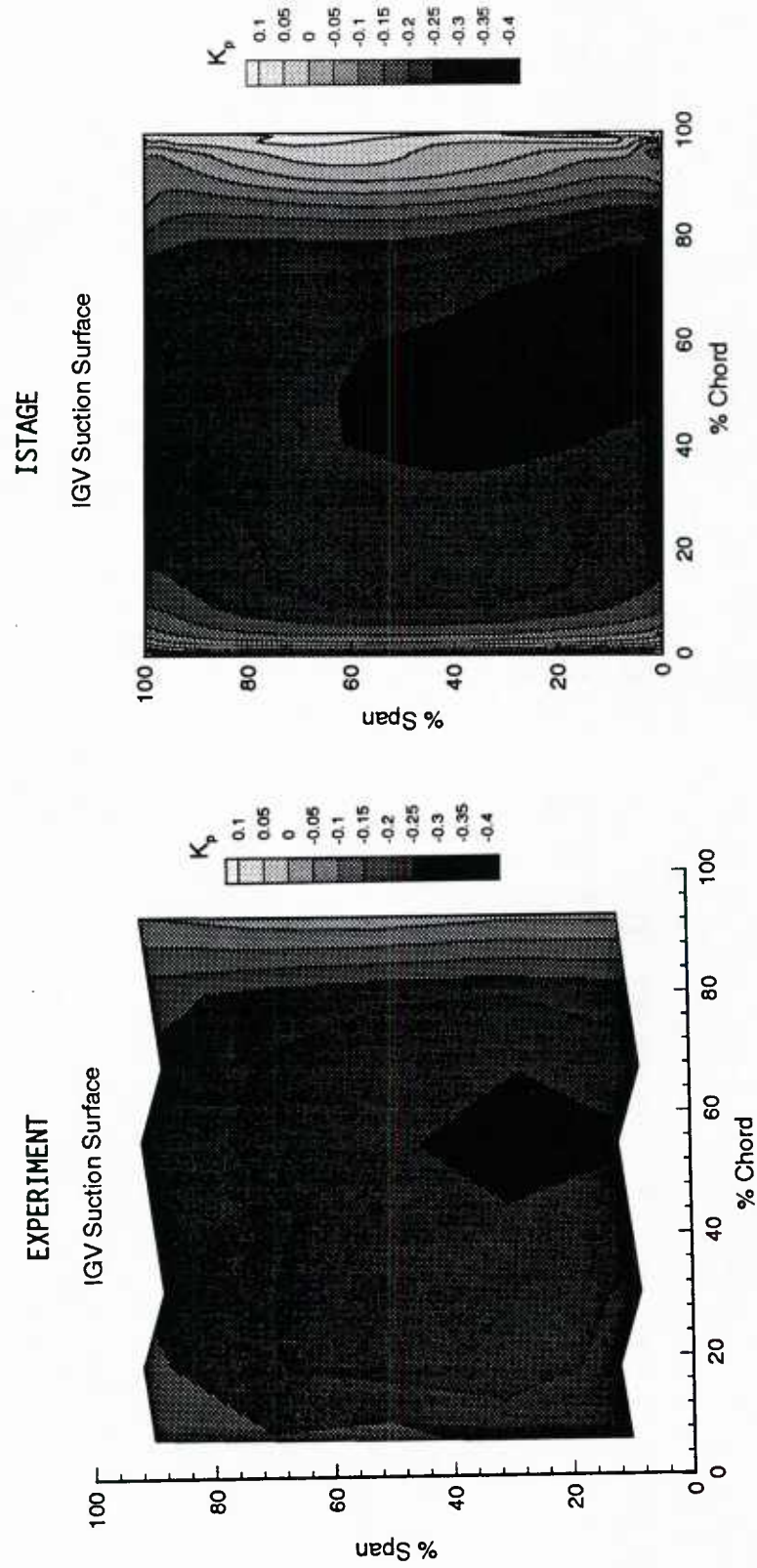


Figure 4.6 IGV Suction Surface Static-Pressure Contours

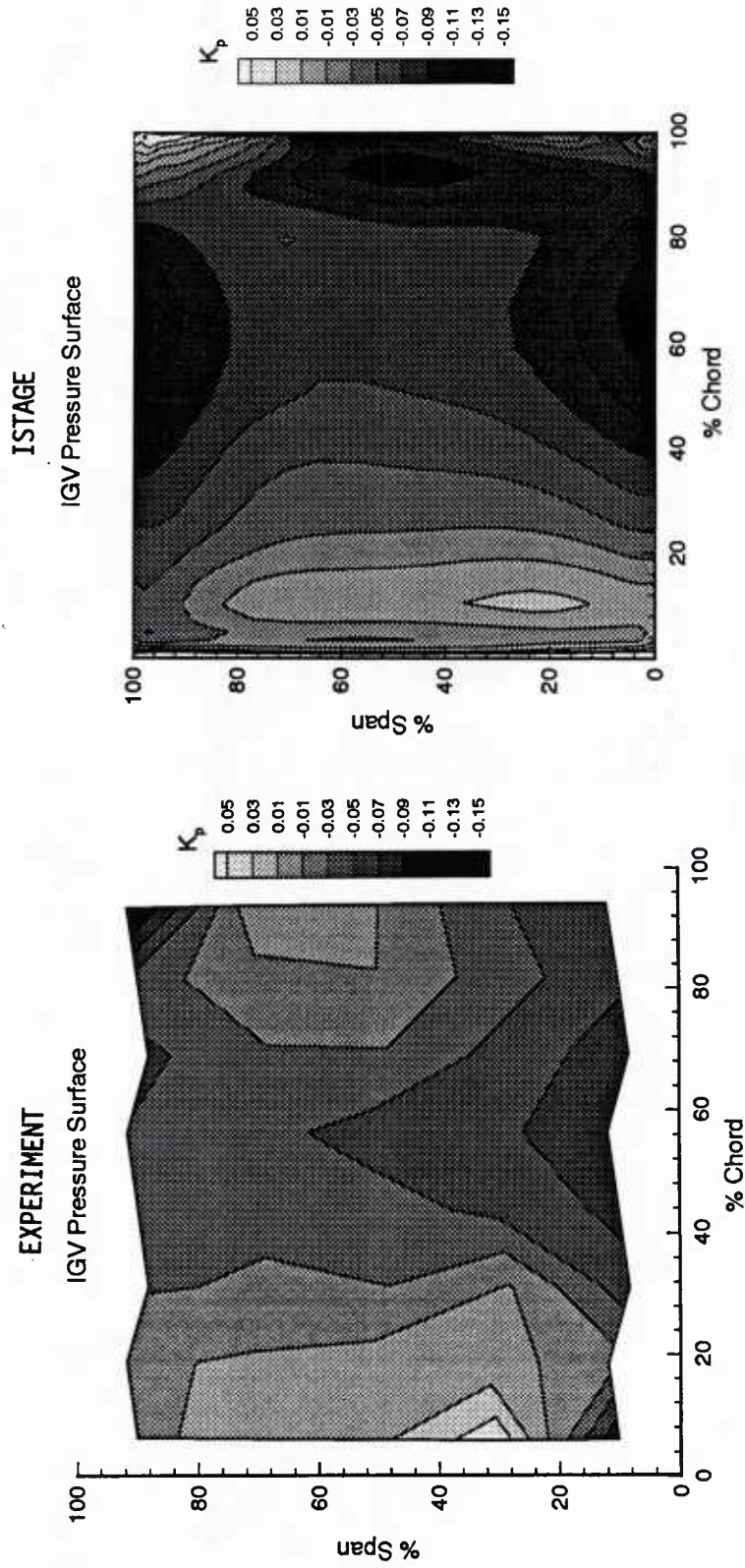


Figure 4.7 IGV Pressure Surface Static-Pressure Contours

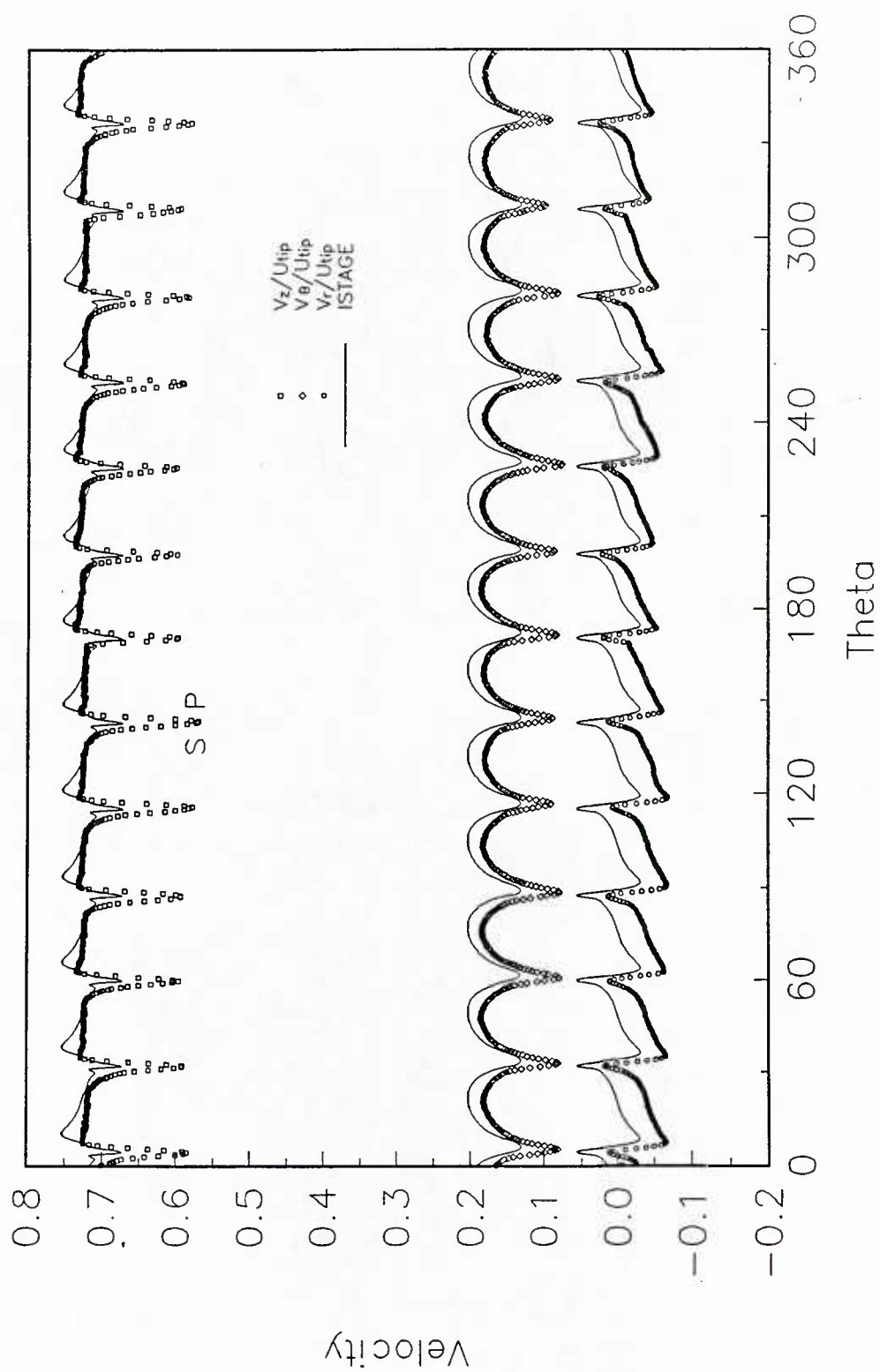


Figure 4.8 Circumferential Variation of Velocity Components 49.7% Chord Axially Downstream of the IGV Trailing Edge--Five-Hole Probe Measurements and ISTAGE Predictions: (a) 4.8% Span

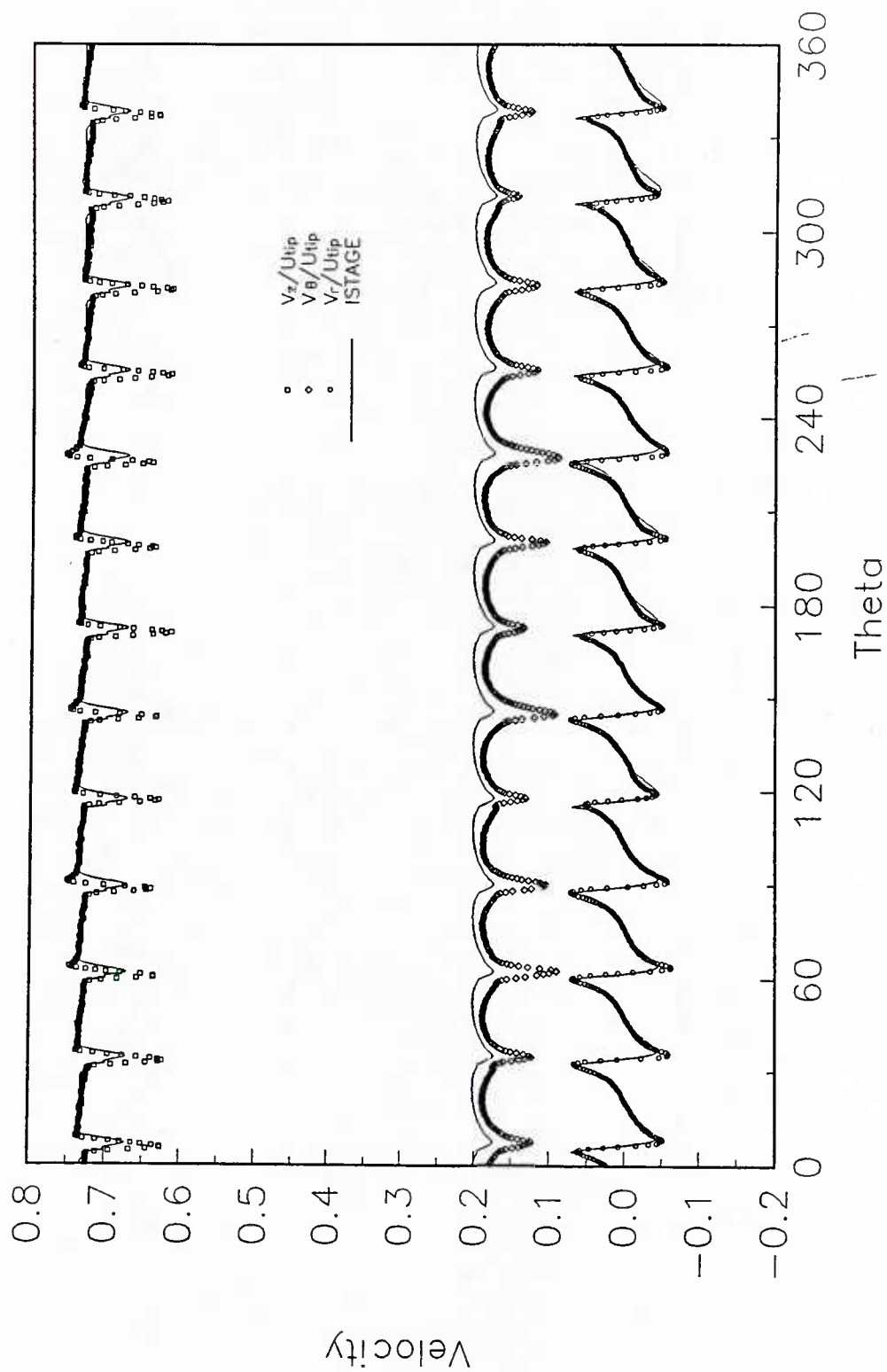


Figure 4.8 Circumferential Variation of Velocity Components 49.7% Chord Axially Downstream of the IGV Trailing Edge--Five-Hole Probe Measurements and ISTAGE Predictions: (b) 9.5% Span

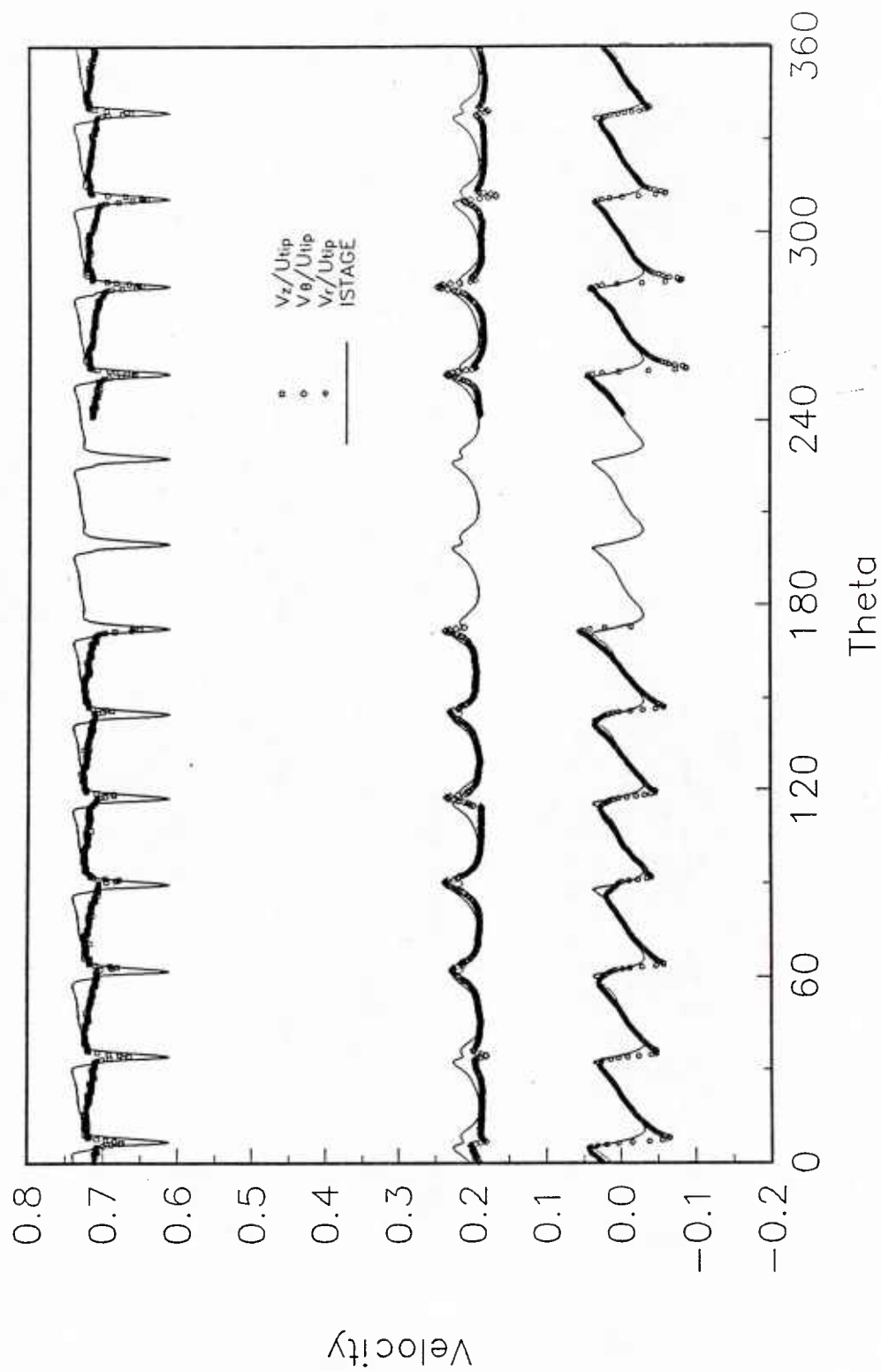


Figure 4.8 Circumferential Variation of Velocity Components 49.7% Chord Axially Downstream of the IGV Trailing Edge--Five-Hole Probe Measurements and ISTAGE Predictions: (c) 19.0% Span

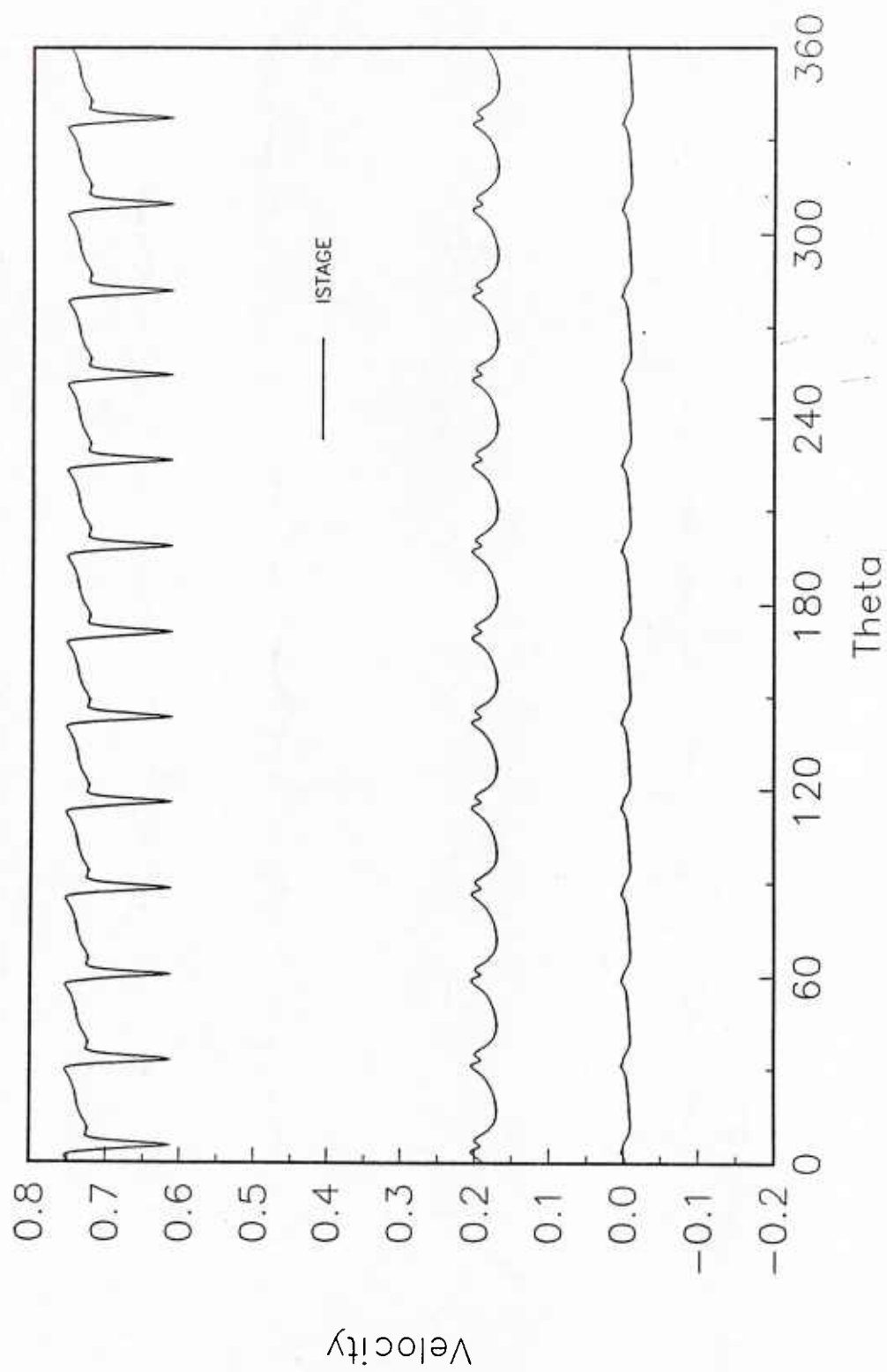


Figure 4.8 Circumferential Variation of Velocity Components 49.7% Chord Axially Downstream of the
IGV Trailing Edge--Five-Hole Probe Measurements and ISTAGE Predictions: (d) 38.1% Span

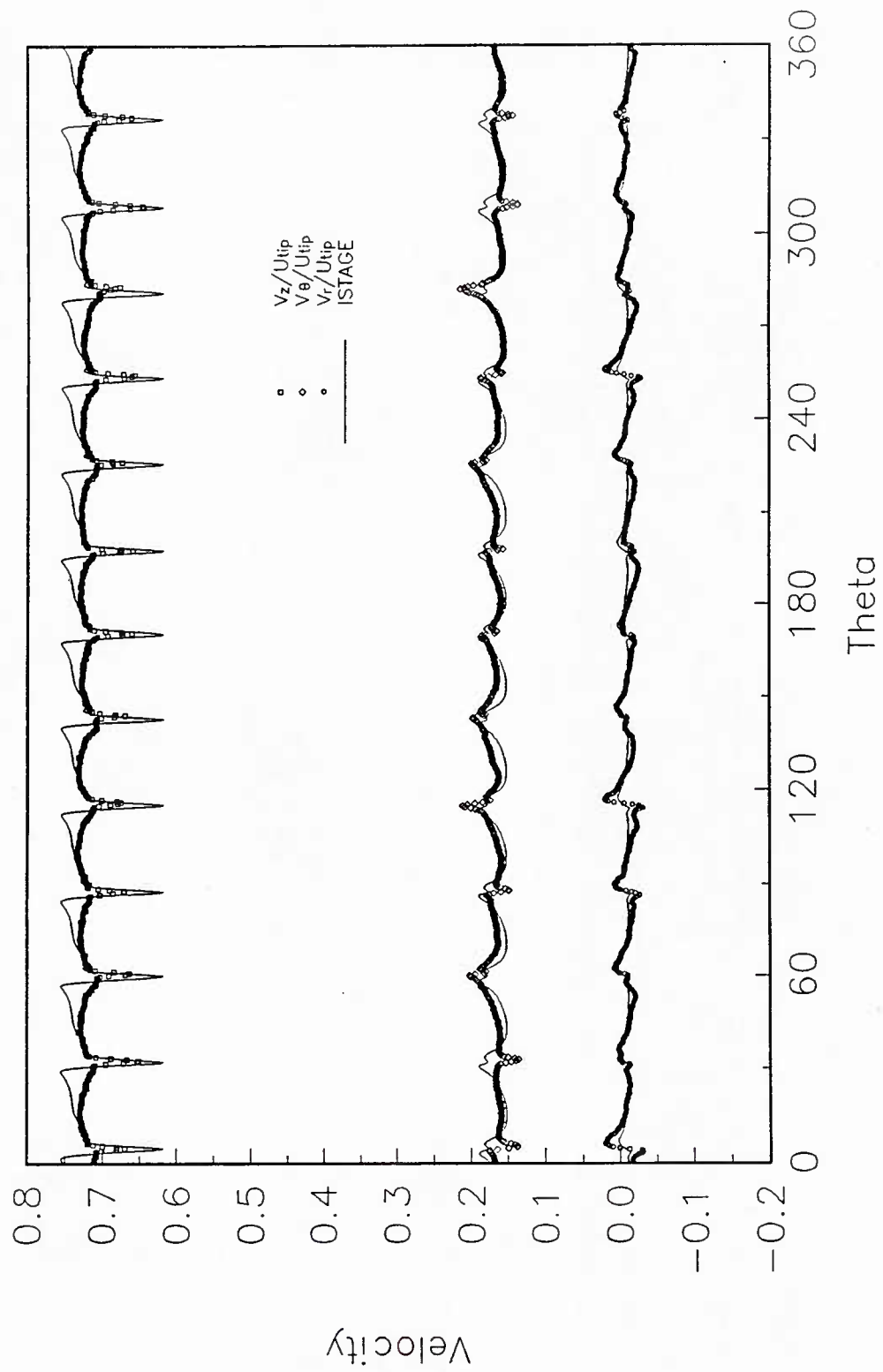


Figure 4.8 Circumferential Variation of Velocity Components 49.7% Chord Axially Downstream of the IGV Trailing Edge--Five-Hole Probe Measurements and ISTAGE Predictions: (e) 52.4% Span

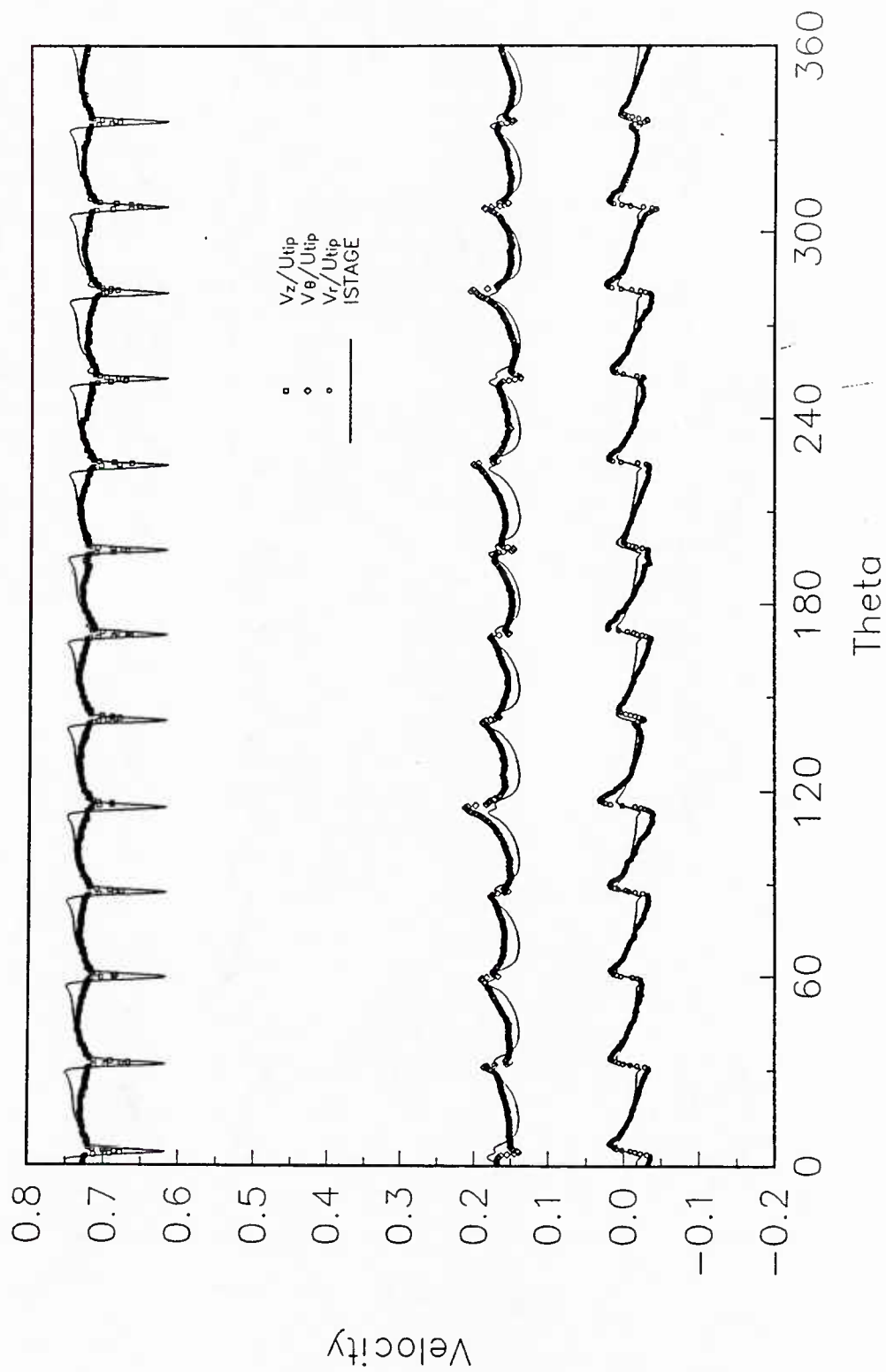


Figure 4.8 Circumferential Variation of Velocity Components 49.7% Chord Axially Downstream of the IGW Trailing Edge--Five-Hole Probe Measurements and ISTAGE Predictions: (f) 61.9% Span

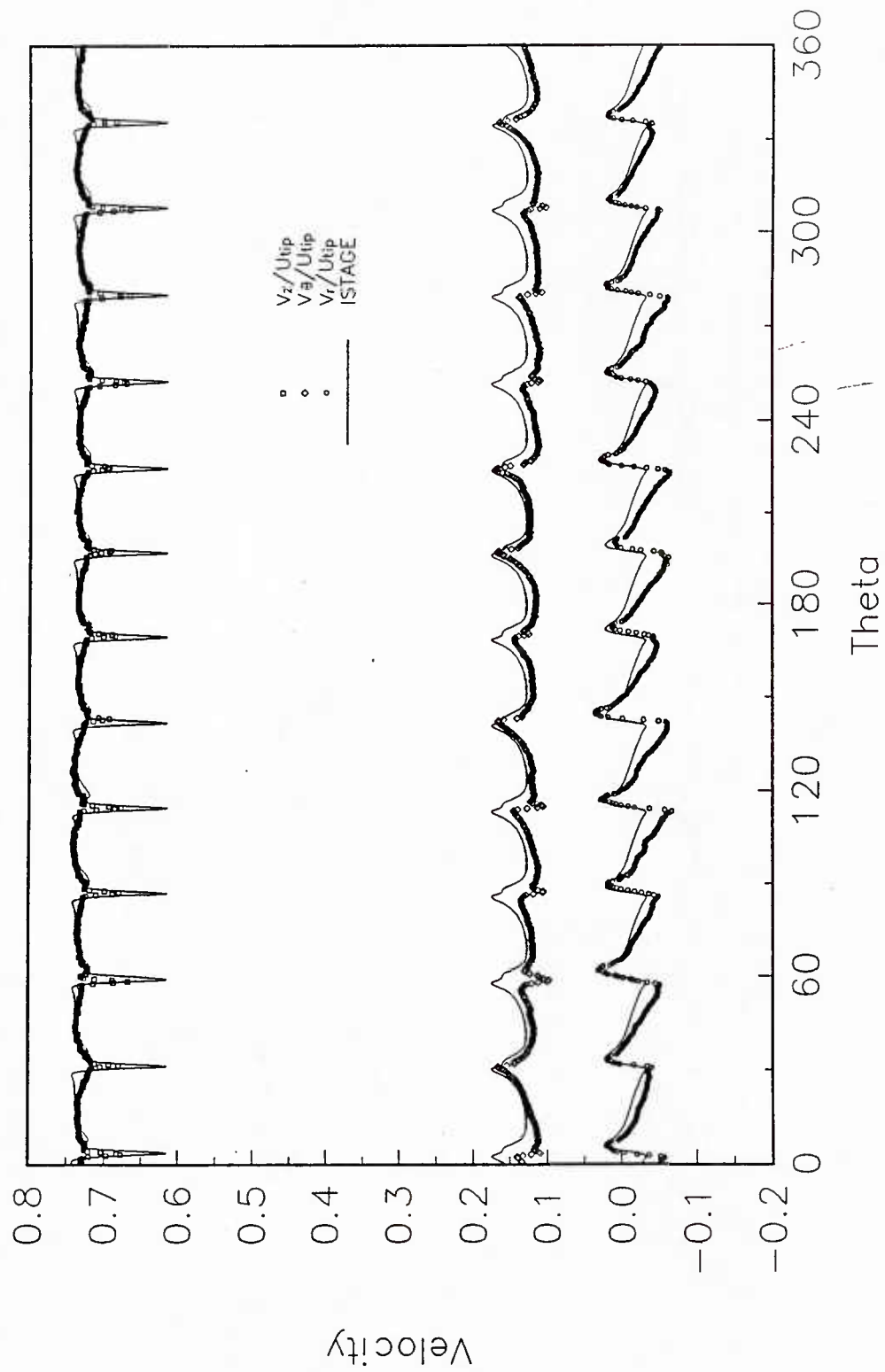


Figure 4.8 Circumferential Variation of Velocity Components 49.7% Chord Axially Downstream of the IGV Trailing Edge--Five-Hole Probe Measurements and ISTAGE Predictions: (g) 71.4% Span

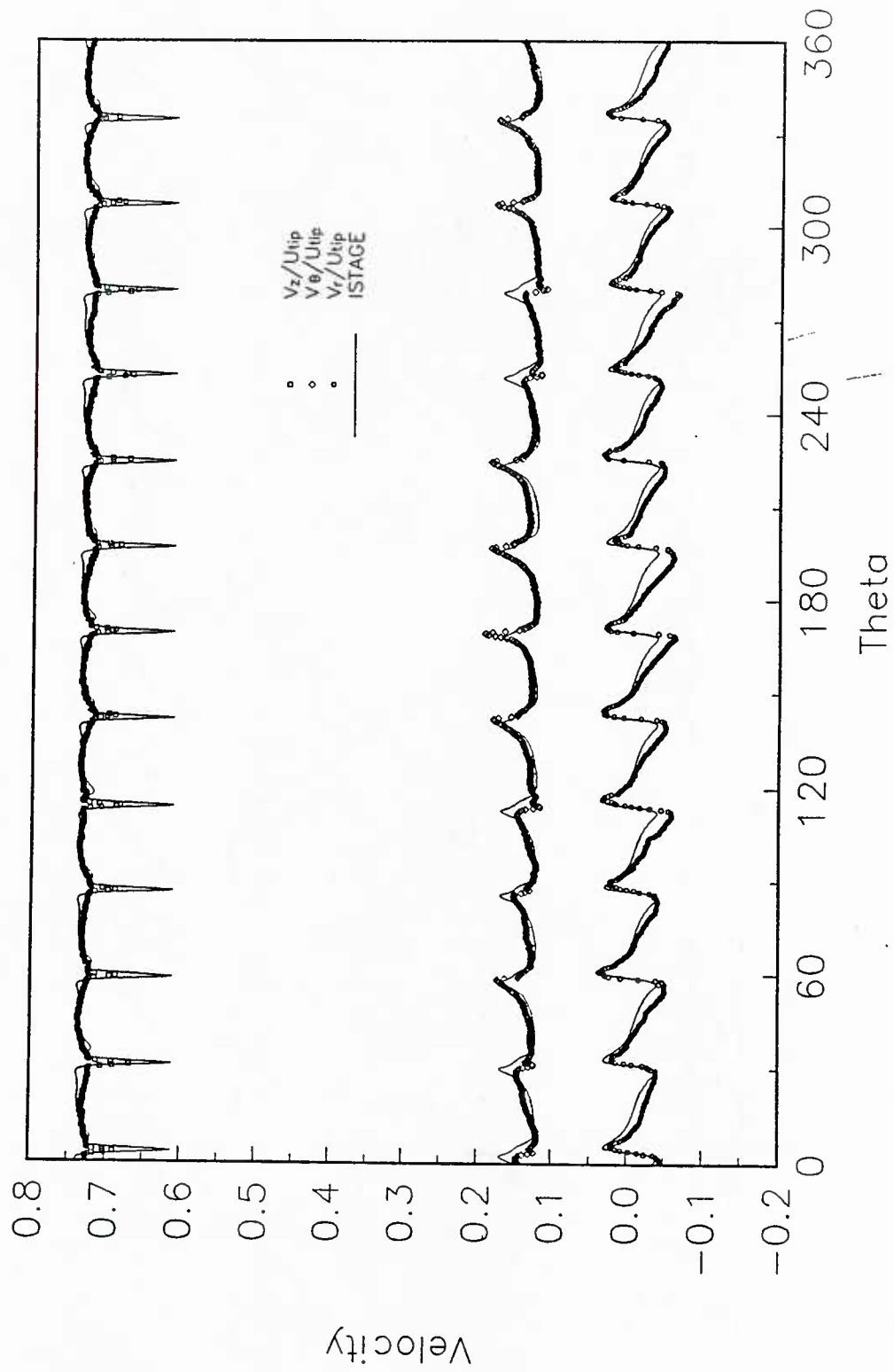


Figure 4.8 Circumferential Variation of Velocity Components 49.7% Chord Axially Downstream of the IGV Trailing Edge--Five-Hole Probe Measurements and ISTAGE Predictions: (h) 76.2% Span

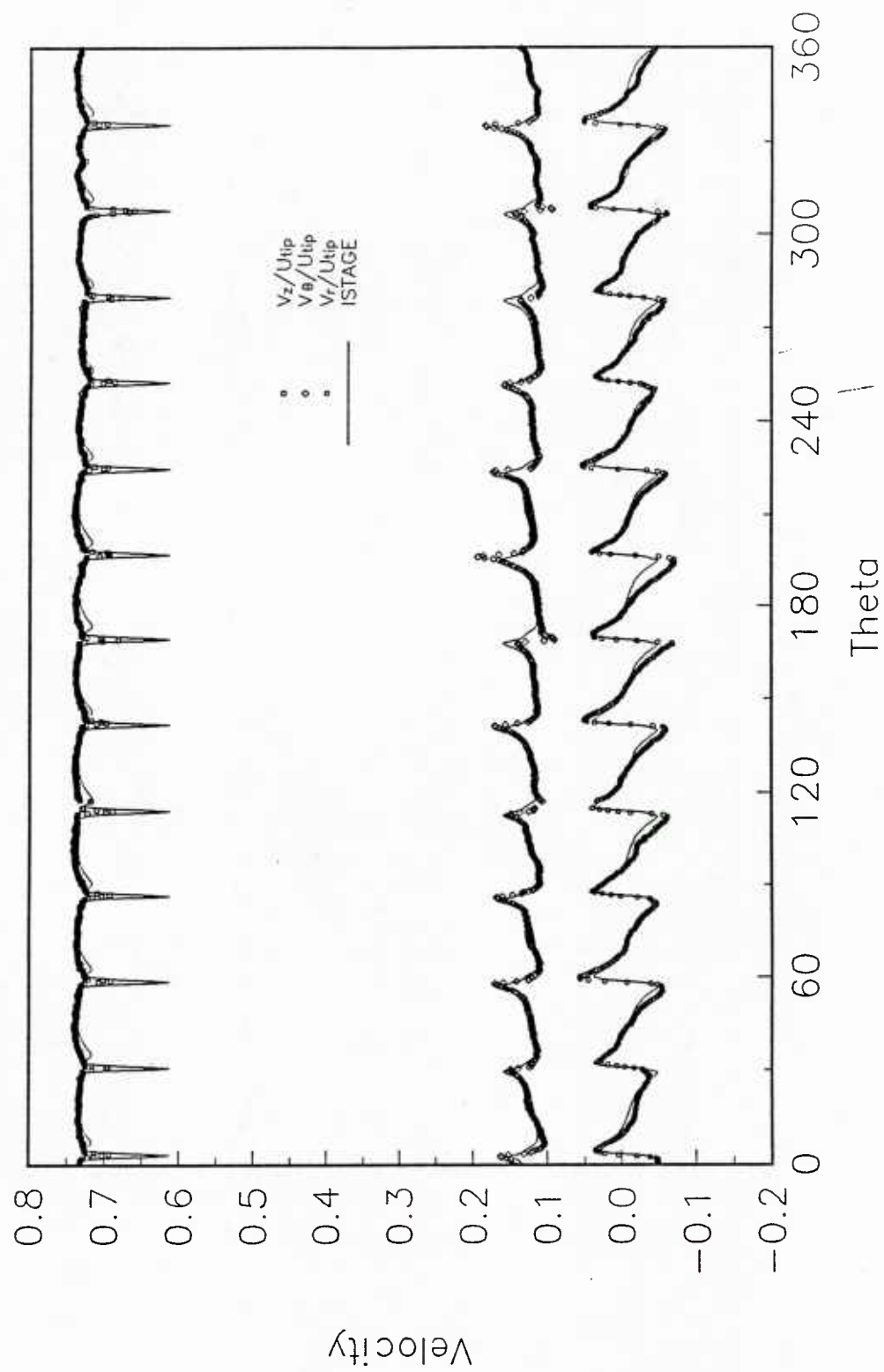


Figure 4.8 Circumferential Variation of Velocity Components 49.7% Chord Axially Downstream of the IGV Trailing Edge--Five-Hole Probe Measurements and ISTAGE Predictions: (i) 81.0% Span

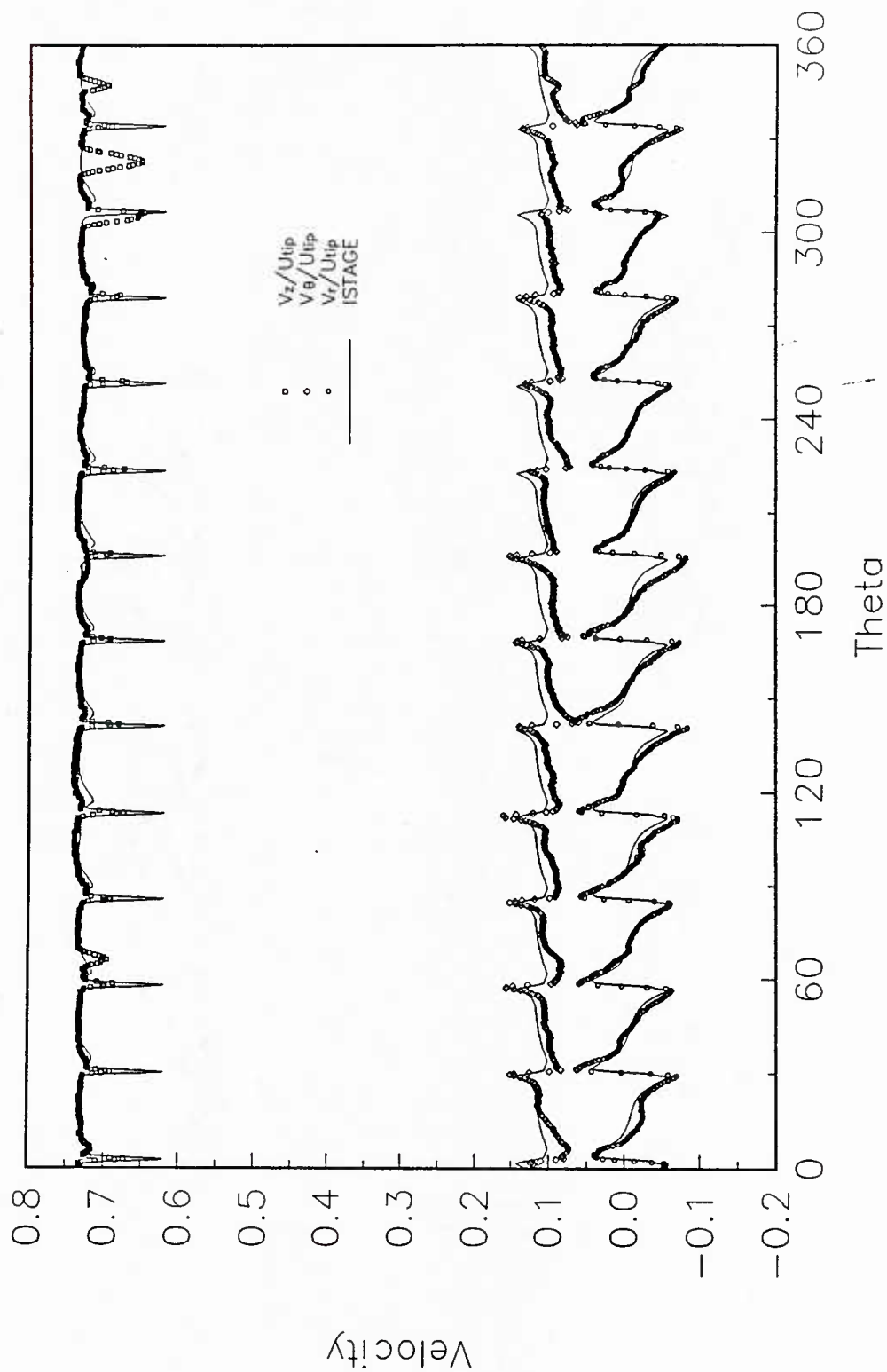


Figure 4.8 Circumferential Variation of Velocity Components 49.7% Chord Axially Downstream of the IGV Trailing Edge--Five-Hole Probe Measurements and ISTAGE Predictions: (j) 85.7% Span

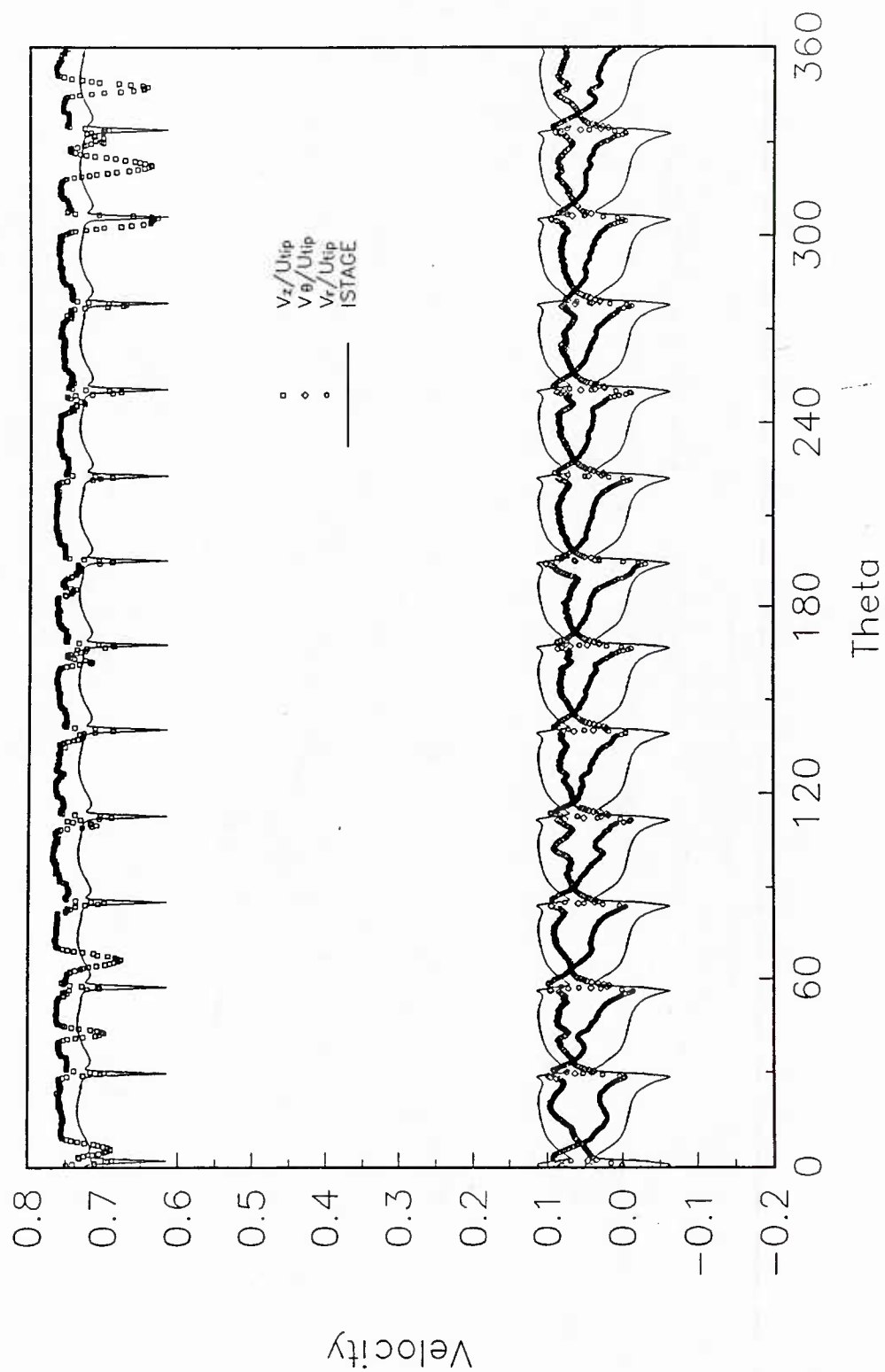


Figure 4.8 Circumferential Variation of Velocity Components 49.7% Chord Axially Downstream of the IGV Trailing Edge--Five-Hole Probe Measurements and ISTAGE Predictions: (k) 90.5% Span

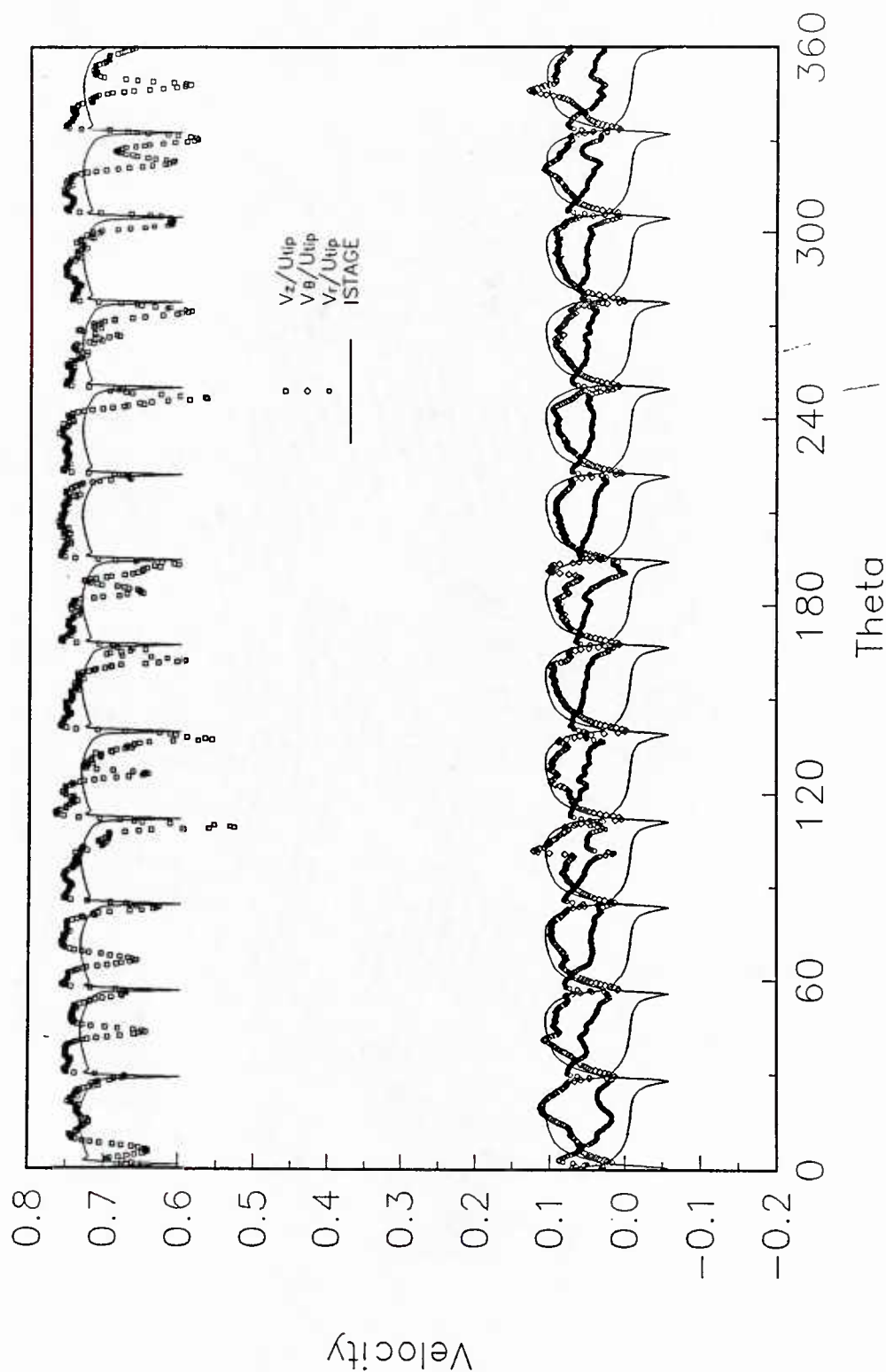


Figure 4.8 Circumferential Variation of Velocity Components 49.7% Chord Axially Downstream of the IGV Trailing Edge--Five-Hole Probe Measurements and ISTAGE Predictions: (l) 95.2% Span

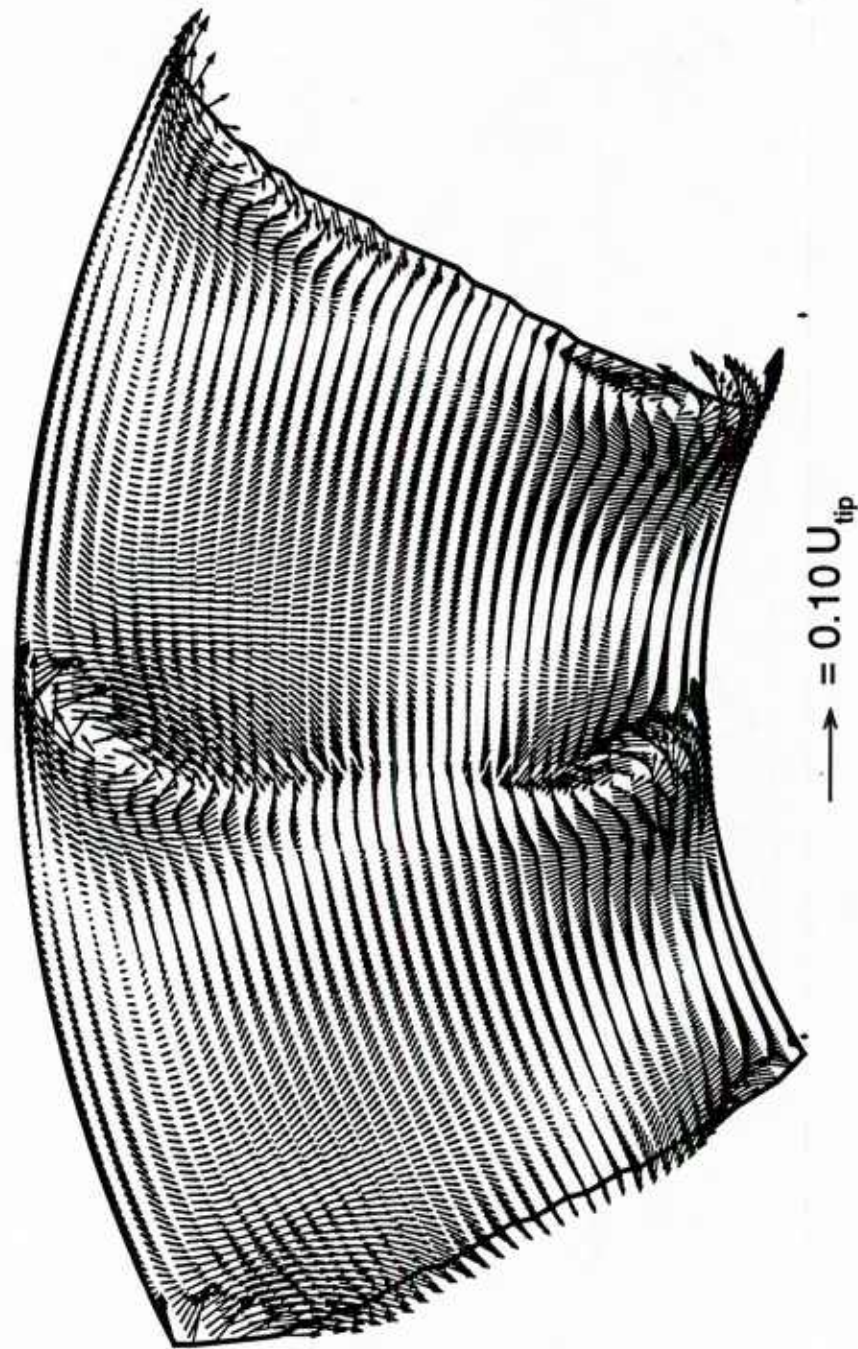


Figure 4.9 Secondary Velocity Vectors 49.7% Chord Axially Downstream of the IGV Trailing Edge: (a) ISTAGE Predictions

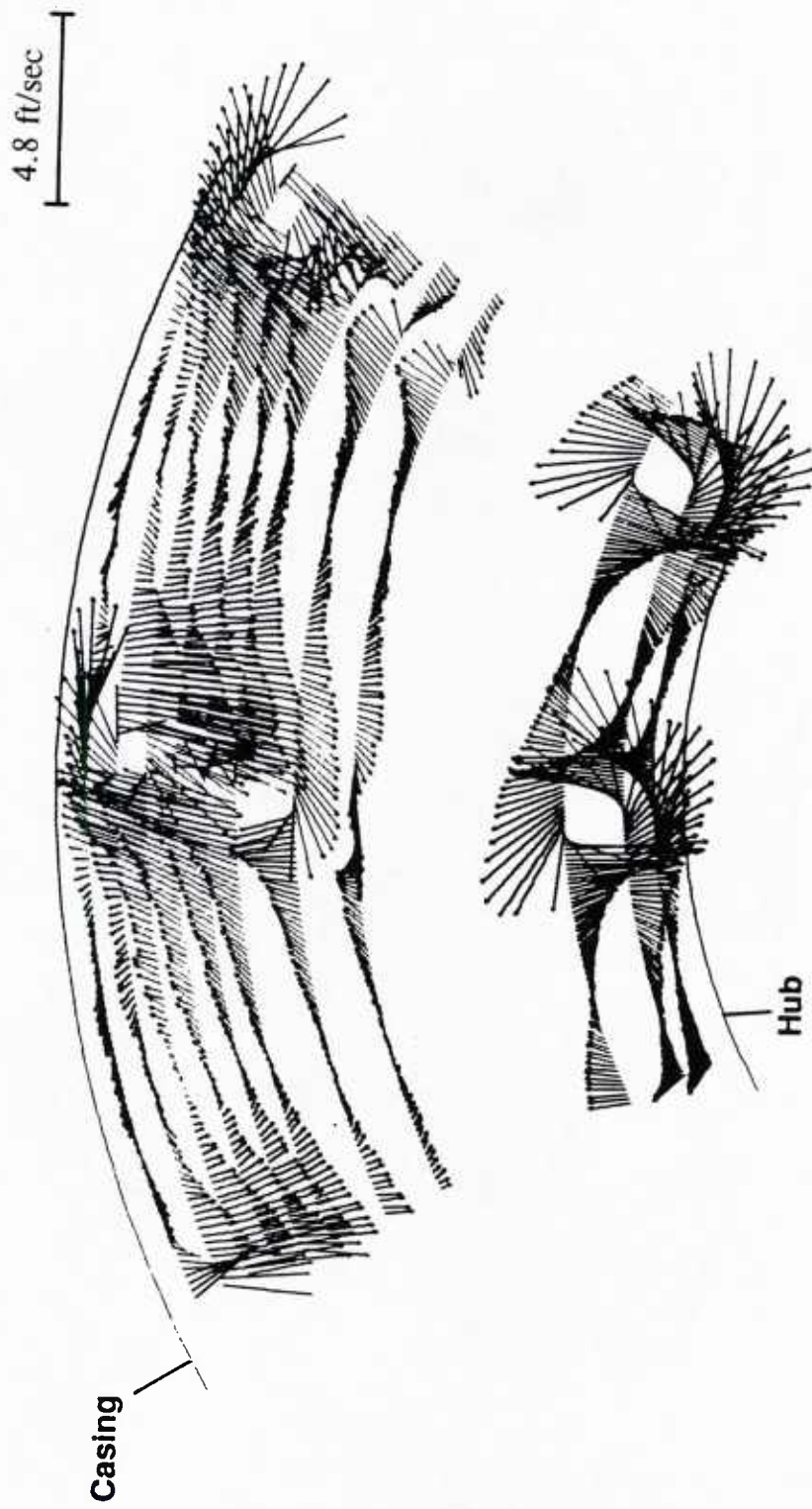


Figure 4.9 Secondary Velocity Vectors 49.7% Chord Axially Downstream of the IGV Trailing Edge: (b) Five-Hole Probe Rake Surveys

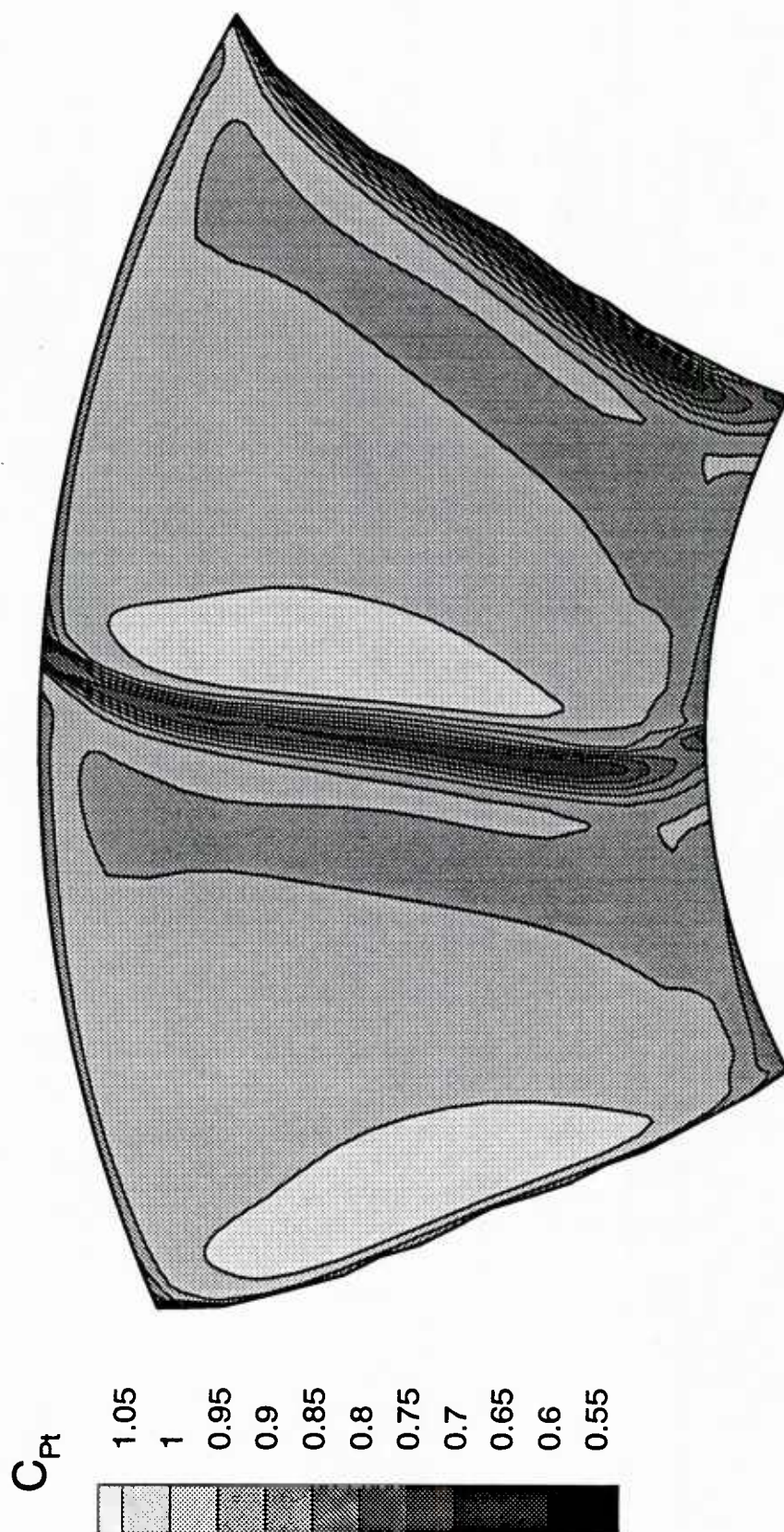


Figure 4.10 Total-Pressure Coefficient Contours 49.7% Chord Axially Downstream of the IGV Trailing Edge: (a) ISTAGE Predictions

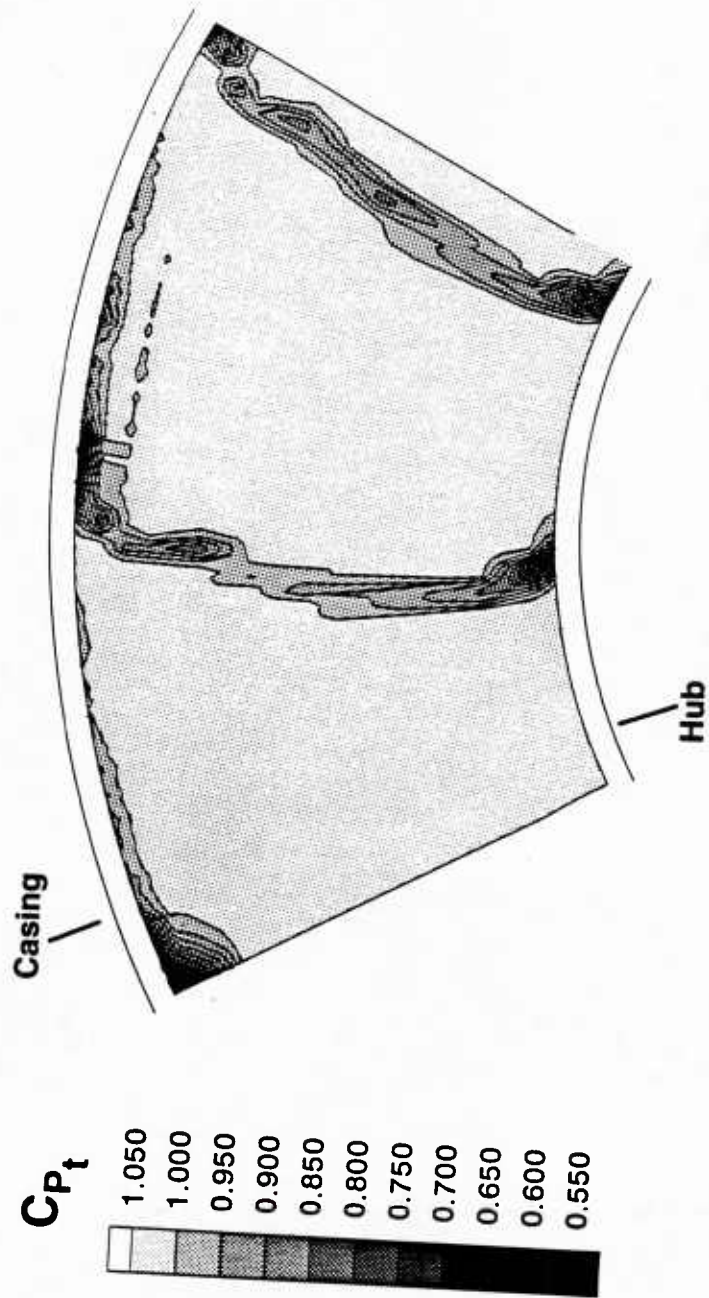


Figure 4.10 Total-Pressure Coefficient Contours 49.7% Chord Axially Downstream of the IGV Trailing Edge: (b) Five-Hole Probe Rake Surveys

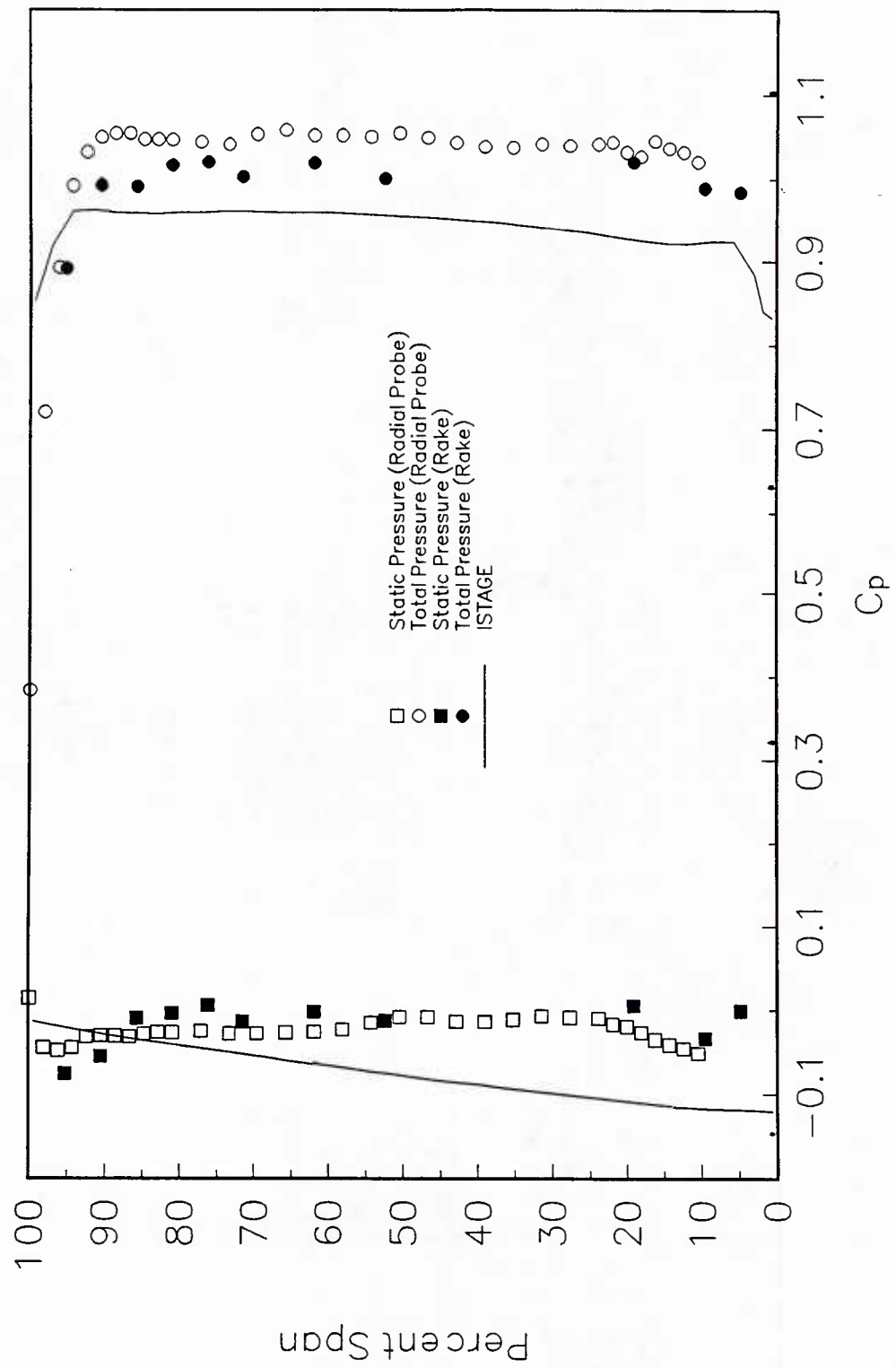


Figure 4.11 Circumferentially-Averaged Pressure Coefficients 49.7%
Chord Axially Downstream of the IGV Trailing Edge

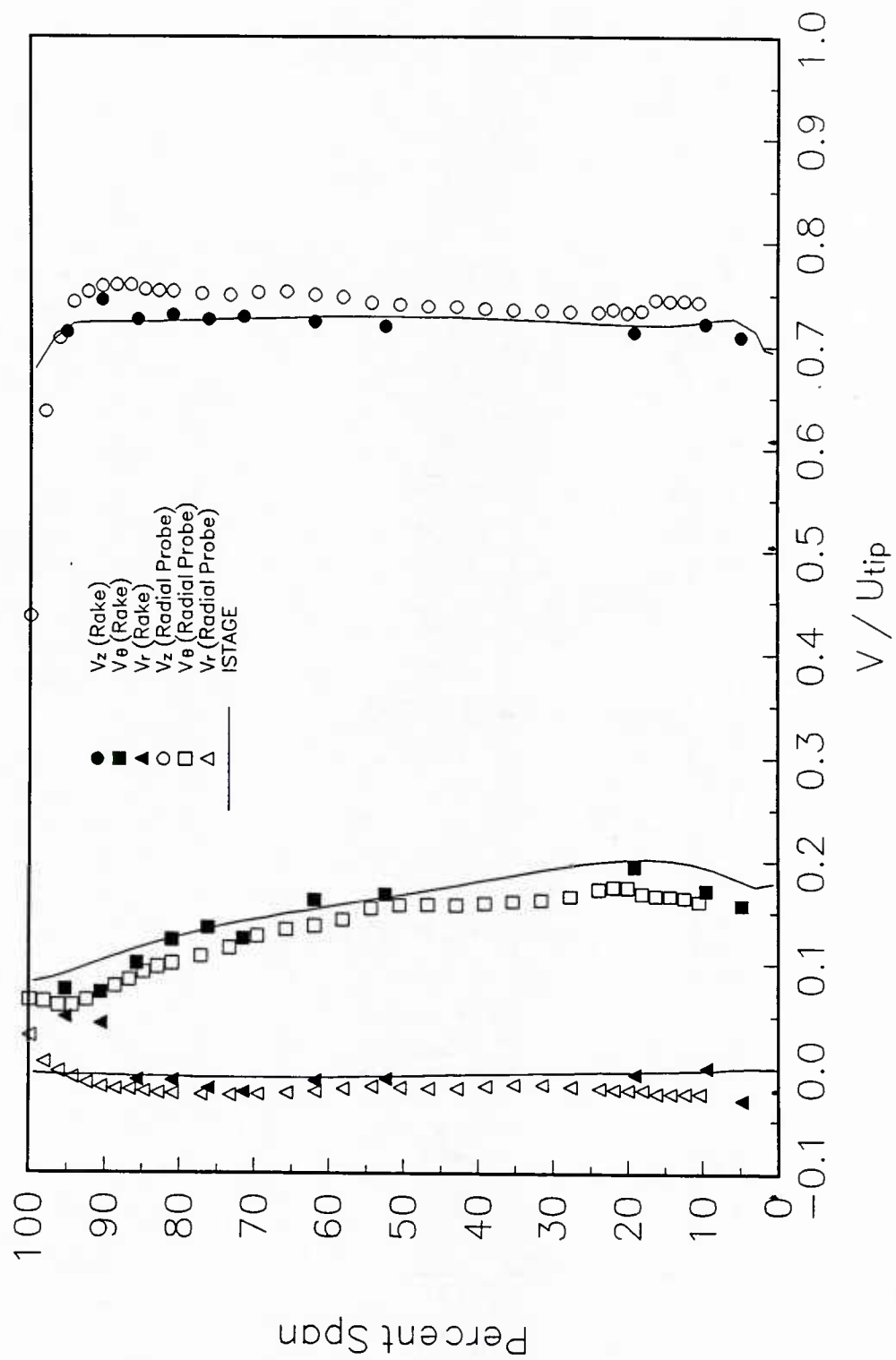


Figure 4.12 Circumferentially-Averaged Velocities 49.7%
Chord Axially Downstream of the IGV Trailing Edge

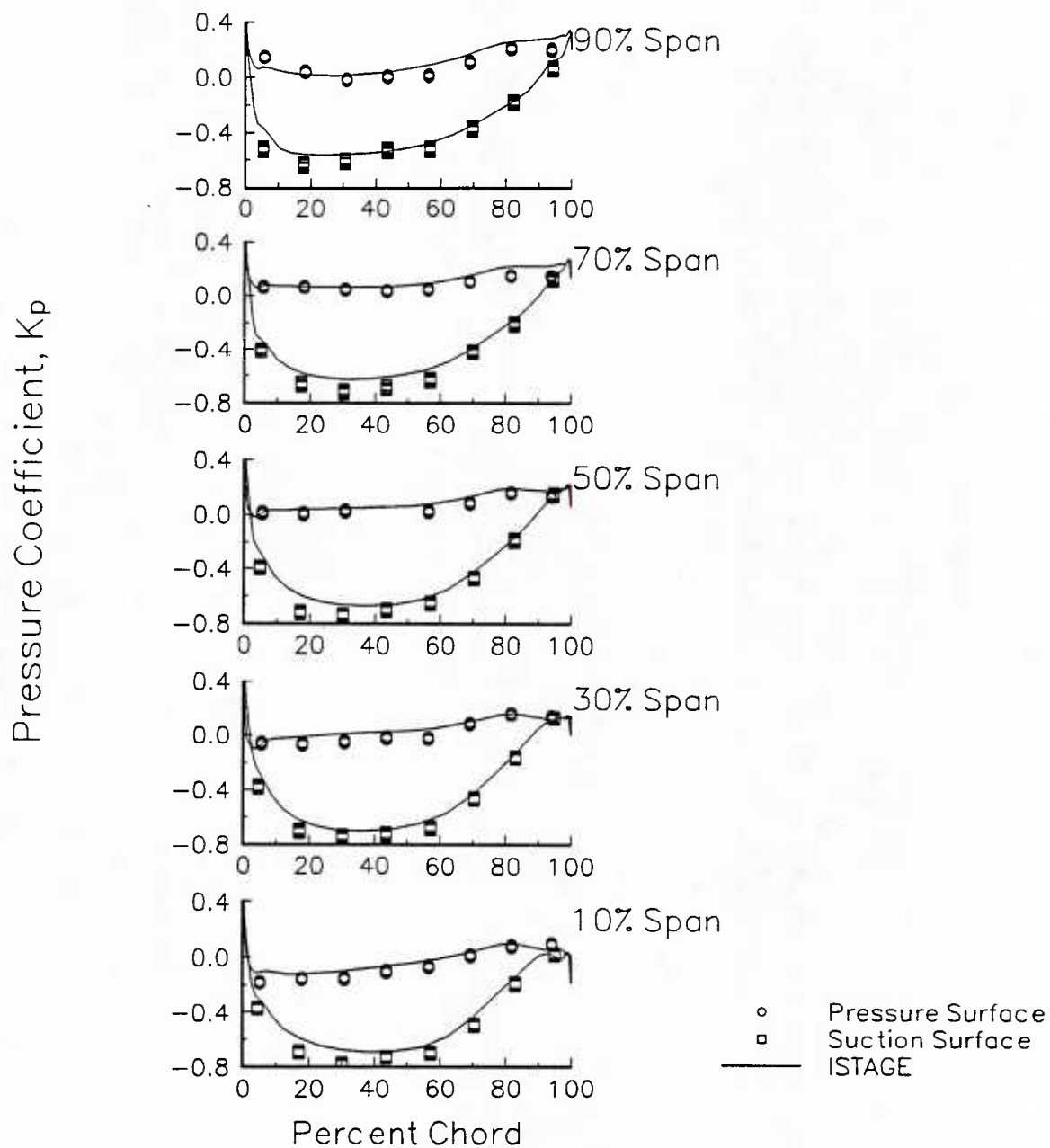


Figure 4.13 Rotor Blade Static-Pressure Distribution

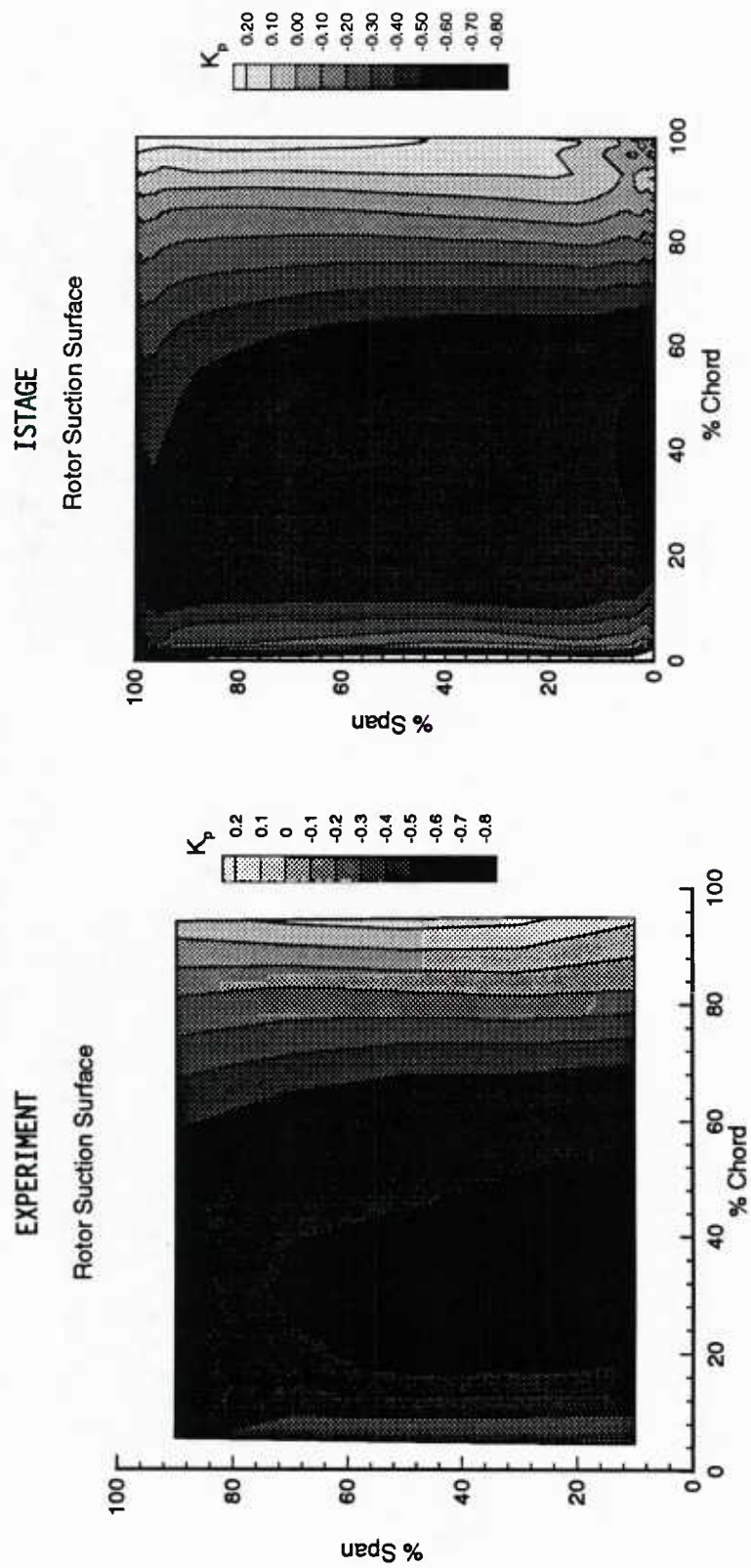


Figure 4.14 Rotor Blade Suction Surface Static-Pressure Contours

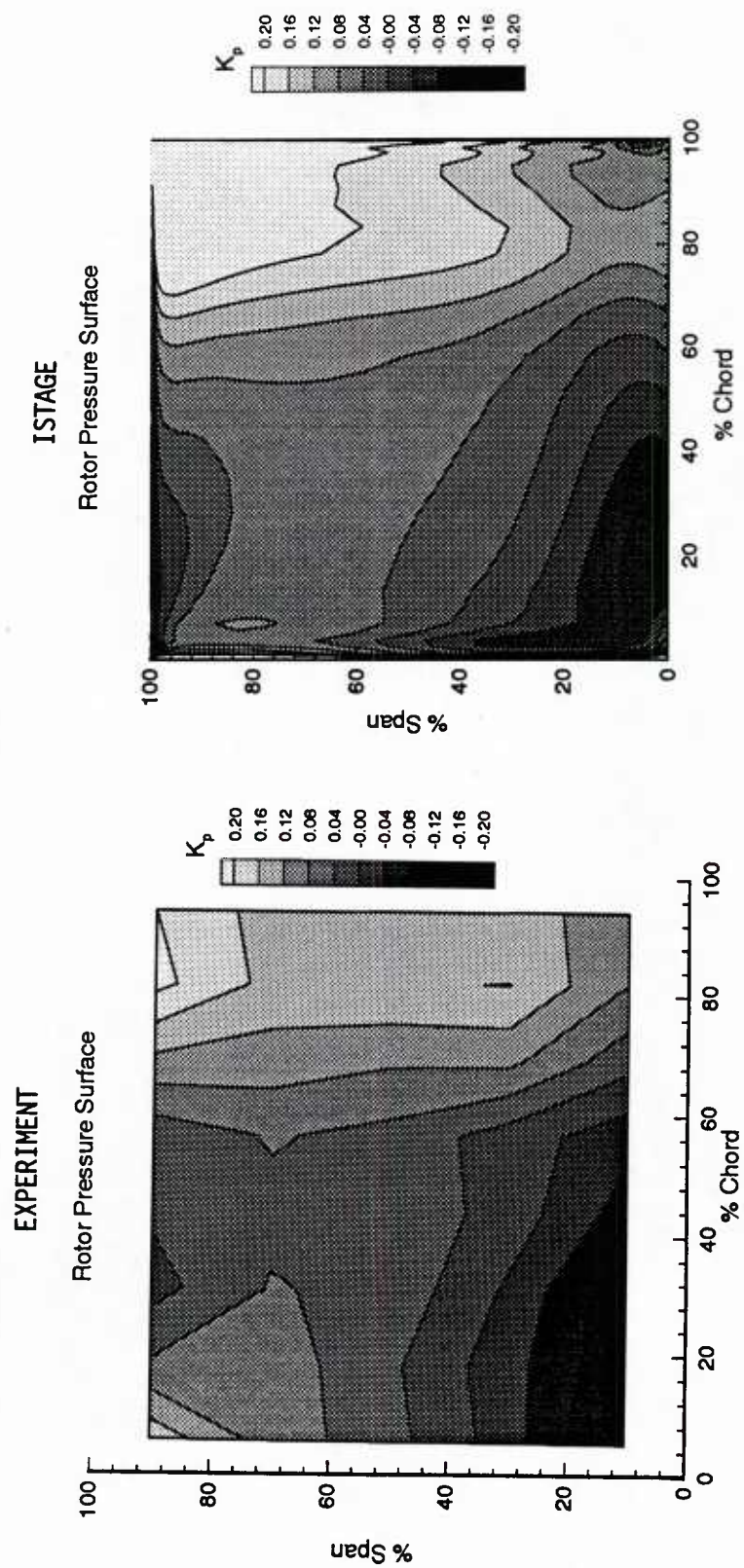


Figure 4.15 Rotor Blade Pressure Surface Static-Pressure Contours

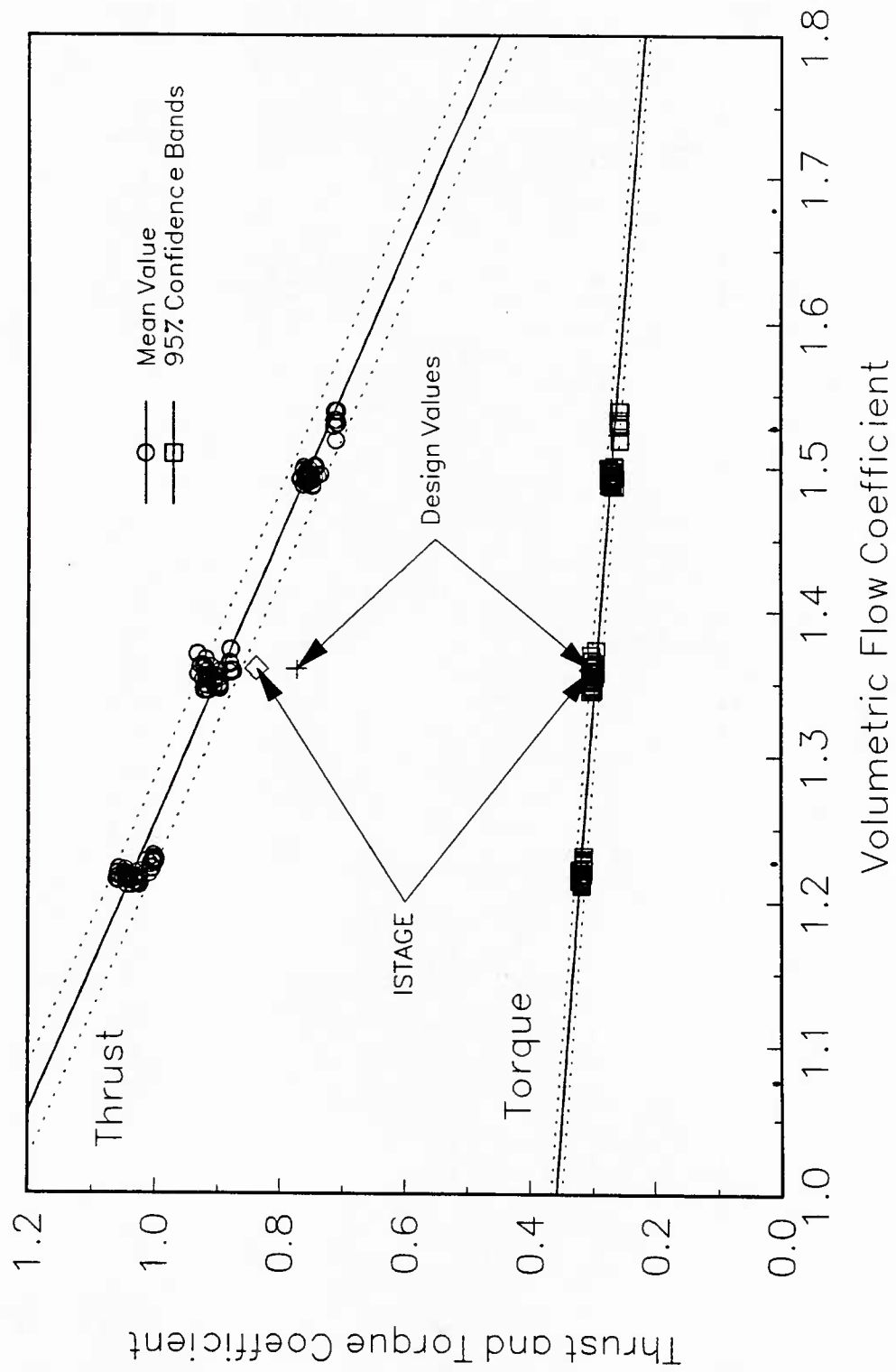
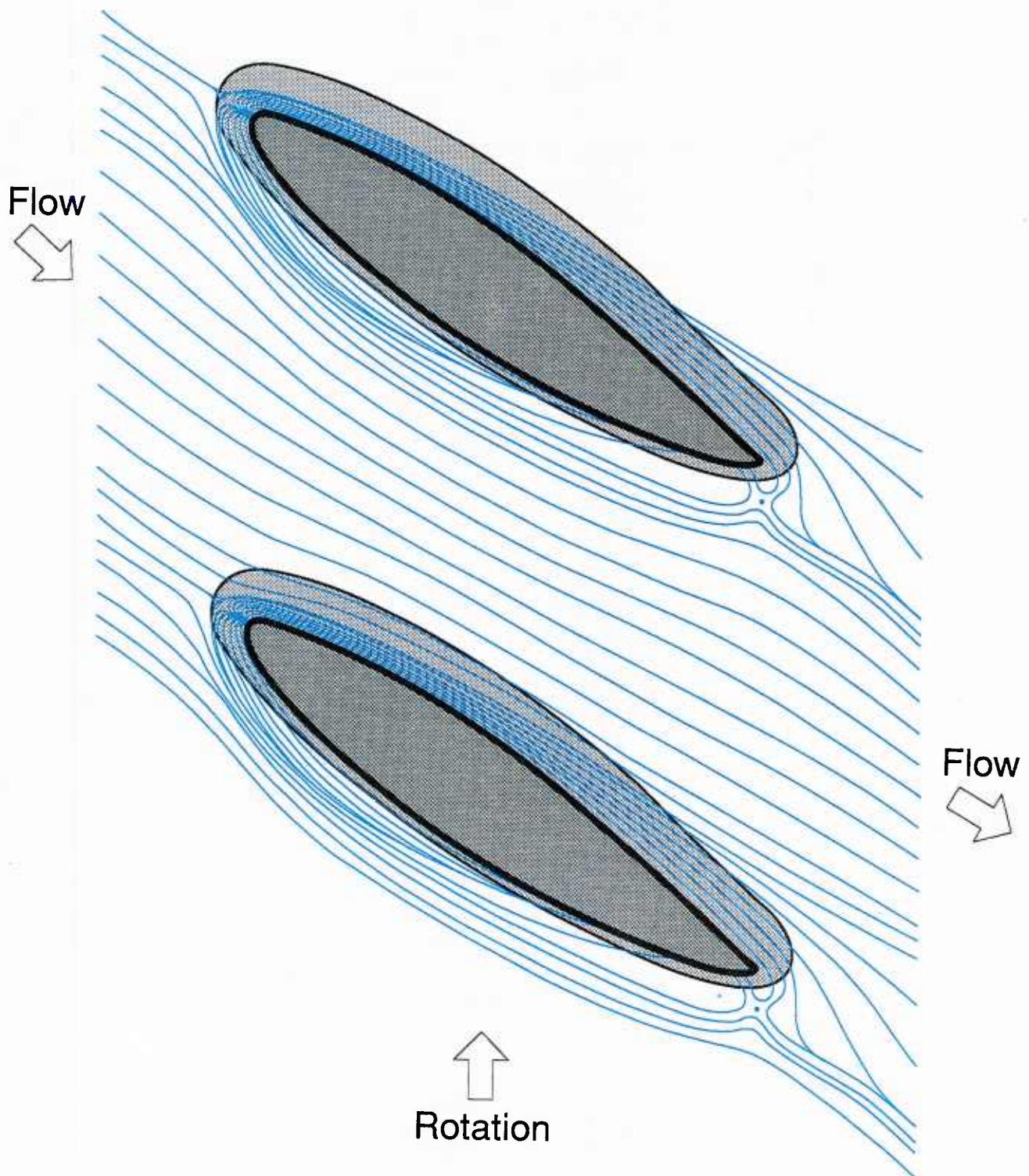


Figure 4.16 Variation of Rotor Shaft Thrust and Torque with Volumetric Flow Coefficient



4.17 Predicted Particle Paths, One Grid Point from the Rotor Blade Hub



4.18 Schematic of Surface Flow Visualization on the Rotor Blade Hub Surface

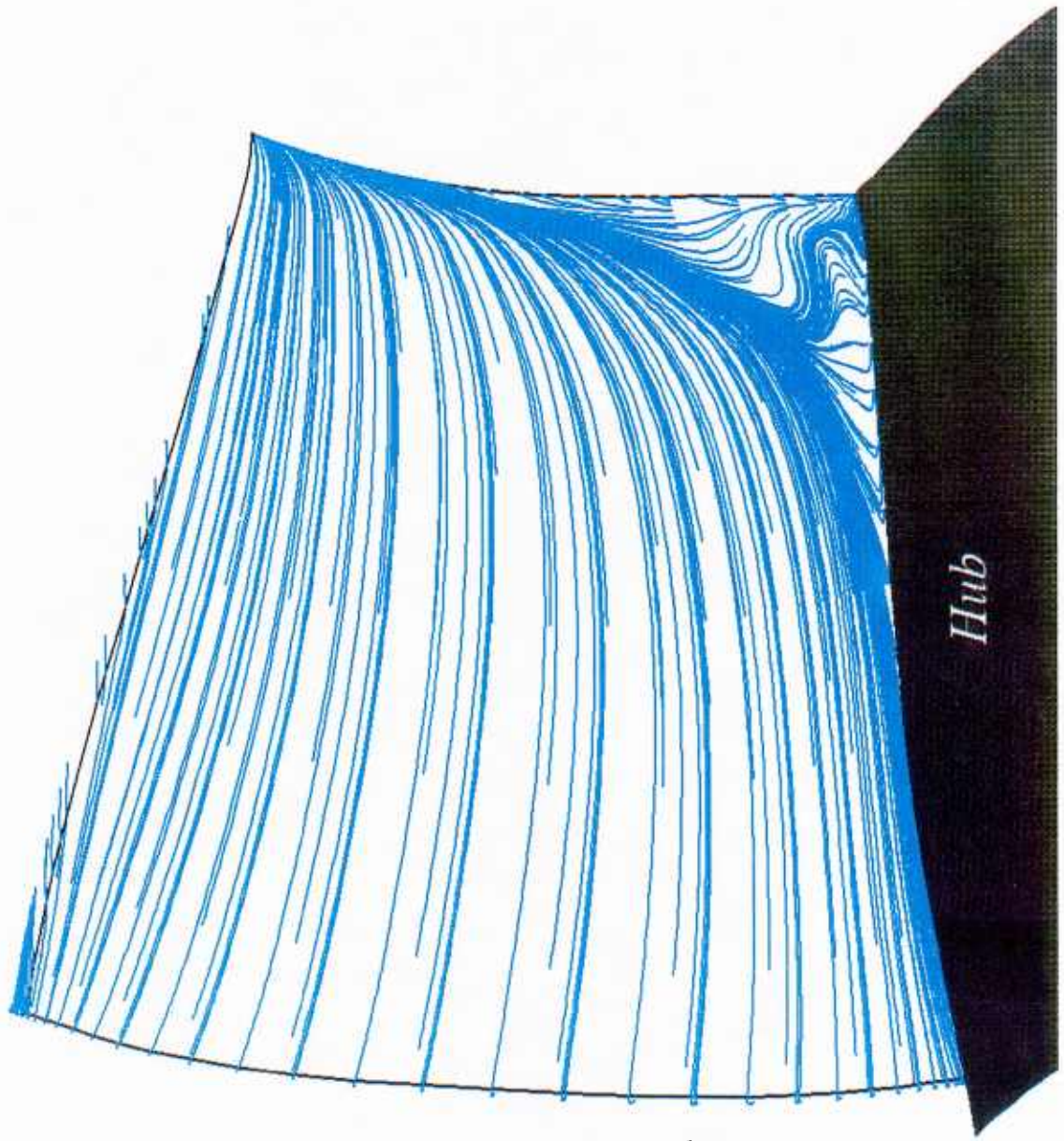
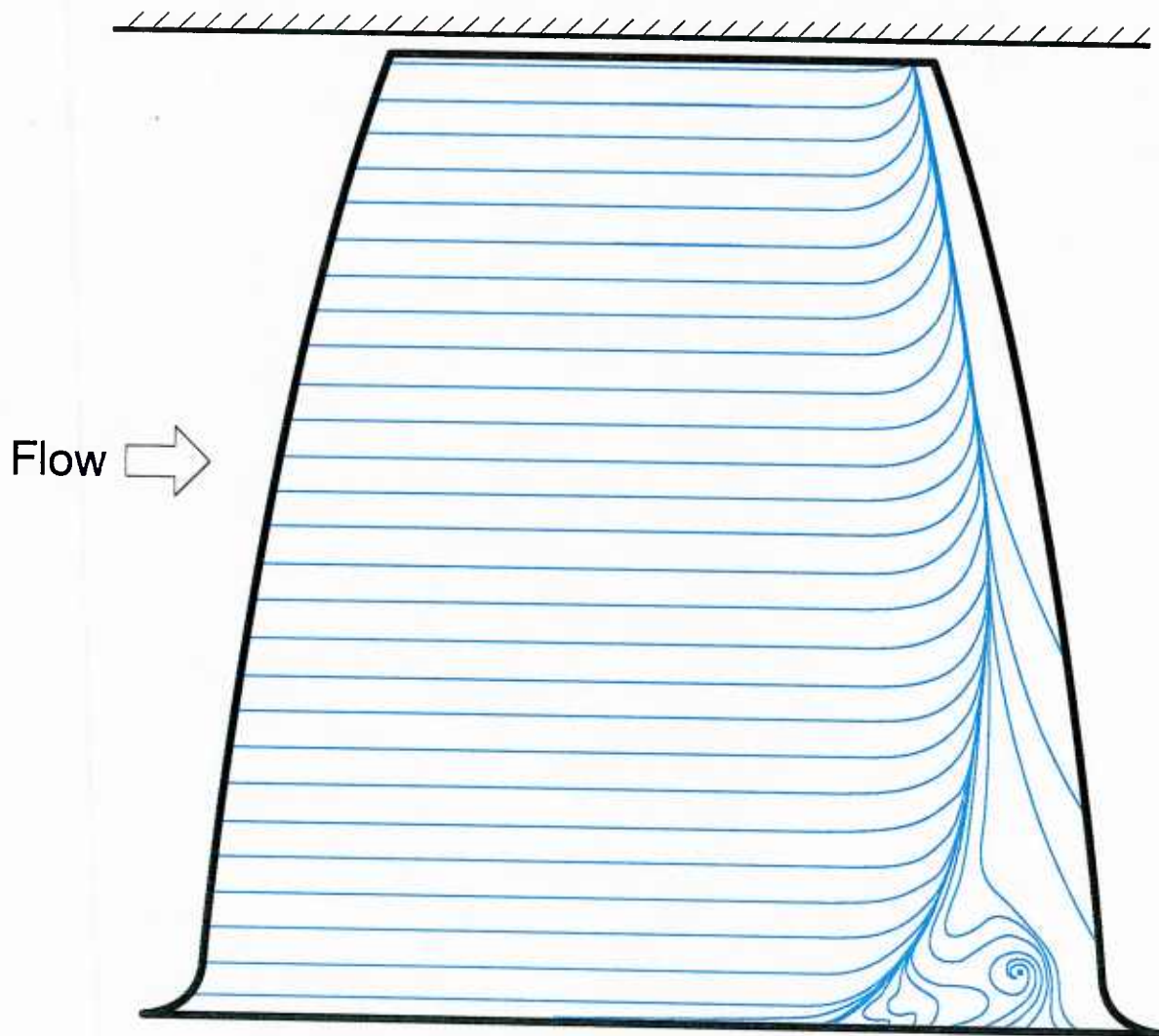


Figure 4.19 Predicted Particle Paths, One Grid Point from the Rotor Blade Suction Surface



4.20 Schematic of Surface Flow Visualization on the Rotor Blade Suction Surface

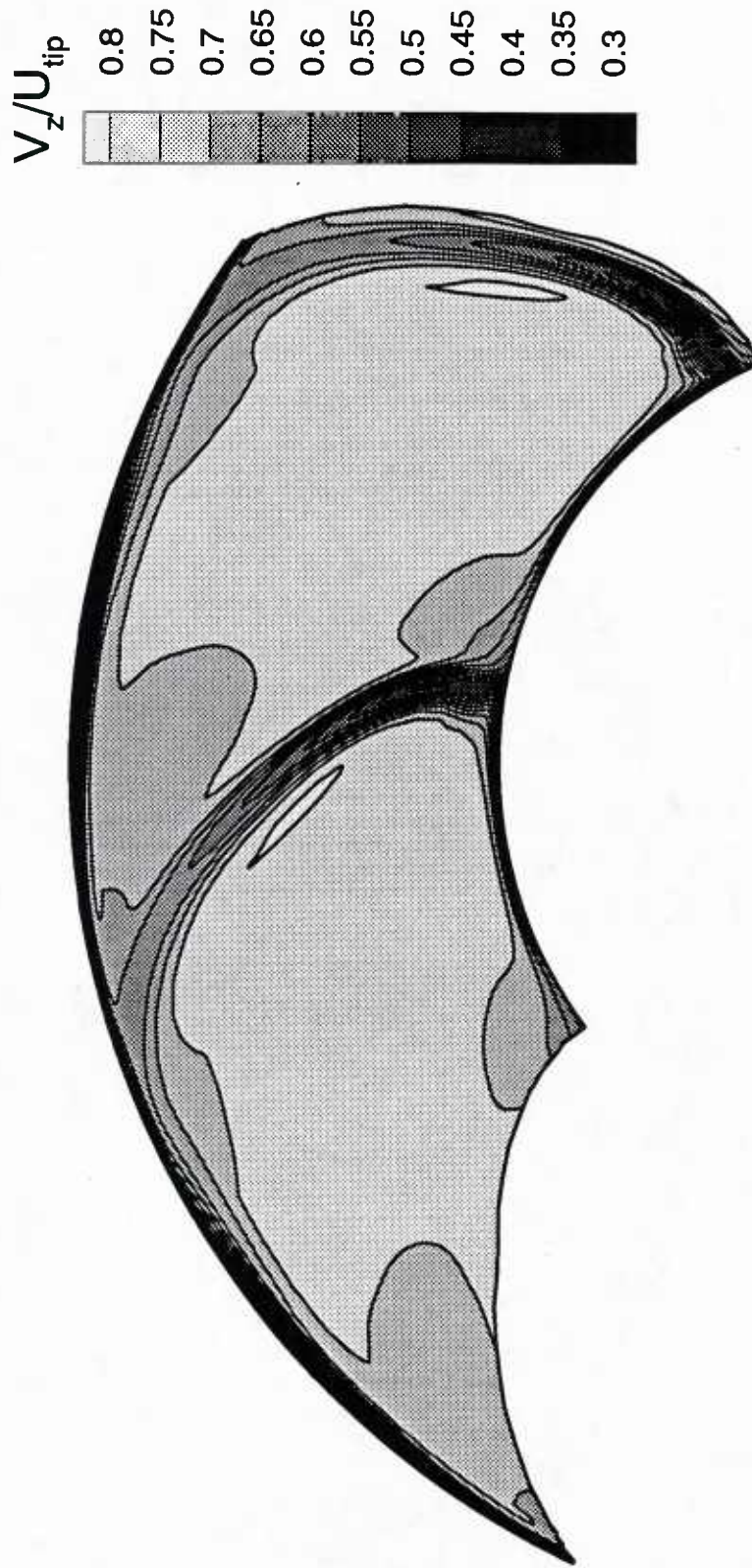


Figure 4.21 Axial Velocity Contours 32.2% Chord Axially Downstream of the Rotor Tip Trailing Edge: (a) ISTAGE Predictions

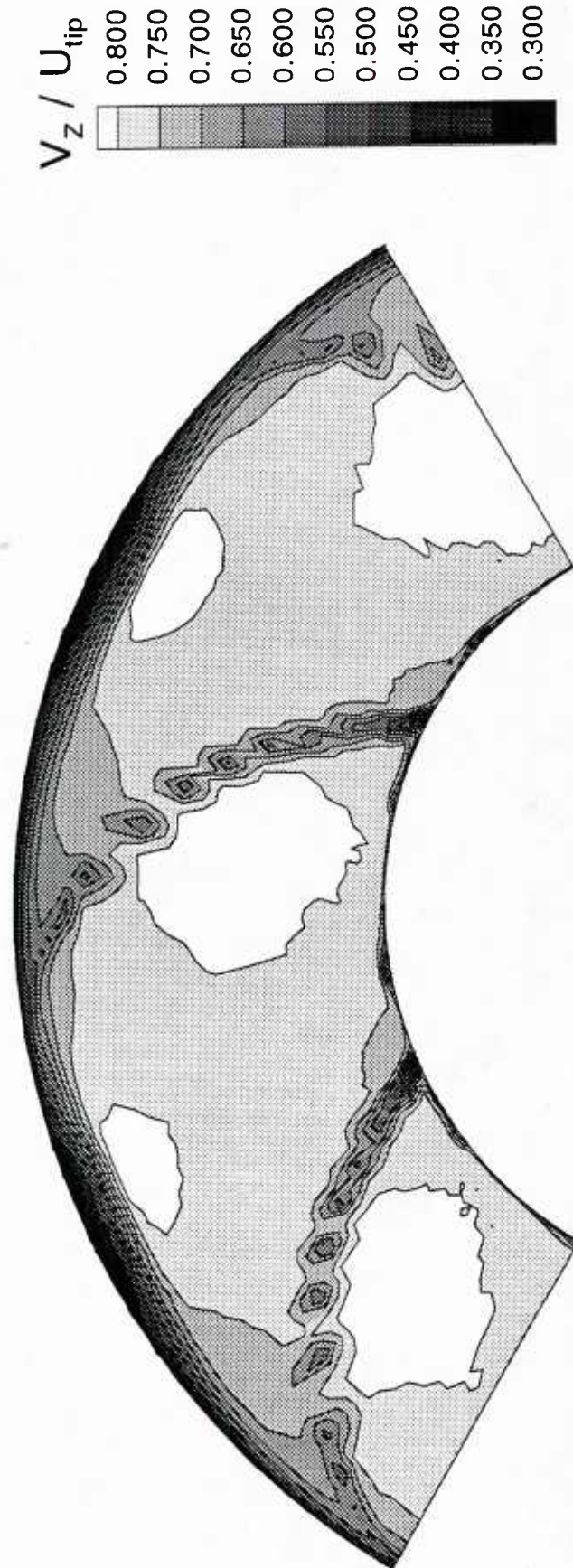


Figure 4.21 Axial Velocity Contours 32.3% Chord Axially Downstream of the Rotor Tip Trailing Edge: (b) LDV Measurements

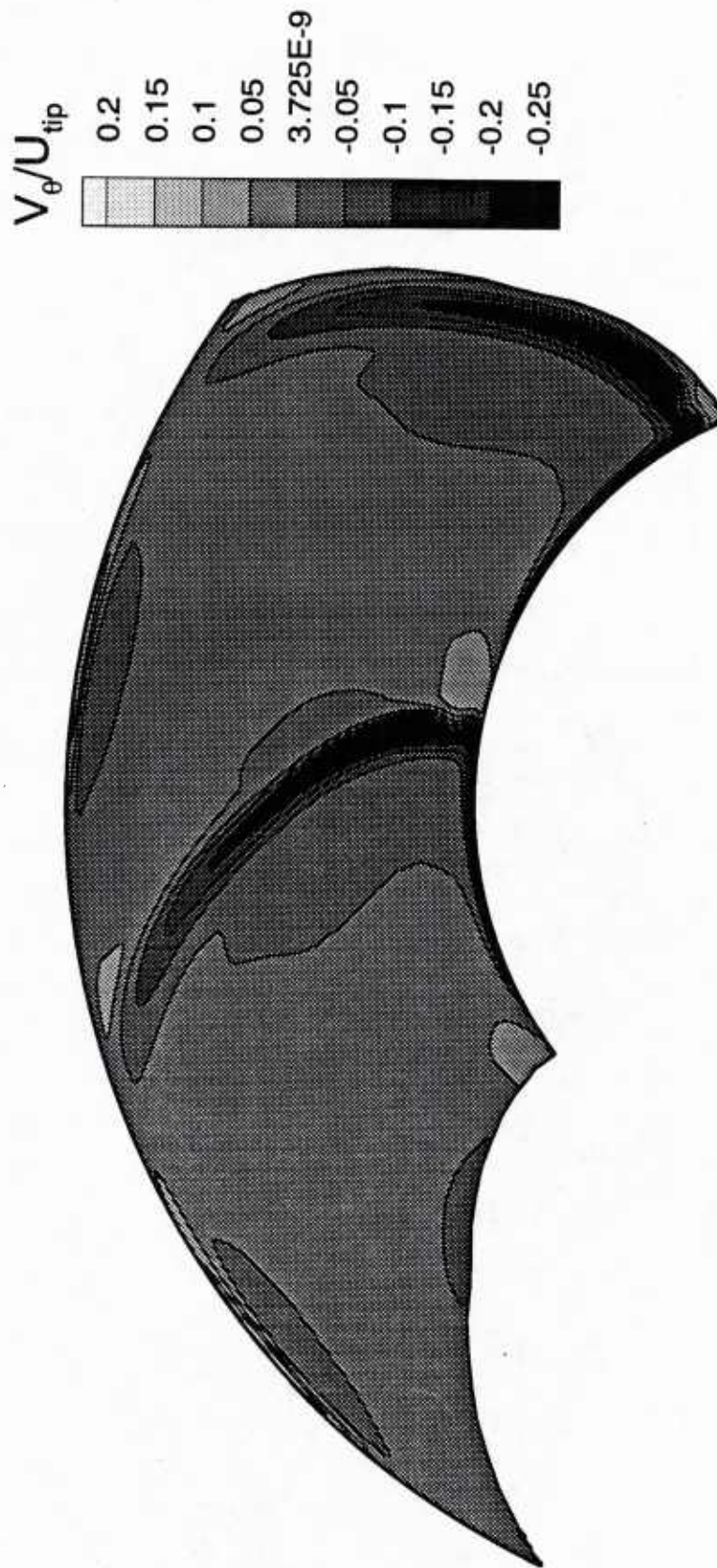


Figure 4.22 Tangential Velocity Contours 32.2% Chord Axially Downstream of the Rotor Tip Trailing Edge: (a) ISTAGE Predictions



Figure 4.22 Tangential Velocity Contours 32.2% Chord Axially Downstream of the Rotor Tip Trailing Edge: (b) LDV Measurements

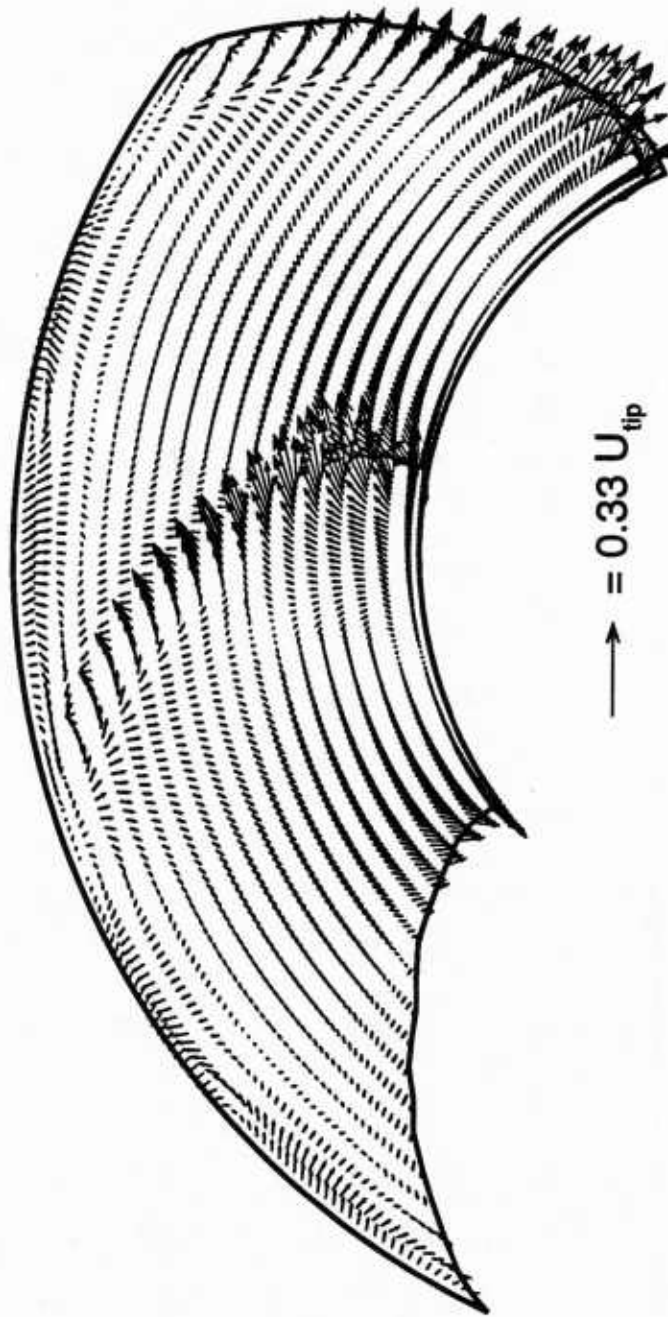


Figure 4.23 Predicted Secondary Velocity Vectors 32.2% Chord Axially Downstream of the Rotor Tip Trailing Edge

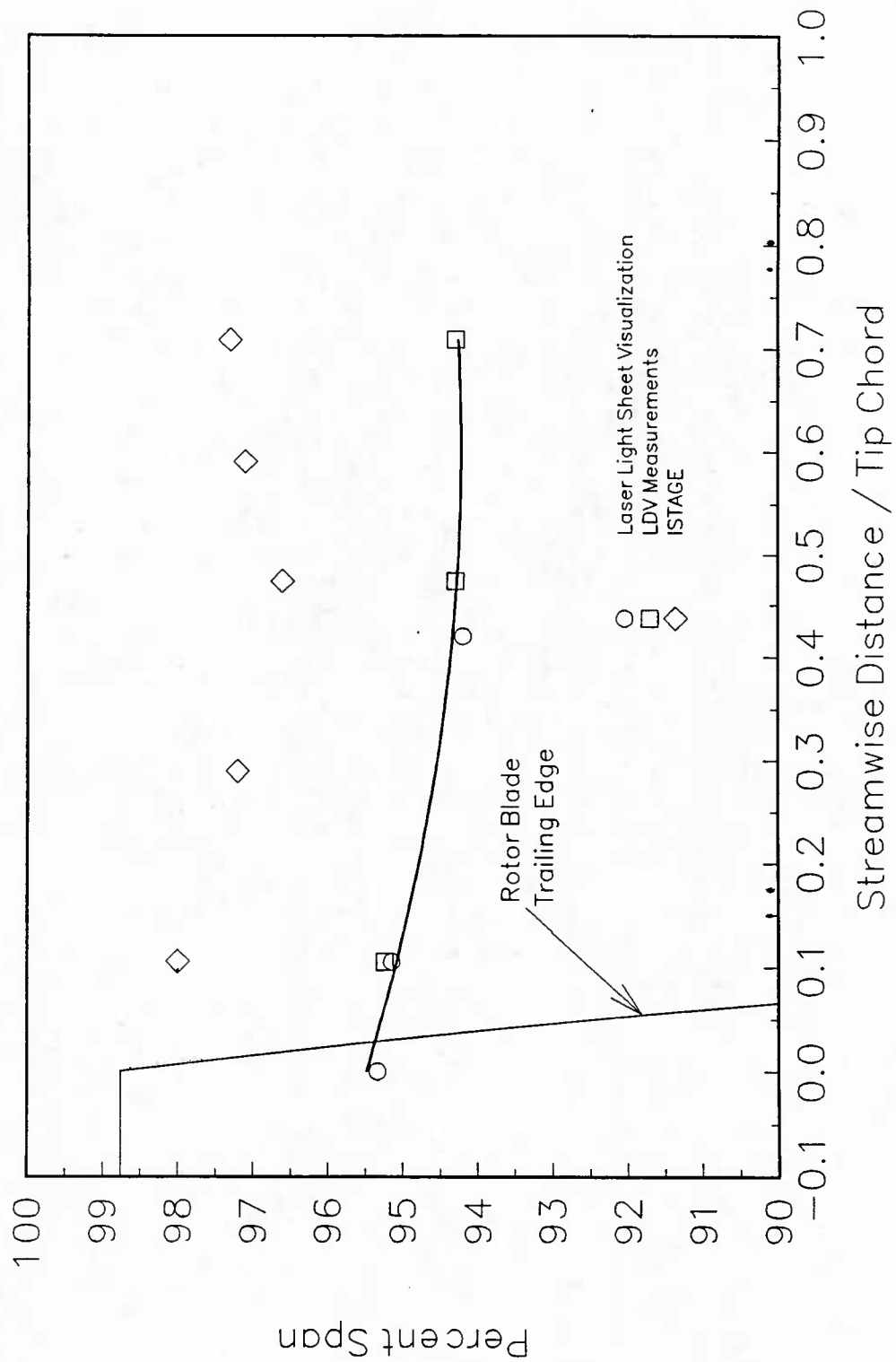


Figure 4.24 Spanwise Position of the Core of the Rotor Tip Leakage Vortex

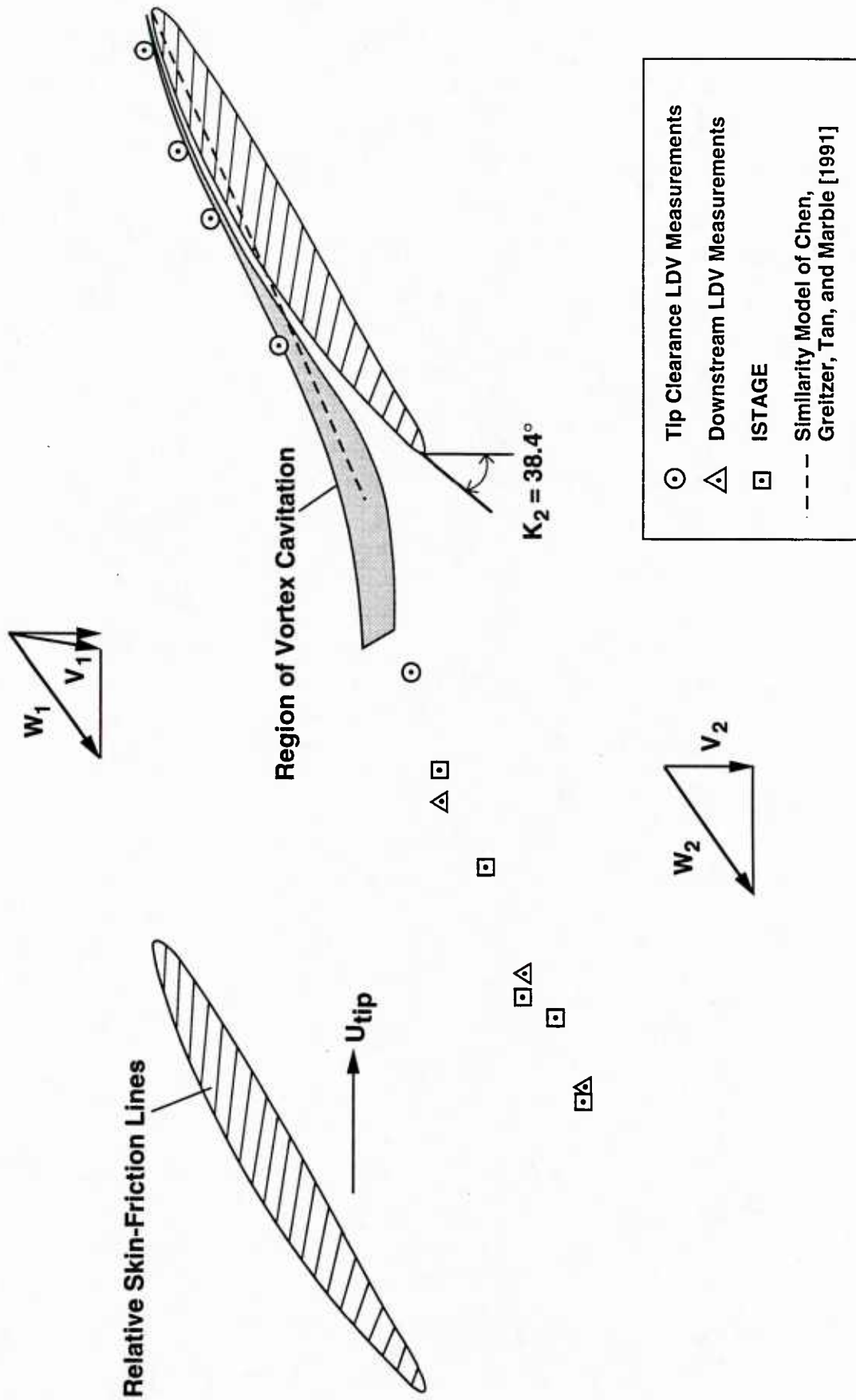


Figure 4.25 Blade-to-Blade Position of the Core of the Rotor Tip Leakage Vortex

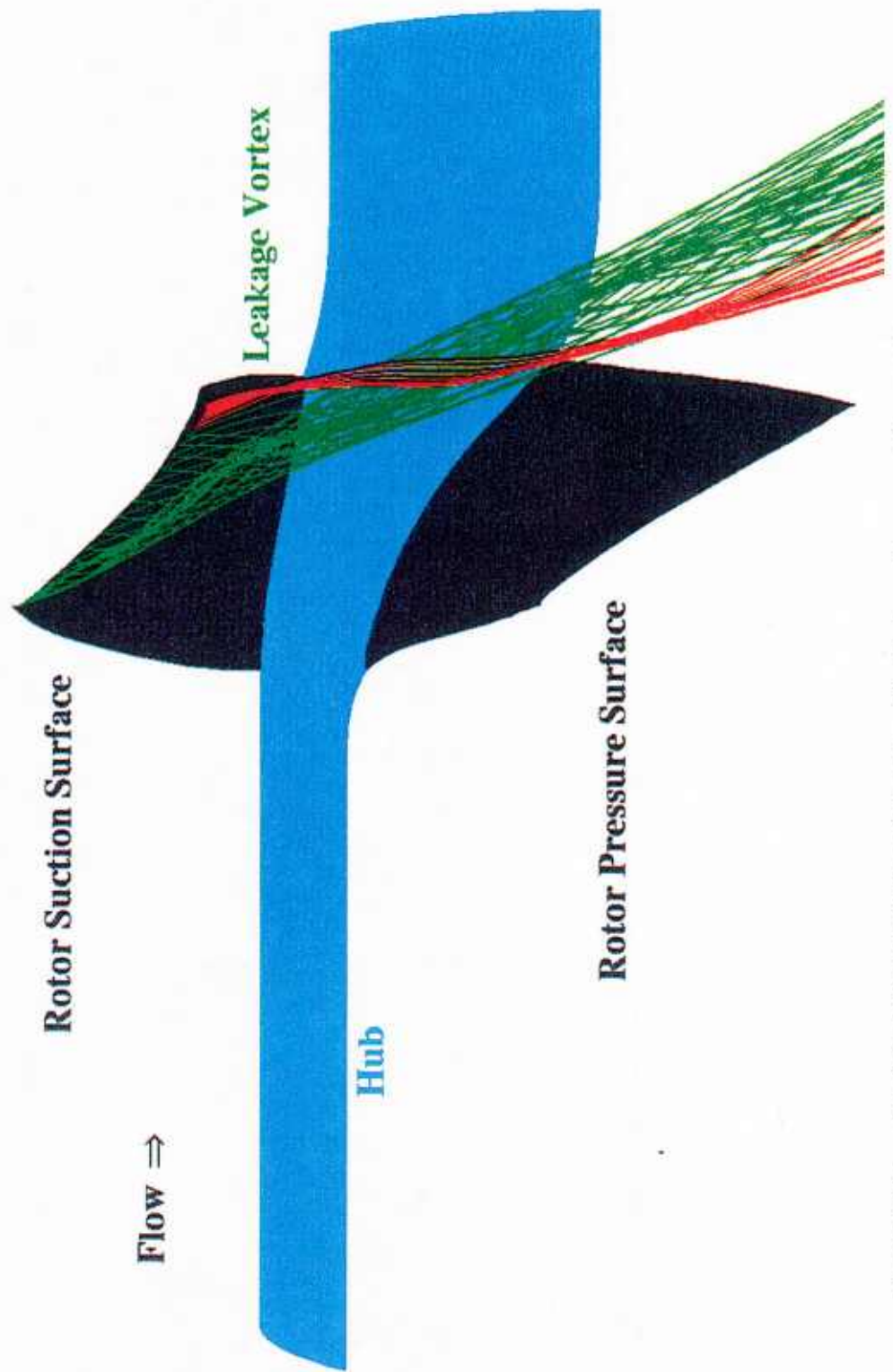


Figure 4.26 Prediction Particle Paths of the Rotor Tip Leakage Vortex and the Trailing Edge Separation Vortex

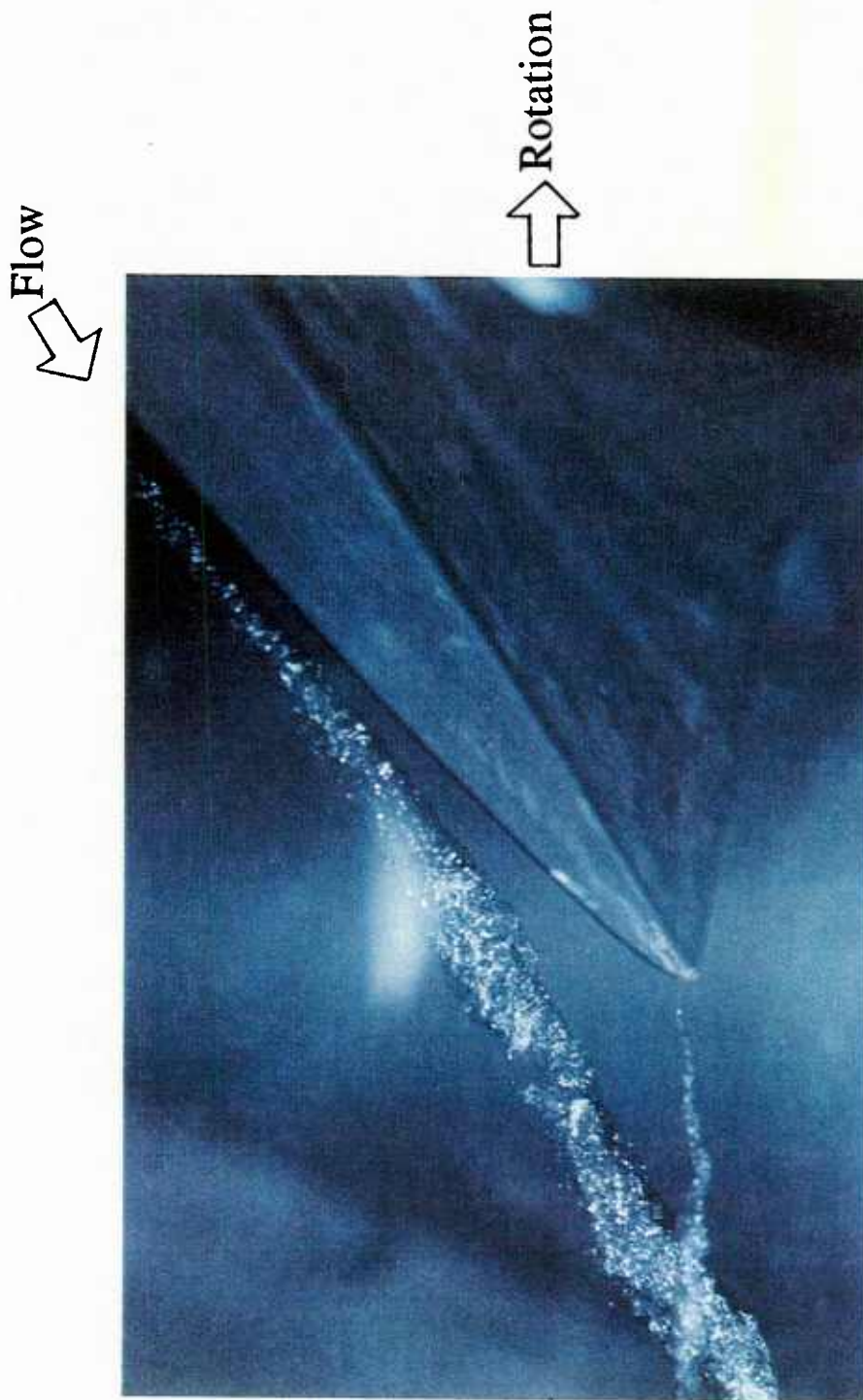


Figure 4.27 Photograph of a Cavitating Rotor Tip Leakage Vortex and a Cavitating Trailing Edge Separation Vortex (Farrell [1989])

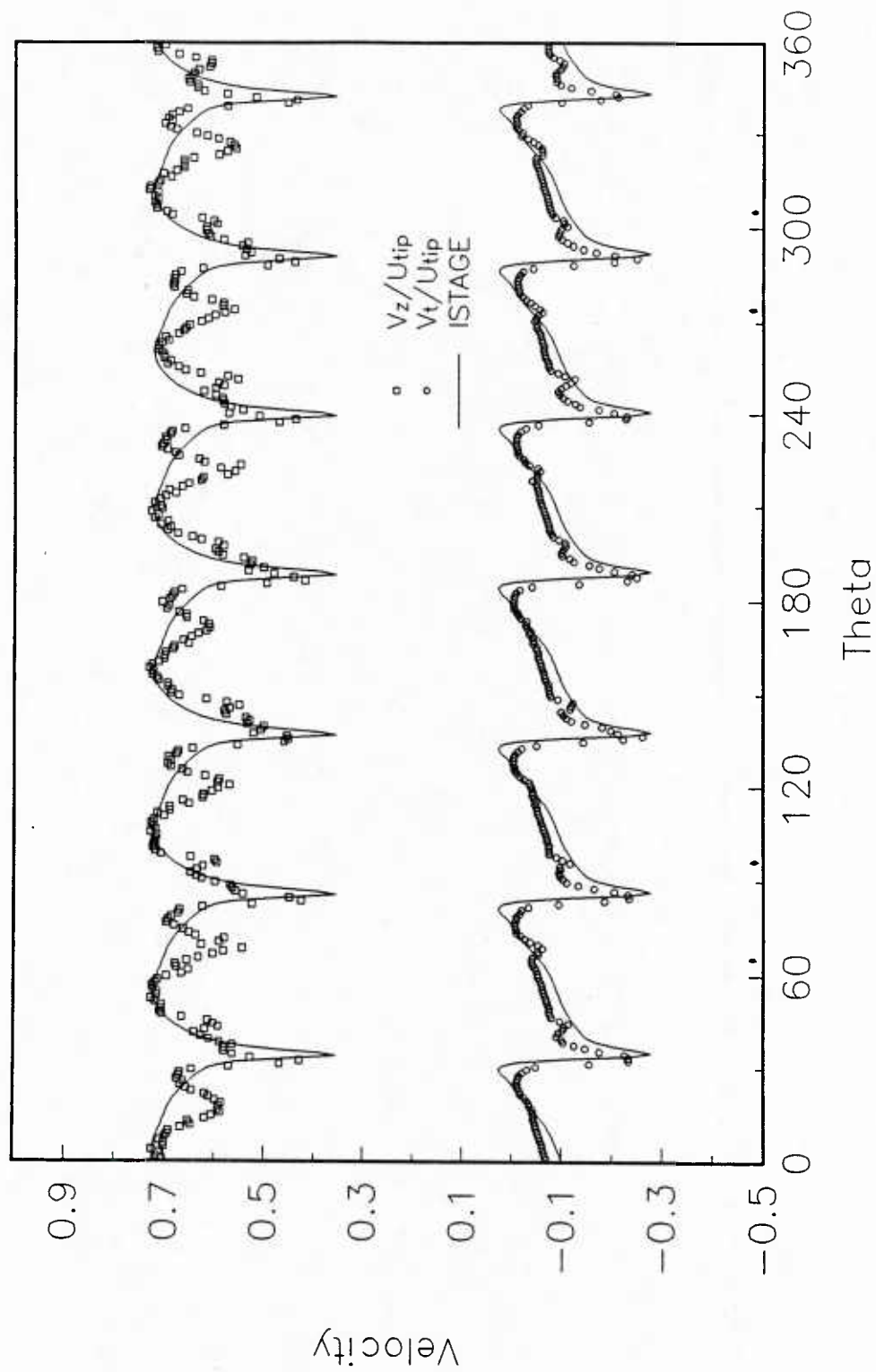


Figure 4.28 Circumferential Variation of Velocity Components 32.2% Chord Axially Downstream of the Rotor Tip Trailing Edge--LDV Measurements and ISTAGE Predictions: (a) 2.9% Span

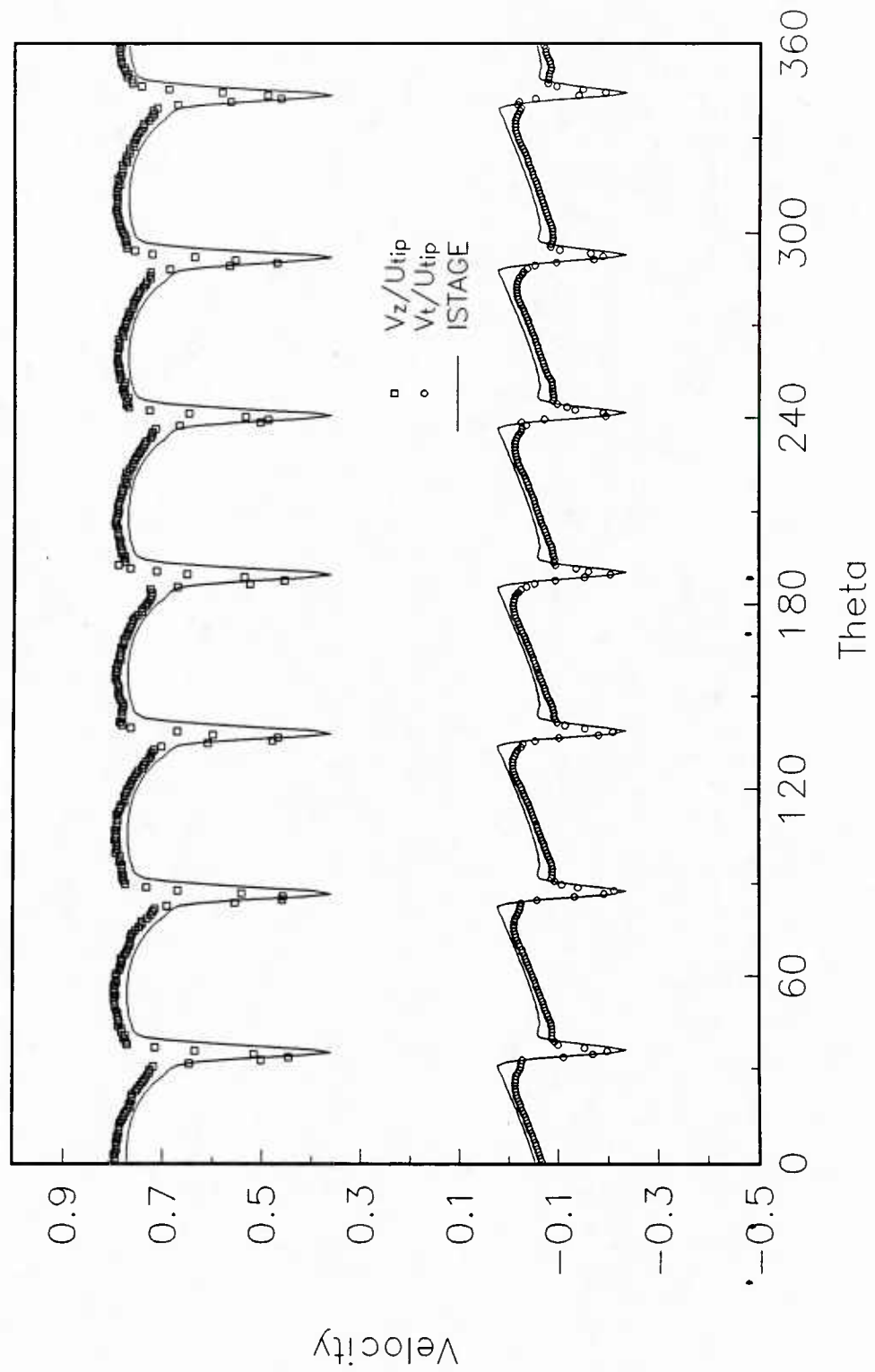


Figure 4.28 Circumferential Variation of Velocity Components 32.2% Chord Axially Downstream of the Rotor Tip Trailing Edge--LDV Measurements and ISTAGE Predictions: (b) 8.6% Span

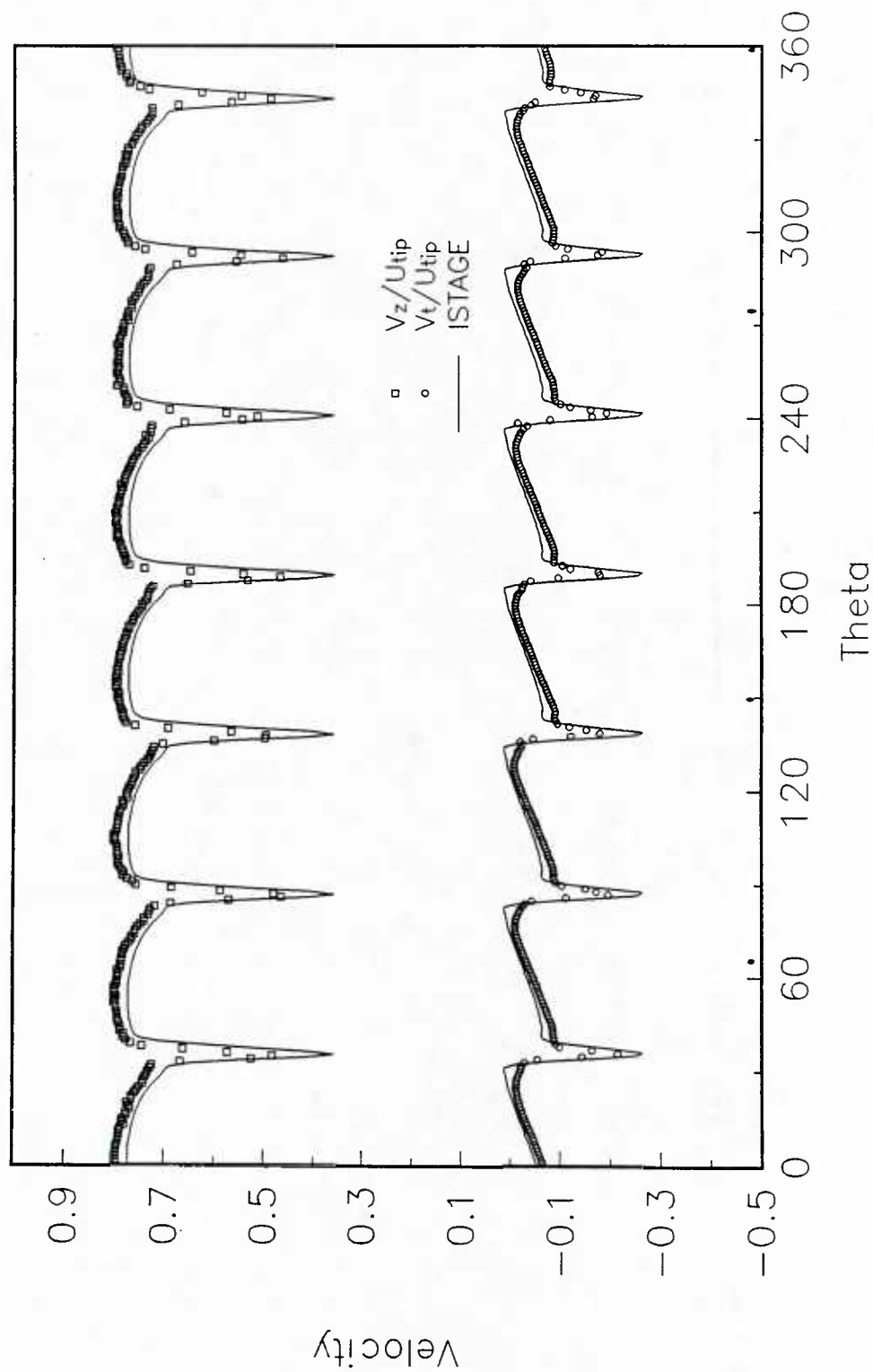


Figure 4.28 Circumferential Variation of Velocity Components 32.2% Chord Axially Downstream of the Rotor Tip Trailing Edge--LDV Measurements and ISTAGE Predictions: (c) 10.5% Span

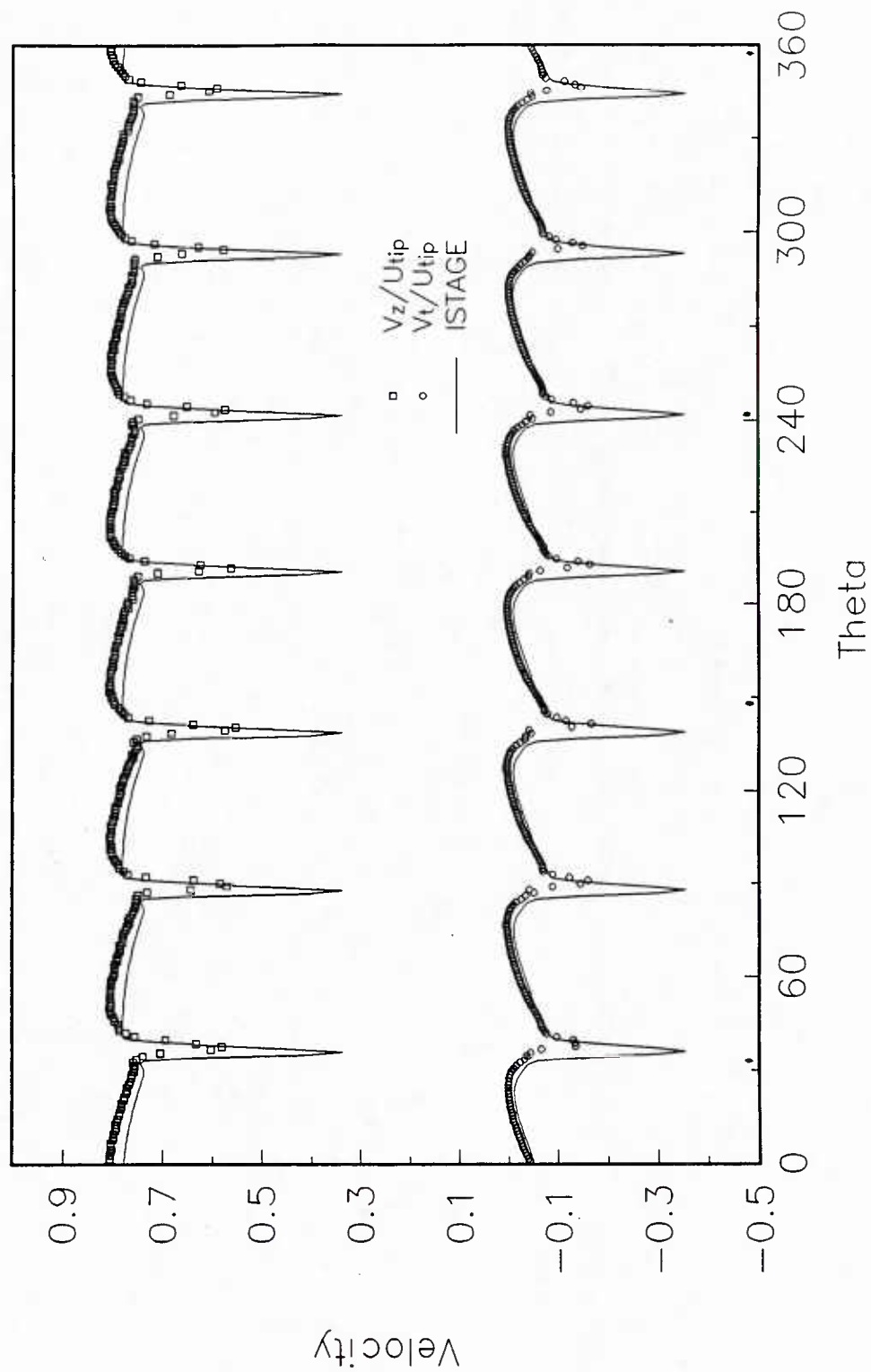


Figure 4.28 Circumferential Variation of Velocity Components 32.2% Chord Axially Downstream of the Rotor Tip Trailing Edge--LDV Measurements and ISTAGE Predictions: (d) 19.9% Span

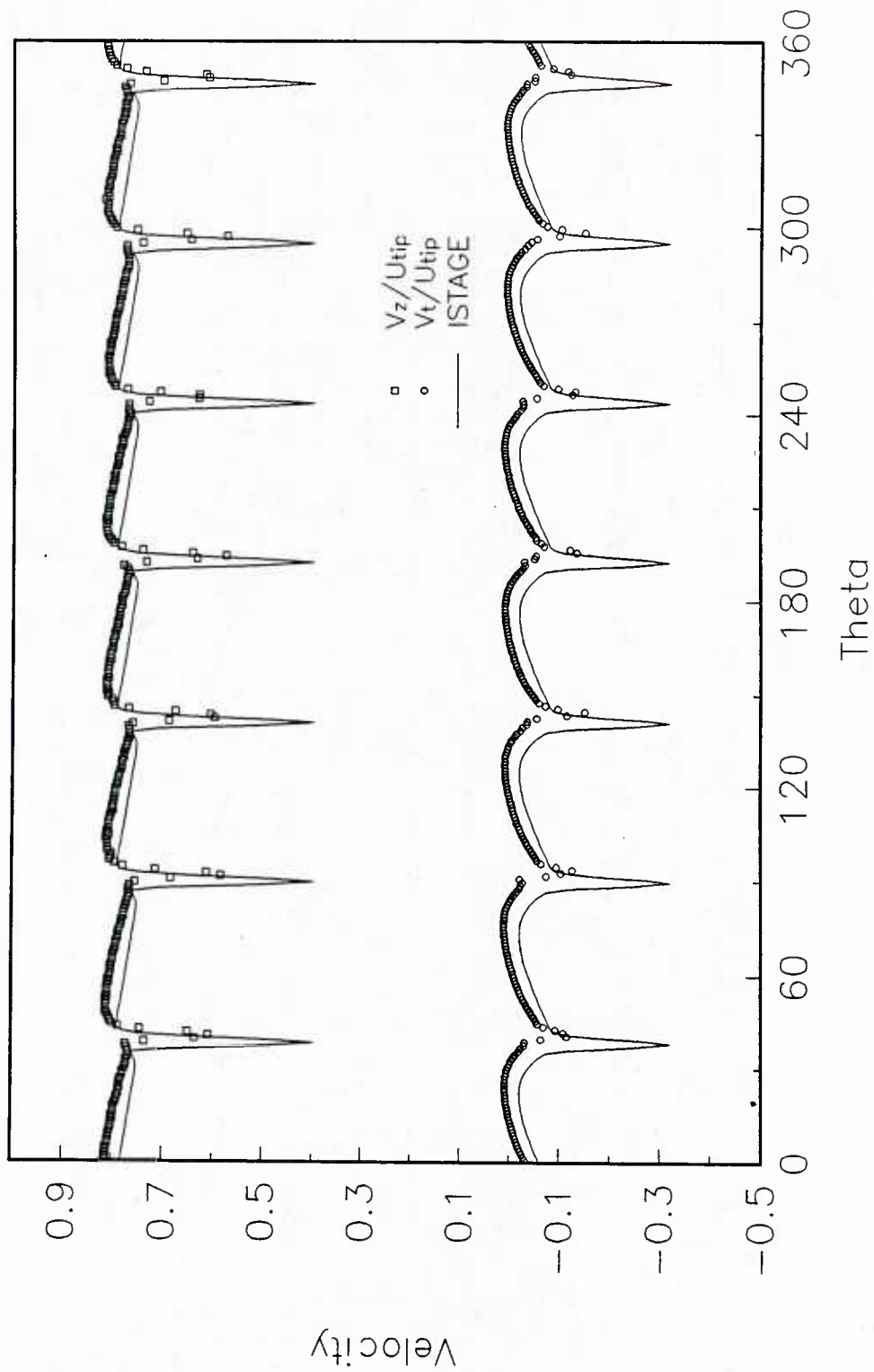


Figure 4.28 Circumferential Variation of Velocity Components 32.2% Chord Axially Downstream of the Rotor Tip Trailing Edge--LDV Measurements and ISTAGE Predictions: (e) 29.4% Span

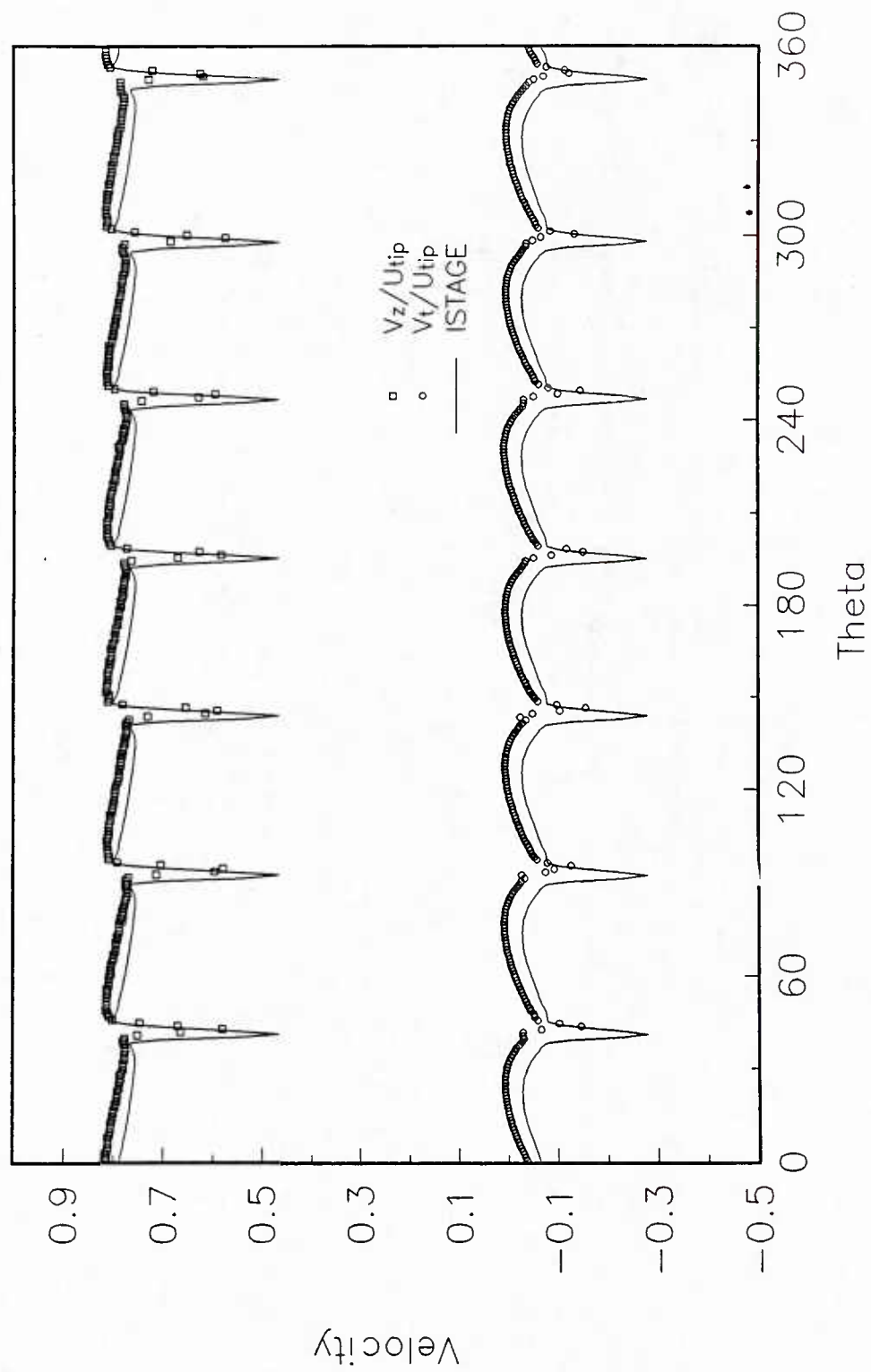


Figure 4.28 Circumferential Variation of Velocity Components 32.2% Chord Axially Downstream of the Rotor Tip Trailing Edge--LDV Measurements and ISTAGE Predictions: (f) 38.8% Span

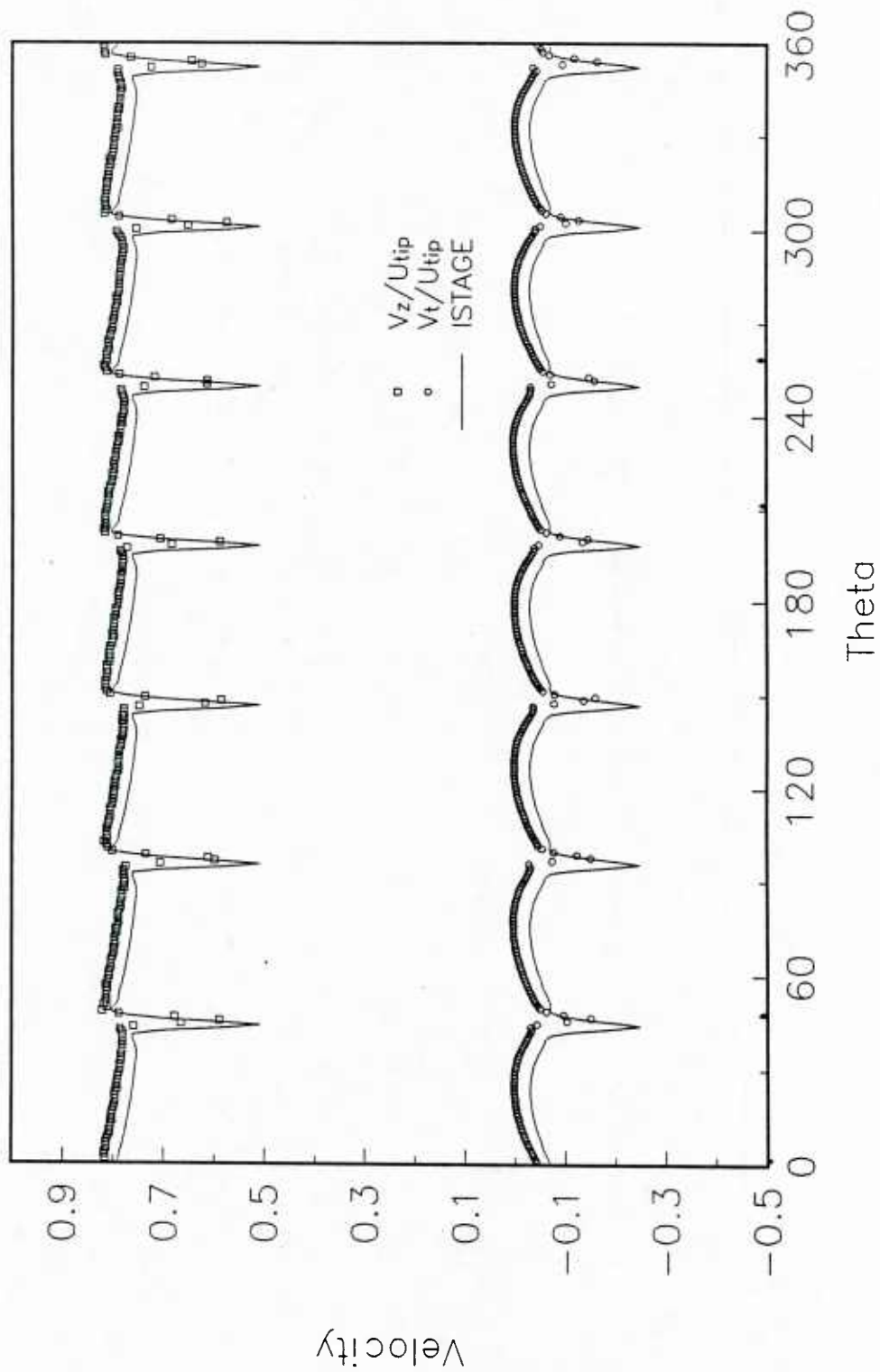


Figure 4.28 Circumferential Variation of Velocity Components 32.2% Chord Axially Downstream of the Rotor Tip Trailing Edge--LDV Measurements and ISTAGE Predictions: (g) 48.2% Span

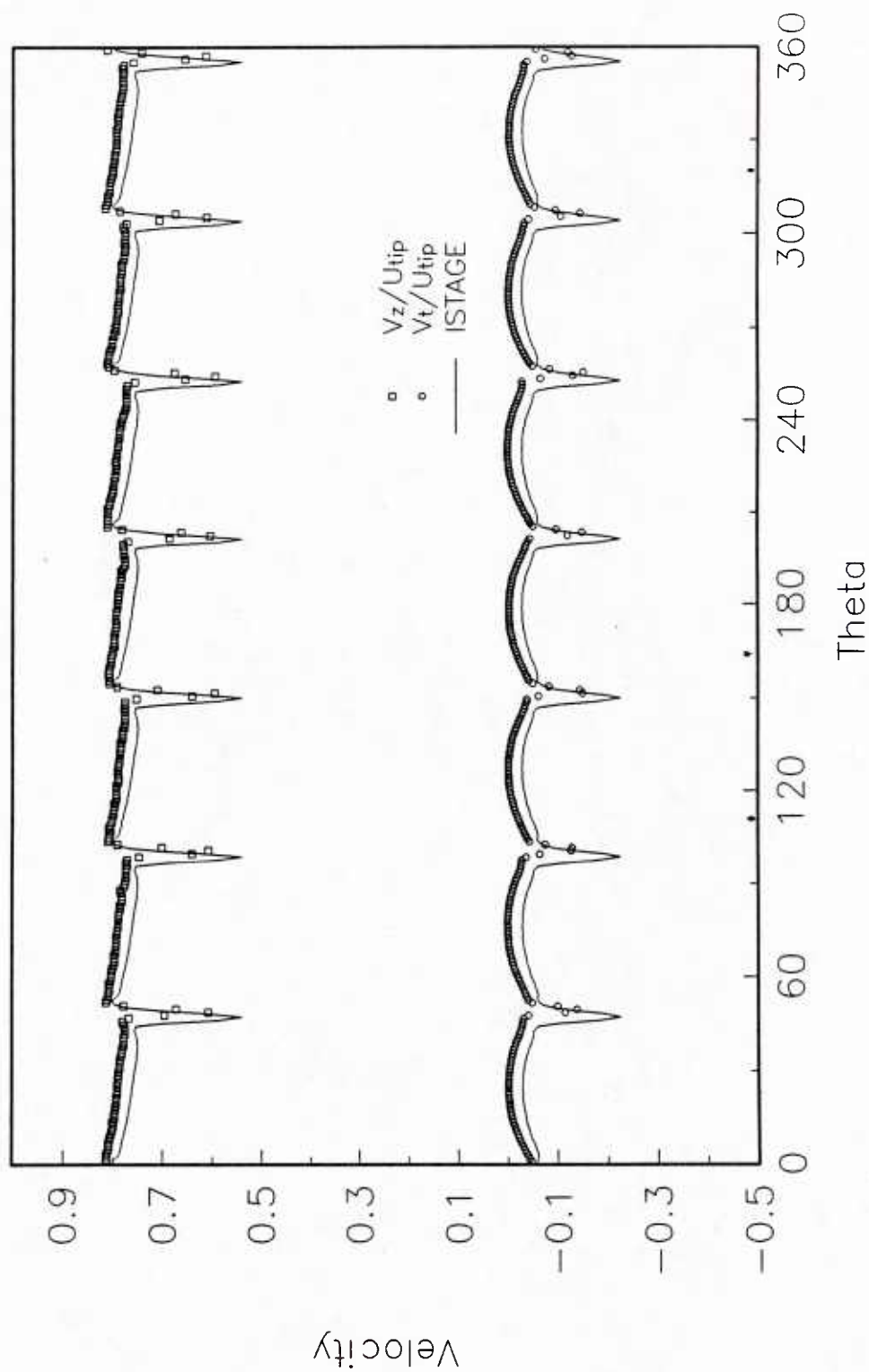


Figure 4.28 Circumferential Variation of Velocity Components 32.2% Chord Axially Downstream of the Rotor Tip Trailing Edge--LDV Measurements and ISTAGE Predictions: (h) 57.7% Span

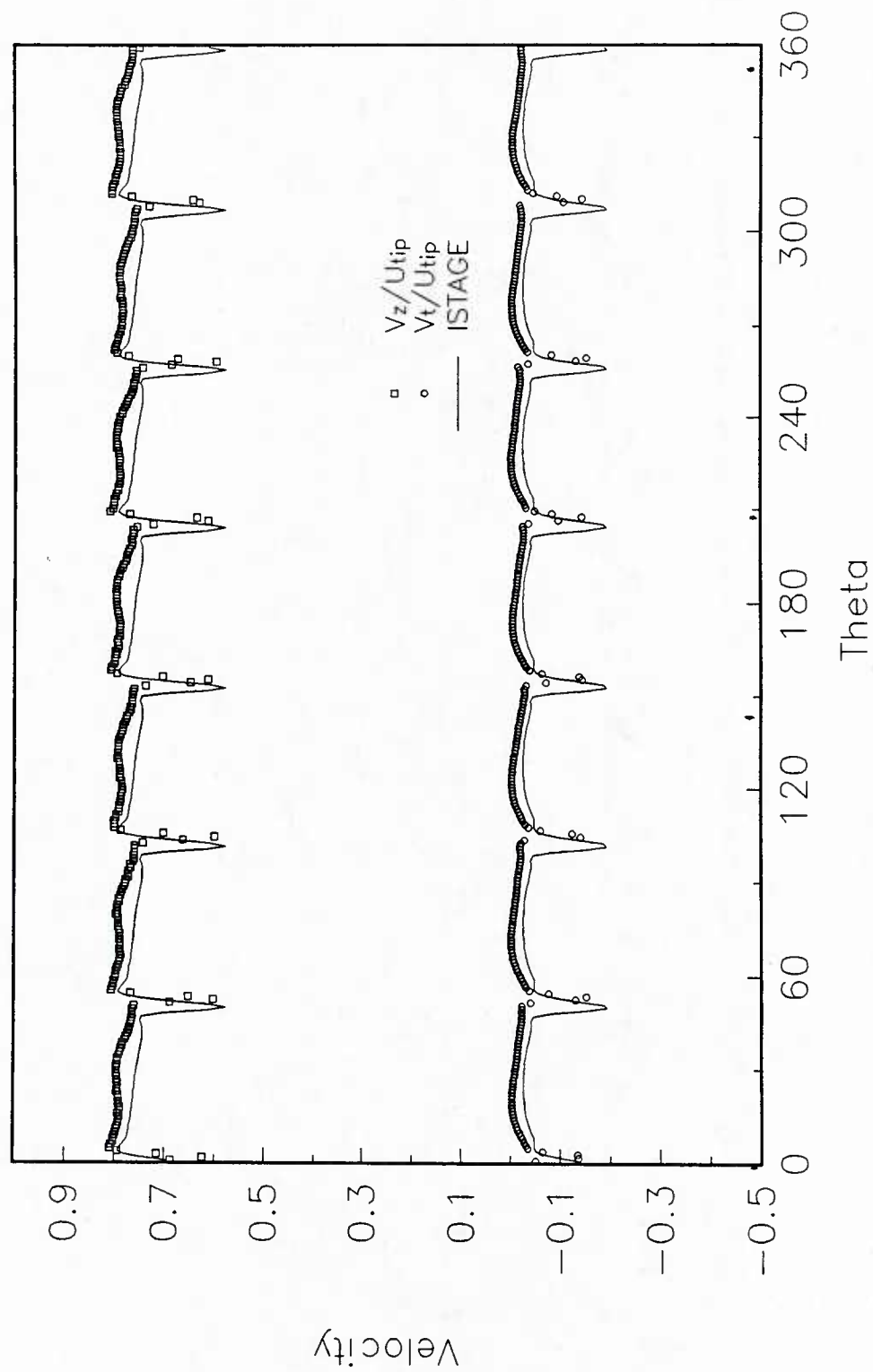


Figure 4.28 Circumferential Variation of Velocity Components 32.2% Chord Axially Downstream of the Rotor Tip Trailing Edge--LDV Measurements and ISTAGE Predictions: (i) 67.1% Span

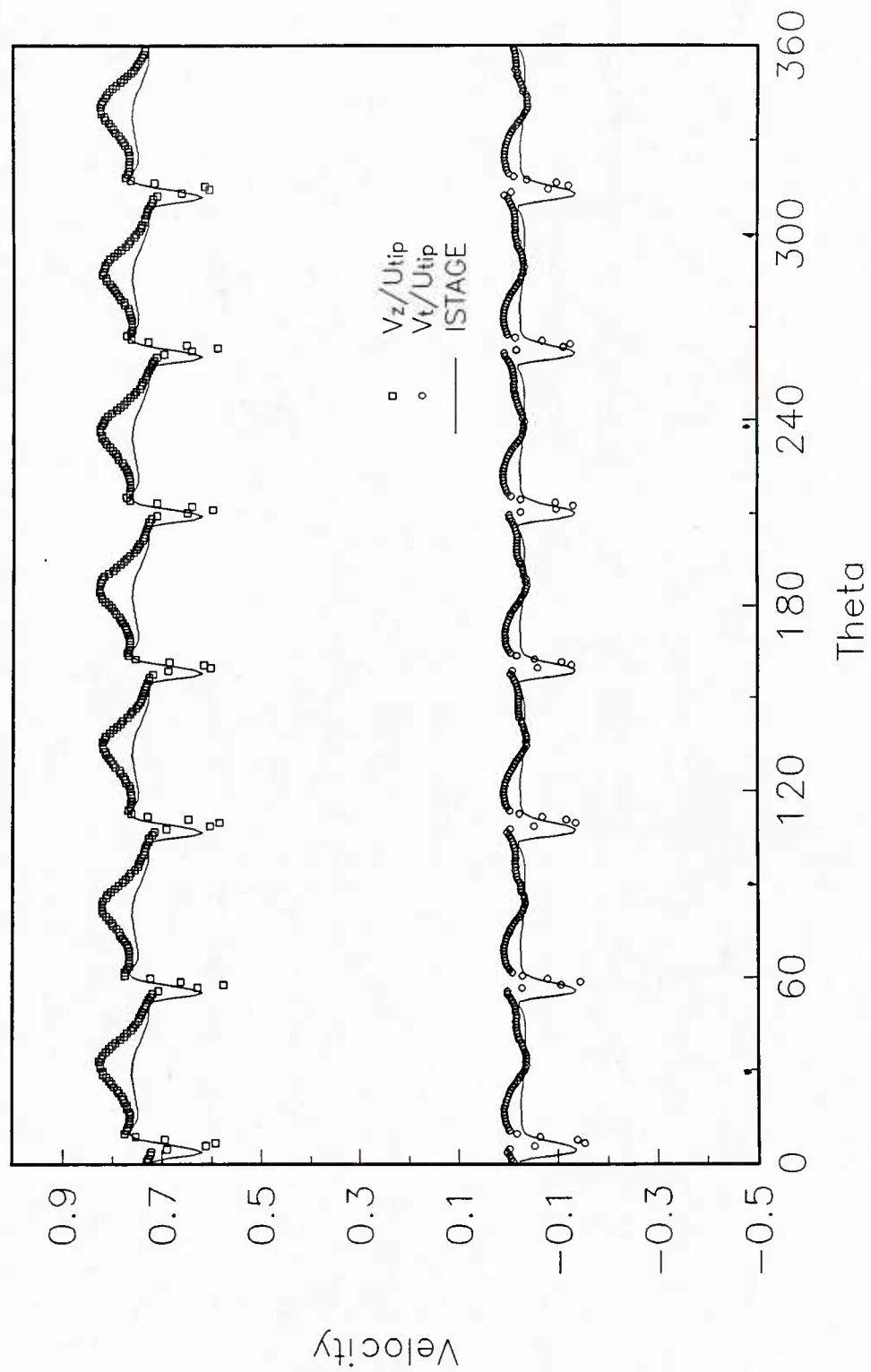


Figure 4.28 Circumferential Variation of Velocity Components 32.2% Chord Axially Downstream of the Rotor Tip Trailing Edge--LDV Measurements and ISTAGE Predictions: (j) 81.3% Span

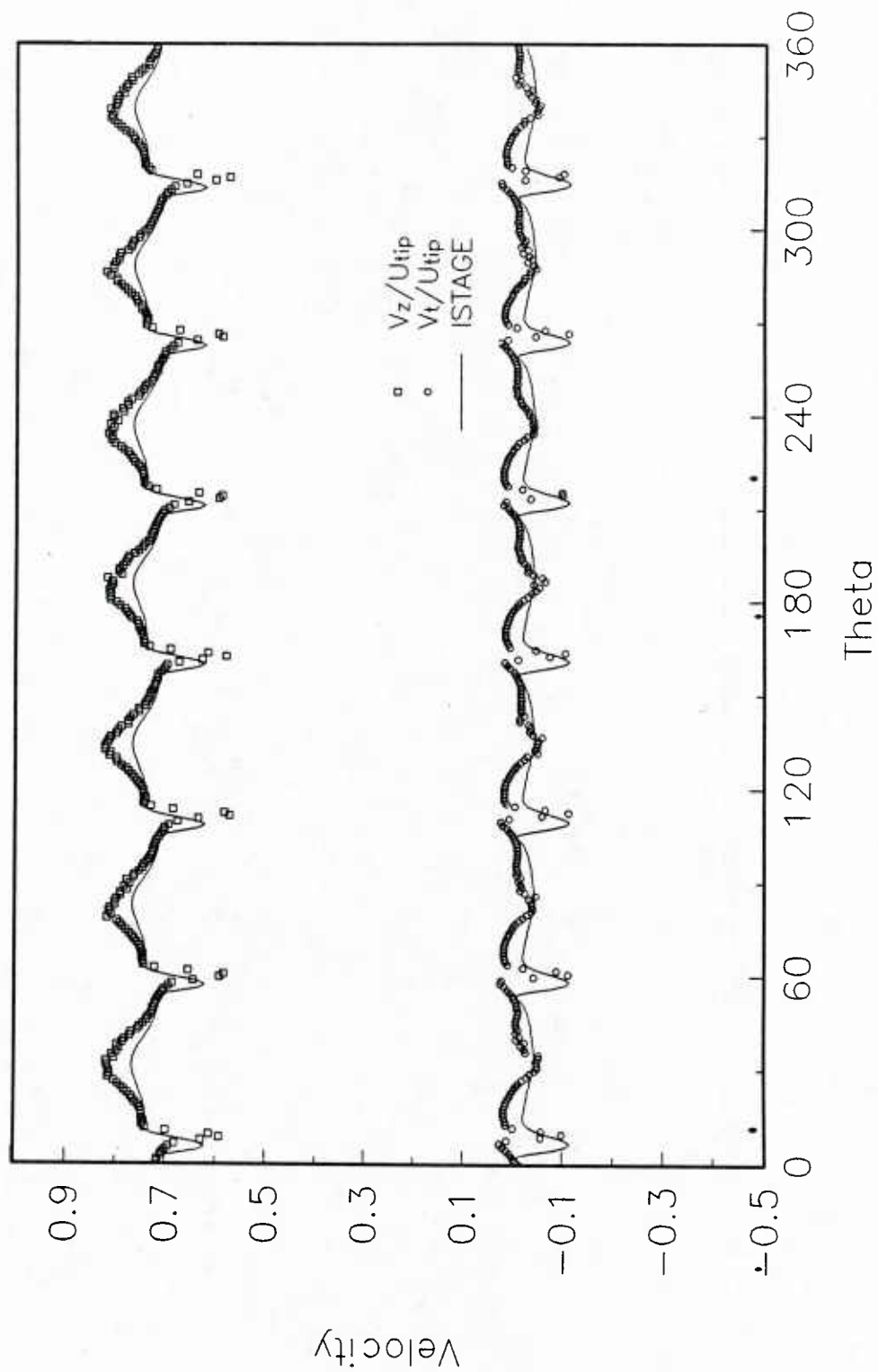


Figure 4.28 Circumferential Variation of Velocity Components 32.2% Chord Axially Downstream of the Rotor Tip Trailing Edge--LDV Measurements and ISTAGE Predictions: (k) 86.0% Span

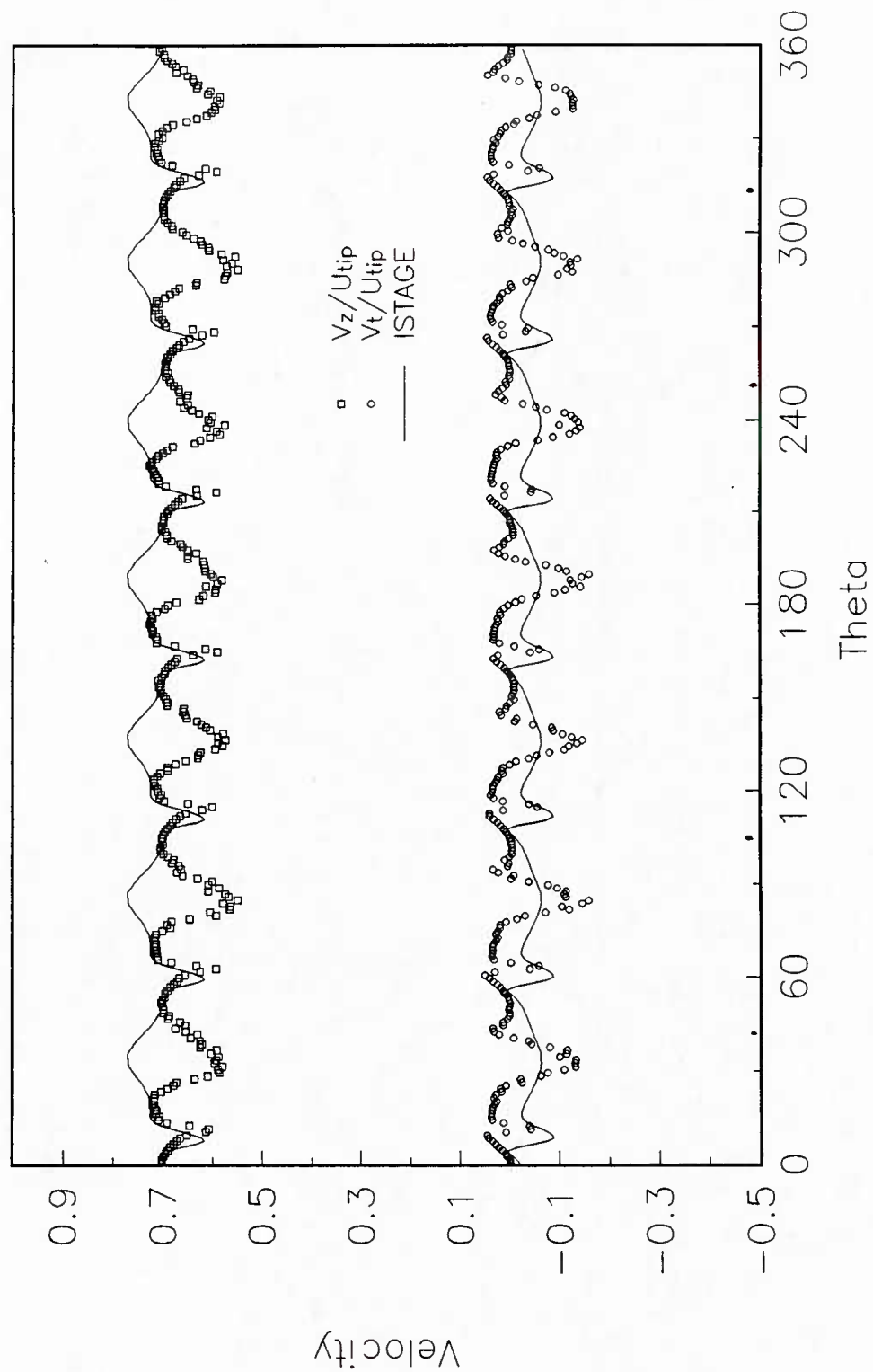


Figure 4.28 Circumferential Variation of Velocity Components 32.2% Chord Axially Downstream of the Rotor Tip Trailing Edge--LDV Measurements and ISTAGE Predictions: (1) 90.7% Span

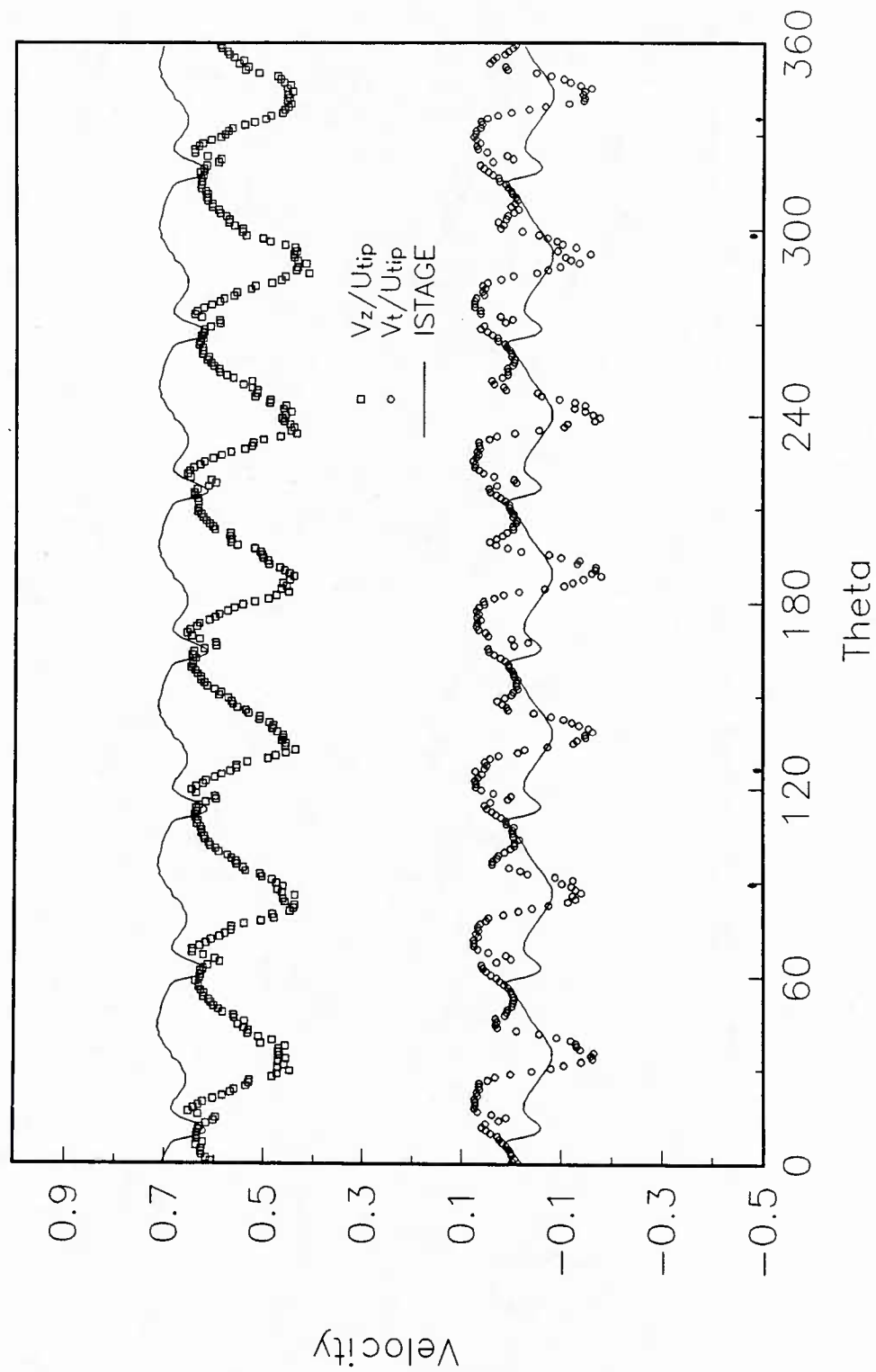


Figure 4.28 Circumferential Variation of Velocity Components 32.2% Chord Axially Downstream of the Rotor Tip Trailing Edge--LDV Measurements and ISTAGE Predictions: (m) 94.5% Span

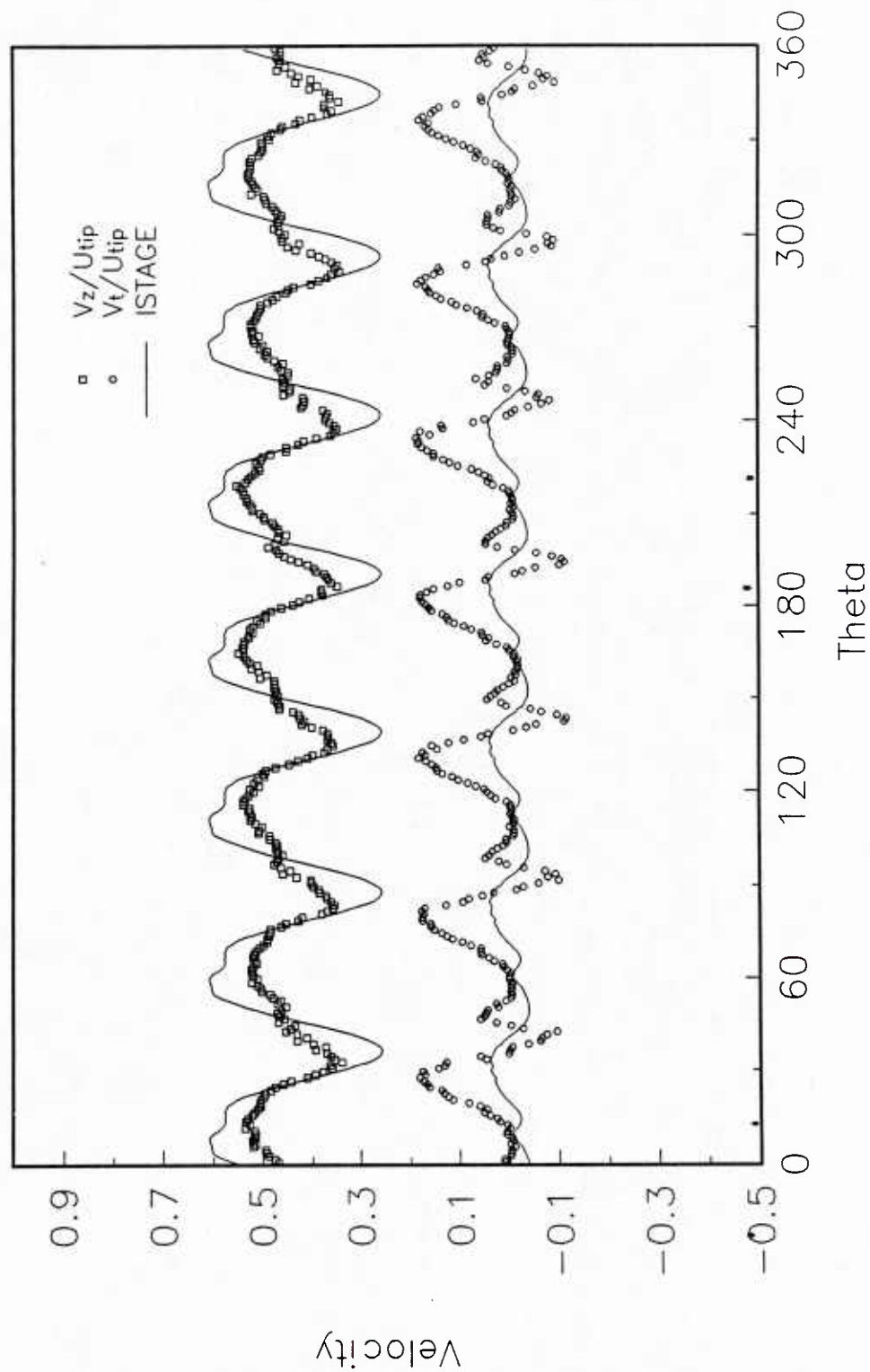


Figure 4.28 Circumferential Variation of Velocity Components 32.2% Chord Axially Downstream of the Rotor Tip Trailing Edge--LDV Measurements and ISTAGE Predictions: (n) 98.3% Span

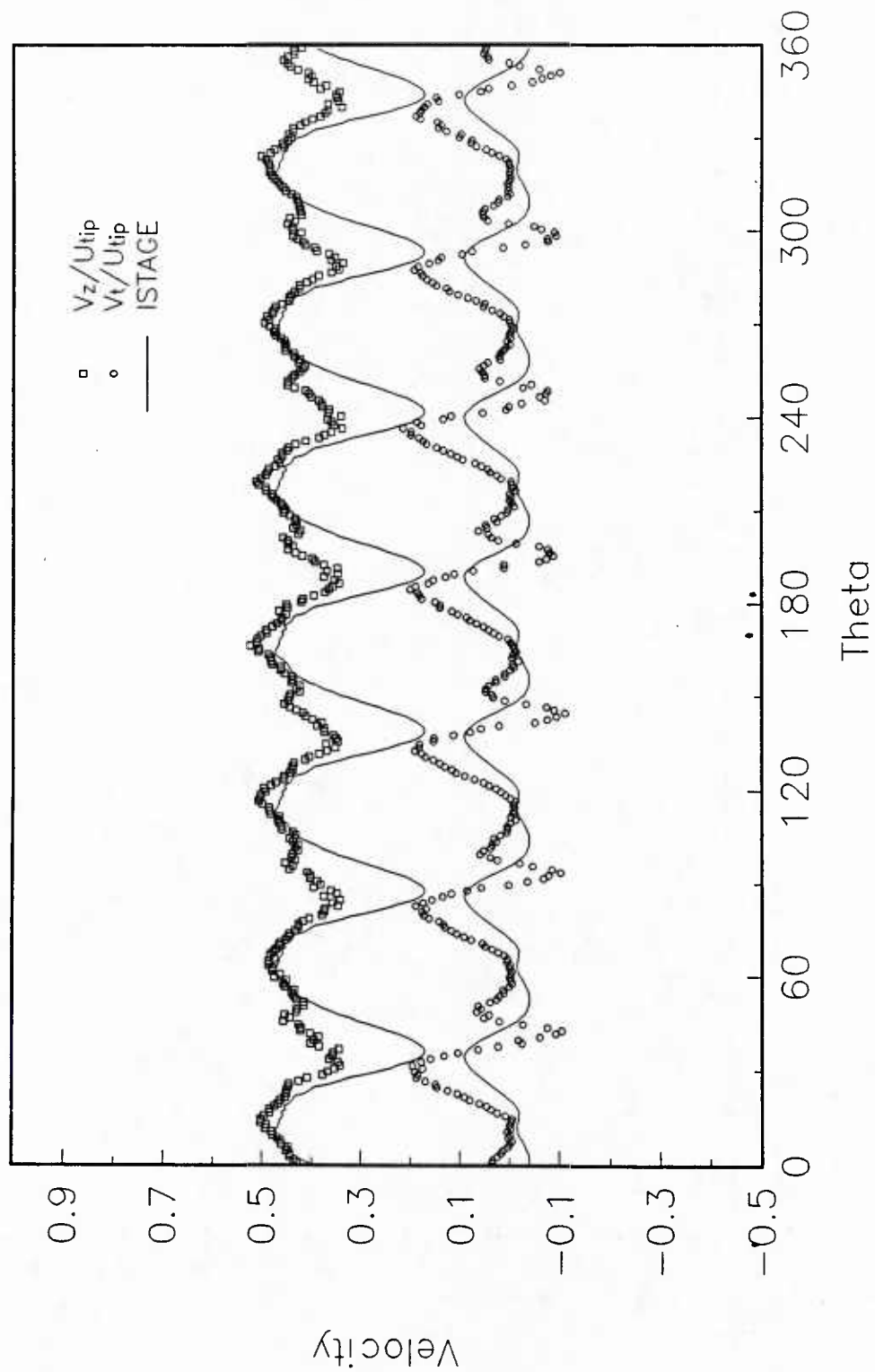


Figure 4.28 Circumferential Variation of Velocity Components 32.2% Chord Axially Downstream of the Rotor Tip Trailing Edge--LDV Measurements and ISTAGE Predictions: (o) 99.2% Span

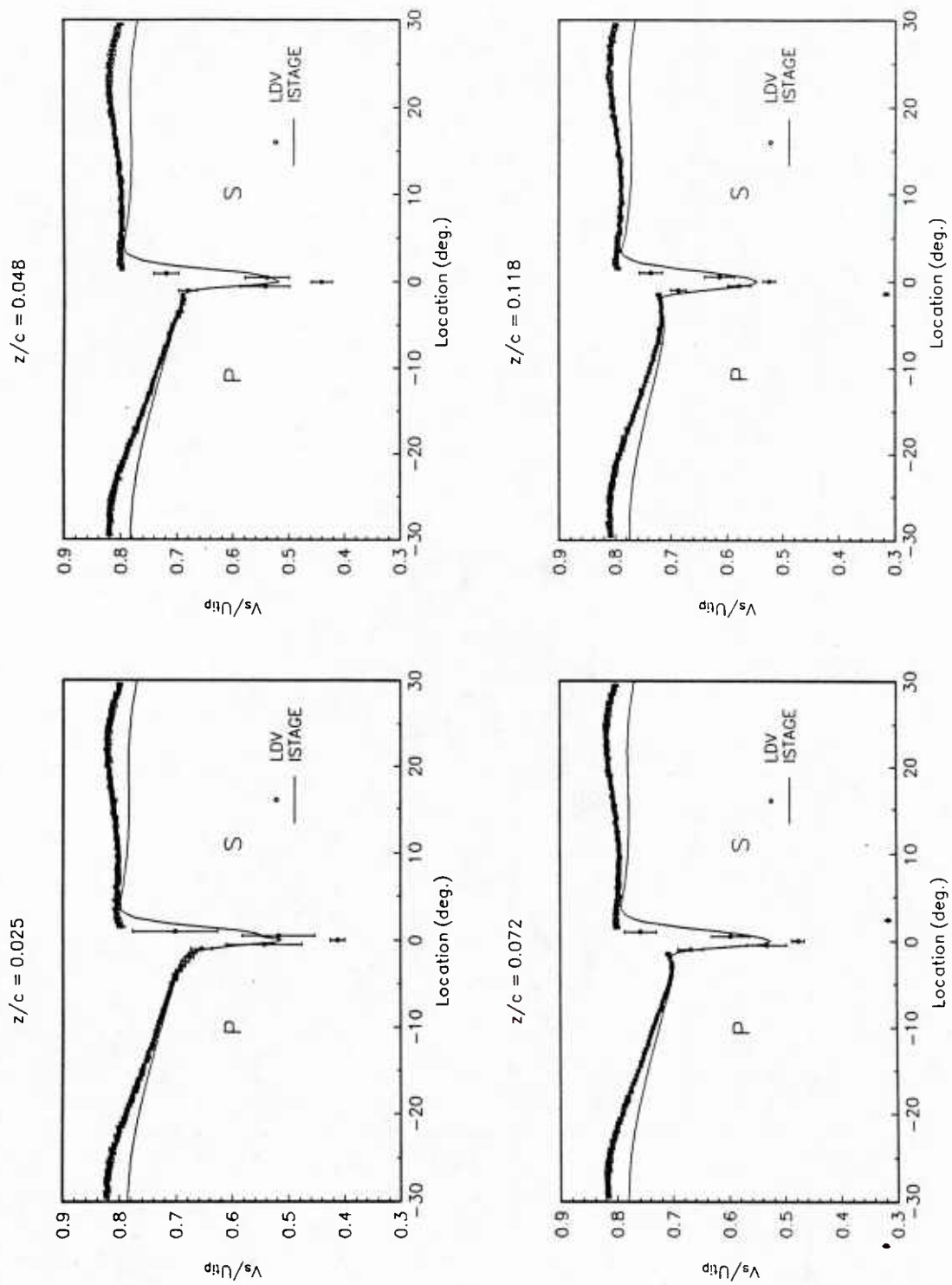


Figure 4.29 Passage-Averaged Rotor Blade Wakes at 76.2% Span: (a) 2.5%, 4.8%, 7.2%, and 11.8% Chord Axially Downstream of the Rotor Blade Trailing Edge

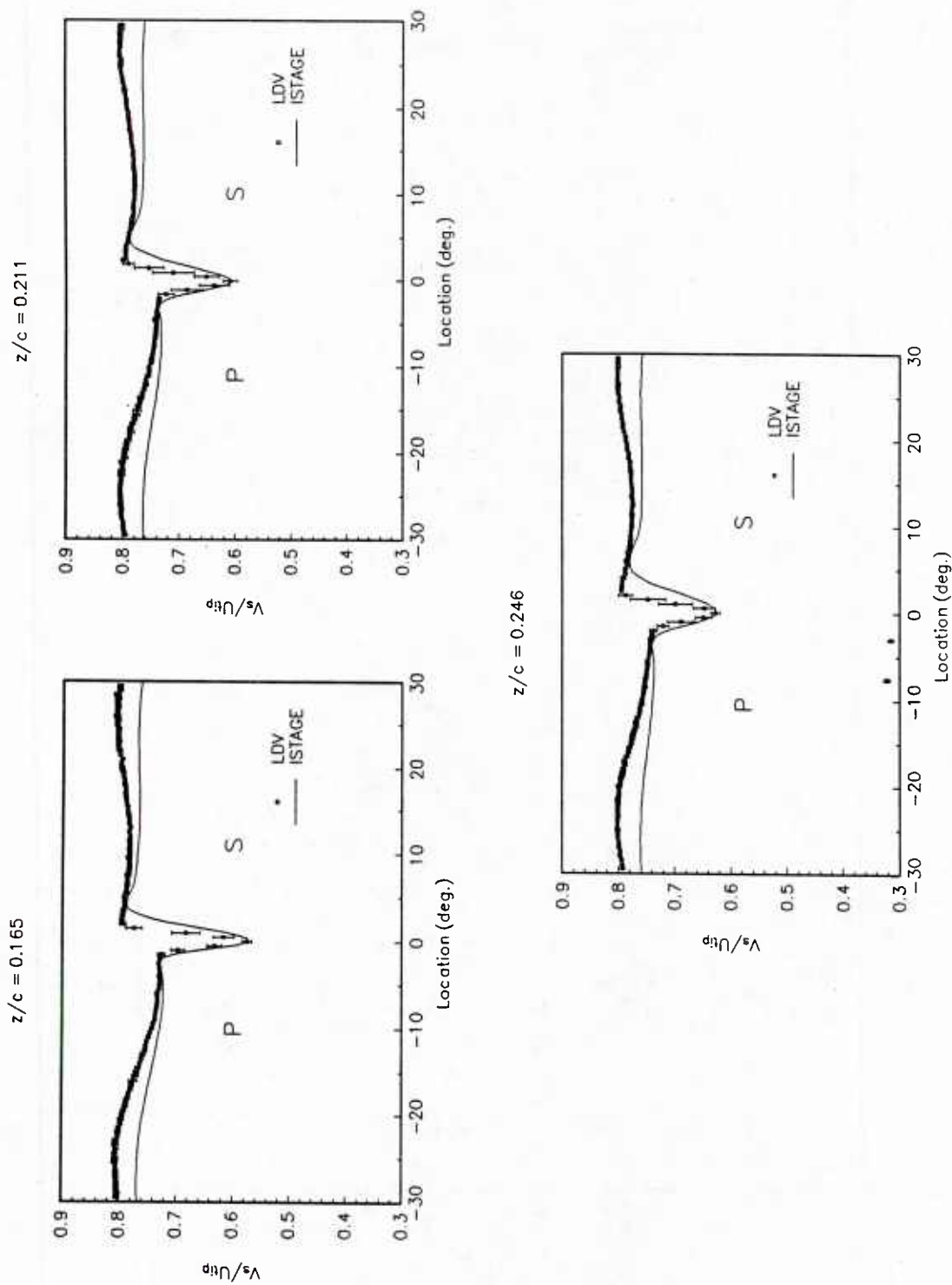


Figure 4.29 Passage-Averaged Rotor Blade Wakes at 76.2% Span: (b) 16.5%, 21.1%, and 24.6% Chord Axially Downstream of the Rotor Blade Trailing Edge

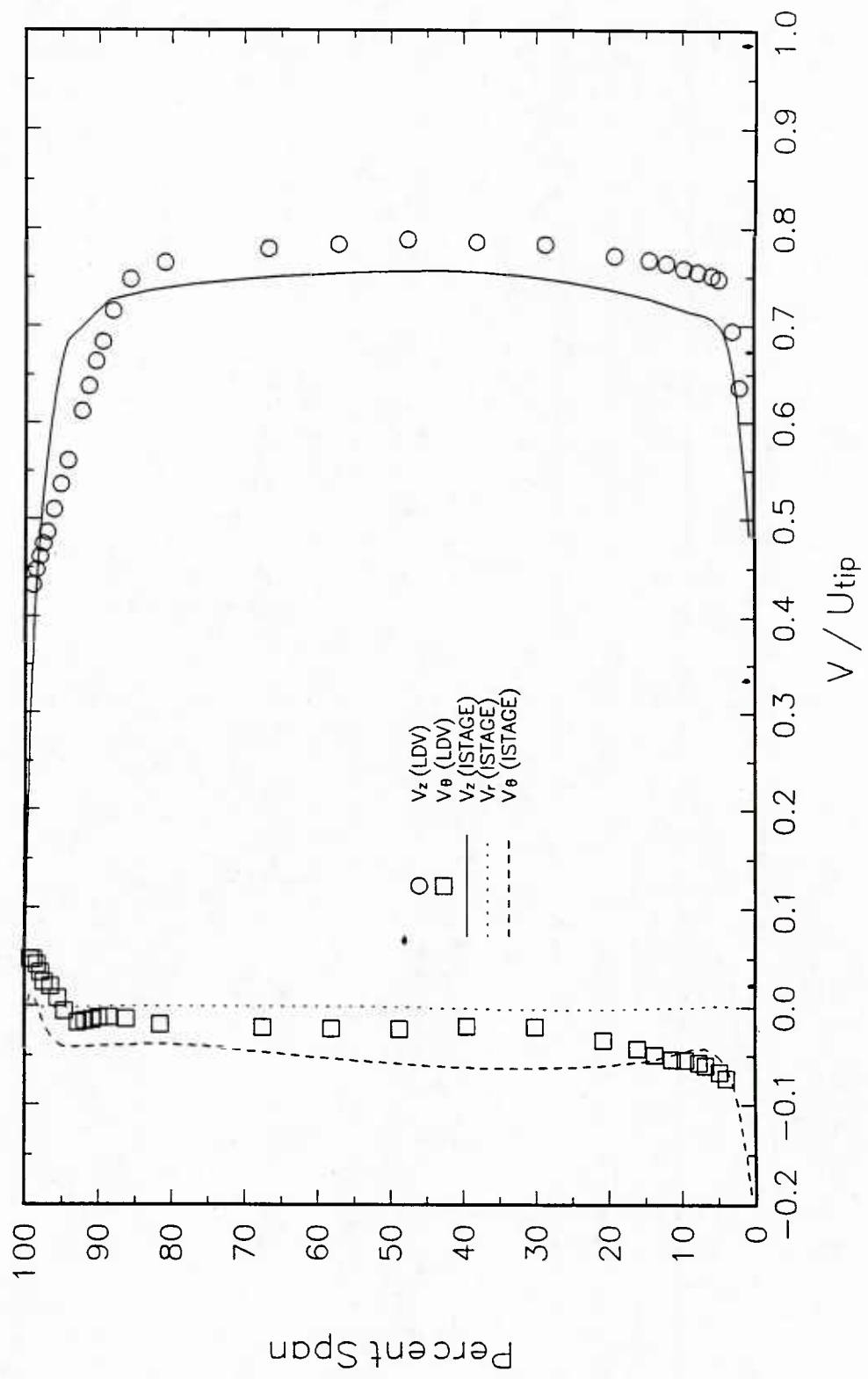


Figure 4.30 Circumferentially-Averaged Velocities 32.2% Chord Axially Downstream of the Rotor Tip Trailing Edge

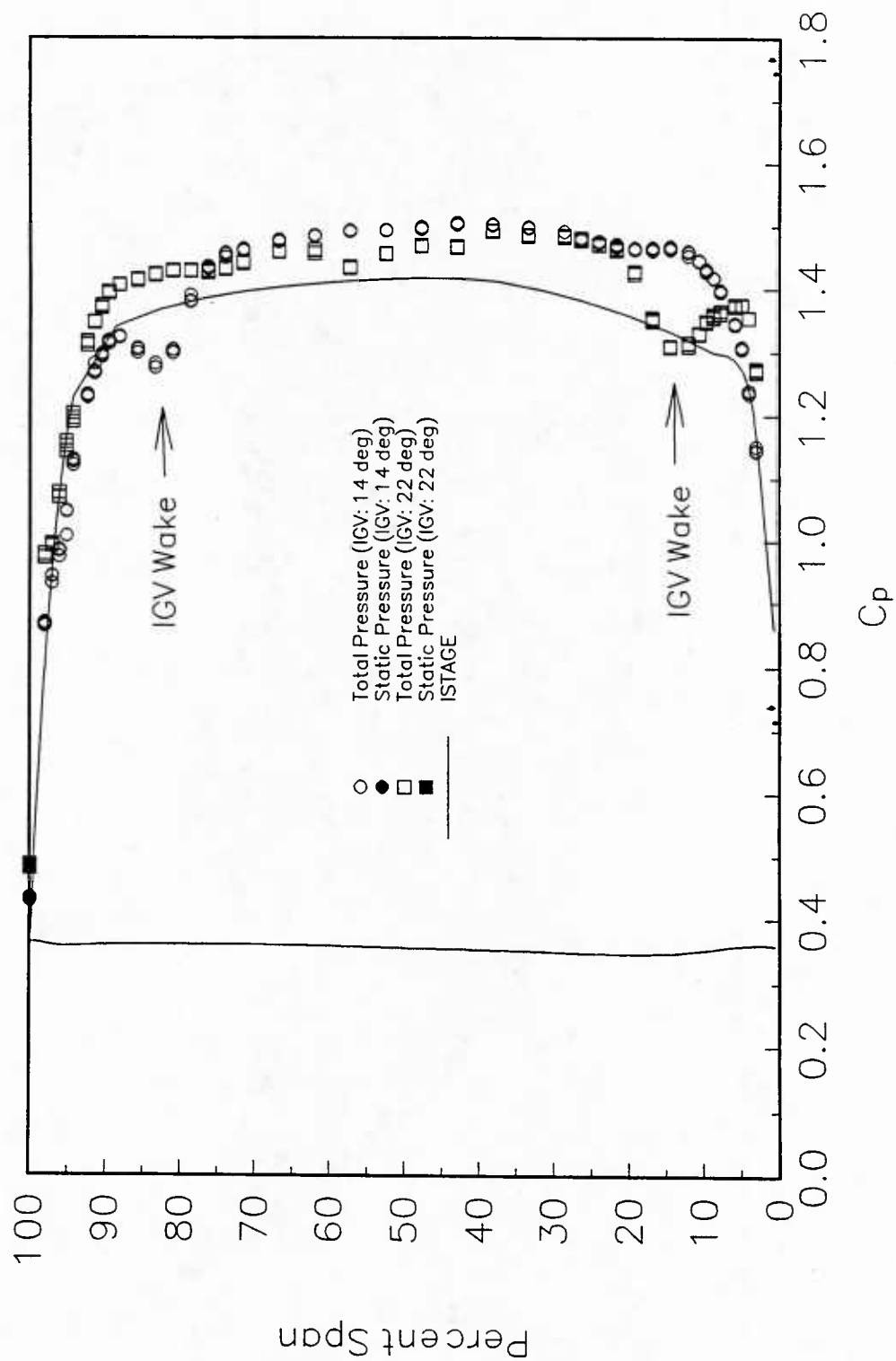


Figure 4.31 Circumferentially-Averaged Pressure Coefficients 32.2% Chord Axially Downstream of the Rotor Tip Trailing Edge

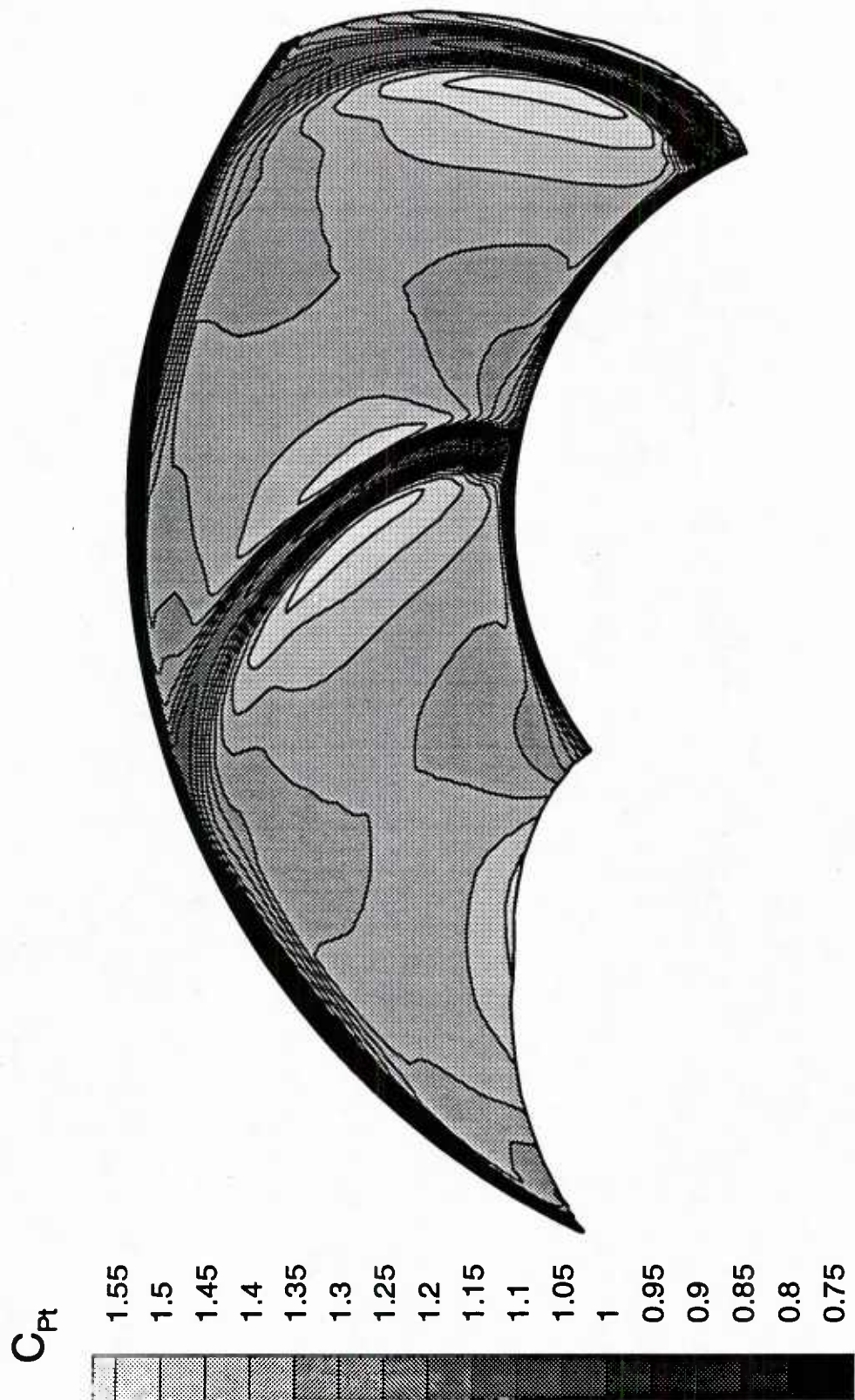


Figure 4.32 Predicted Contours of Total-Pressure Coefficient 32.2% Chord Axially Downstream of the Rotor Tip Trailing Edge

DUDLEY KNOX LIBRARY - RESEARCH REPORTS



5 6853 01056743 1

U270181

The Pennsylvania State University
Applied Research Laboratory
P.O. Box 30
State College, PA 16804